UNIVERSITÉ DU
LUXEMBOURG

DISSERTATION

Defense held on 11/09/2023 in Luxembourg

to obtain the degree of

DOCTEUR DE L'UNIVERSITÉ DU LUXEMBOURG EN SCIENCES DE L'INGÉNIEUR

by

Lionel CLASING

Born on January 22, 1988 in Lippstadt (Germany)

OPTICAL AND THERMAL ANALYSIS AND OPTIMIZATION OF HYBRID SOLAR ROOF TILES

Dissertation defense committee

Prof. Dr.-Ing. Jean-Régis Hadji-Minaglou, Dissertation Supervisor
Professor, Université du Luxembourg

Prof. Dr. rer. nat. Ulf Blieske, Reviewer
Professor, Cologne University of Applied Sciences

Prof. Dr.-Ing. Inès Chihi, Vice Chairman
Professor, Université du Luxembourg

Prof. Dr. rer. nat. Stephan Leyer, Chairman
Professor, Université du Luxembourg

Dr. Nils Reiners, Reviewer
Fraunhofer Institute for Solar Energy Systems

Declaration of Authorship

I, Lionel CLASING, declare that this thesis titled, 'OPTICAL AND THERMAL ANALYSIS AND OPTIMIZATION OF HYBRID SOLAR ROOF TILES' and the work presented in it are my own. I confirm that:

- This work was done wholly or mainly while in candidature for a research degree at this University.

- Where any part of this thesis has previously been submitted for a degree or any other qualification at this University or any other institution, this has been clearly stated.

- Where I have consulted the published work of others, this is always clearly attributed.

- Where I have quoted from the work of others, the source is always given. With the exception of such quotations, this thesis is entirely my own work.

- I have acknowledged all main sources of help.

- Where the thesis is based on work done by myself jointly with others, I have made clear exactly what was done by others and what I have contributed myself.

Signed:

L. Clasing

Date:
July 14, 2023, Cologne

Abstract

Building-integrated photovoltaic and solar thermal systems have great potential to save greenhouse gas emissions through improved area utilization of building envelopes while replacing building components and energy transfer losses. In addition, the application of hybrid technology to these modules enhances their overall performance. Despite these advantages, the investment costs are higher, there are no suitable building codes, and there is a lack of solutions to application-specific problems. In order to address these issues, an improved module design is presented. The design has the characteristics of a roof tile and meets application-specific requirements such as durability, accessibility, easy installation, replacement and maintenance, as well as high efficiency & aesthetics. Nevertheless, predictability of the energy yields, operation performance and effective heat utilization are also decisive factors for the commercialization of these systems. Another point to consider is the application of colored glasses, which can improve the aesthetic appearance and thus the acceptance of building-integrated solar systems. In order to contribute to these factors with regard to the improved module design presented, research gaps on three topics were identified through an analysis of the current state of this technology. These topics are: i) modeling and analysis of custom module designs; ii) identification and quantification of the optimization potential to maximize operational performance; and iii) experimental and numerical performance assessment of improved module designs.

This thesis focuses on optical and thermal analysis as well as optimization of an improved building-integrated photovoltaic and solar thermal module design with active rear ventilation. A simulation framework with suitable models to analyze optimization potential and predict the overall performance under real operating conditions is developed and validated by experimental field measurements. Therefore, optical, electrical and thermal models are set up and parameterized by small-scale laboratory measurements and simulations. In addition, a modeling approach using angular-dependent spectral responsivity to simulate the performance of colored glasses is developed and validated. Another focus of the work is to identify and quantify the optical and thermal optimization potential. Hence, angular-dependent optical parameters of nano-imprinted textured front covers are measured and used to quantify the annual increase in optical performance in a simulation study. Likewise, numerical simulations are used to determine the optimal mass flow rate as a function of system leakage using the effective thermal efficiency approach. The performance of a system with the improved module design is assessed by measurements in an experimental field test over a one-year period. In addition, annual performance is evaluated by a simulation case study with different climatic conditions and system configurations using the validated modeling framework. Finally, an air-source heat pump to

utilize the preheated air was used in the field test and modeled in the simulation study.

A summary of the key findings related to the research topics is presented as follows: A time-series based simulation framework for the improved module design with a prediction accuracy of the electrical and thermal energy yield with a mean relative error of less than $\pm 1\%$ is developed. The angular-dependent spectral responsivity performance modeling approach for high-transmissive colored glasses shows a root mean square error between 1.9% and 2.5%. The improvements by optical optimization result in a maximum annual relative increase in optical performance of 2.2% for nano-imprinted textures. In contrast, the thermal optimizations revealed a maximum effective thermal efficiency of 24.3% for a module design with air leakage. Thirdly, the performance assessment of the experimental system shows a maximum thermal efficiency of 12%. In comparison, the simulated annual thermal efficiency for Cologne shows 11%, while the overall efficiency taking into account the energy for the rear ventilation system is 23%. Also, the field test revealed a relative increase in performance ratio of up to 16% in comparison to systems without active rear ventilation. The experimental measurement series showed a relative increase in the coefficient of performance of 20% on average, while the simulated maximum seasonal performance factor increased by 21%. Finally, the maximum module temperature was observed at 74°C. The maximum air outlet temperature in the rear ventilation system is 52°C in summer and 33°C in winter.

In conclusion, the accuracy of the developed simulation framework is acceptable for assessing the performance of the improved module design. The presented modeling approach is highly flexible and can therefore be adapted to custom module and system designs. The angle-dependent spectral responsivity simulation model has the greatest value for predicting the outdoor performance of colored glass fronts. Furthermore, it can be stated that the angular-dependent optical performance optimization potential is comparatively low, while the thermal optimization potential is high when considering various system design parameters such as mass flow rate and air leakage. The performance assessment revealed a significant improvement in the electrical performance, while the observed thermal performance is comparatively low. The operating temperatures of the modules are in an acceptable range, and therefore deterioration of performance is not expected. In summary, the observations in this work show that the module design studied has the potential to lower the levelized cost of electricity in addition to solving application-specific problems, paving the way for a standard building component.

Table of contents

List of figures

List of tables

Symbols

Roman Symbols

a_{cov}	Solar coverage rate [-]
a_r	Empirical shape parameter [dimensionless]
a_{self}	Self-consumption rate [-]
A	Surface area [m²]
A_{DUT}	Active PV solar cell area of the device under test $[cm^2]$
A_g	Gross collector surface area [m²]
A_p	Cross-sectional area of a pipe [m²]
A_{ref}	Active PV solar cell area of the reference device $[cm^2]$
c_p	Specific heat capacity $[J \cdot kg^{-1} \cdot K^{-1}]$
COP	Coefficient of performance [-]
d	Thickness [mm]
d_s	Thickness of the heat generation area [mm]
D_h	Hydraulic diameter [dimensionless]
EQE	External Quantum Efficiency [%]
E_{eff}	Effective irradiated solar energy [Wh]
E_{el}	Electrical energy [Wh]
f_D	Darcy friction factor [dimensionless]
$F_{d,grd}$	Diffuse ground reflection angular correction factor [dimensionless]
$F_{d,sky}$	Diffuse sky irradiance angular correction factor [dimensionless]

G	Area-specific global irradiance [$W \cdot m^{-2}$]
G_b	Beam normal irradiance [$W \cdot m^{-2}$]
G_d	Diffuse horizontal irradiance [$W \cdot m^{-2}$]
G_{eff}	Effective irradiance including angular-dependent optical losses [$W \cdot m^{-2}$]
G_{gr}	Diffuse ground reflection [$W \cdot m^{-2}$]
G_h	Global horizontal irradiance [$W \cdot m^{-2}$]
G_i	Global irradiance at the plane-of-array [$W \cdot m^{-2}$]
$G(\lambda)$	Spectral irradiance as function of wavelength [$W \cdot m^{-2}$]
I_0	Diode reverse saturation current [A]
I_L	Light-generated current [A]
$I_{SC}(\theta)$	Short-circuit current of a PV module as a function of AOI [A]
$I_{SC}(0°)$	Short-circuit current of a PV module at $\theta = 0°$ [A]
$I_{SC,ASR}$	Short-circuit current calculated by using $SR(\lambda, \theta)$ [A]
J_{SC}	Short-circuit current density of a PV solar cell [$A \cdot mm^{-2}$]
L	Length of the rear ventilation air duct [m]
$\dot{m}$	Specific mass flow rate [$kg \cdot s^{-1}$]
M_a	Mach number [-]
n_1	Refractive index of the first medium at the interface [dimensionless]
n_2	Refractive index of the second medium at the interface [dimensionless]
n_r	Number of parallel air duct rows [-]
n_s	Number of cells in series [dimensionless]
N_D	Diode ideality factor [dimensionless]
p	Pessure [Pa]
p_{el}	Area-specific electrical power [$W \cdot m^{-2}$]
p_f	Pessure drop due to friction [Pa]

PR	Performance Ratio [-]
P_0	PV power output at STC [W]
P	Wetted perimeter [dimensionless]
P_{abs}	Absorbed power after optical losses [$W \cdot m^{-2}$]
P_{el}	Electrical power [W]
P_{th}	Thermal power [W]
$\dot{q}$	Specific heatflux [$W \cdot m^{-2}$]
$\dot{q}_{conv}$	Heatflux densitiy of convective heat transfer [$W \cdot m^{-2}$]
$\dot{q}_{eff}$	Effective area-specific heat flux density [$W \cdot m^{-2}$]
Q_{th}	Area-specific thermal energy [$Wh \cdot m^{-2}$]
$Q_{th,e}$	Thermal energy [Wh]
Re	Reynolds number [dimensionless]
RH	Relative humidity [%]
R	Reflectance [dimensionless]
R_{DUT}	Shunt-resistance setting of the device under test [Ω]
R_{ref}	Shunt-resistance setting of the reference device [Ω]
R_s	Series resistance [Ω]
R_{sh}	Shunt resistance [Ω]
R^2	Coefficient of determination [dimensionless]
s	Air-gap size [mm]
SPF	Seasonal performance factor [-]
$SR(\lambda)$	Spectral responsivity as a function of wavelength [$A \cdot W^{-1}$]
$SR(\lambda, \theta)$	Angular-dependent spectral responsivity [$A \cdot W^{-1}$]
$SR_{ref}(\lambda)$	Absolute spectral responsivity of the reference device [$A \cdot W^{-1}$]
$SR_{DUT}(\lambda)$	Absolute spectral responsivity of the device under test [$A \cdot W^{-1}$]

t	Time interval [h]
T_a	Ambient temperature [°C]
T_f	Fluid Temperature [°C]
T_i	Air inlet temperature [°C]
T_m	PV module temperature [°C]
T_o	Air outlet temperature [°C]
T_s	Surface Temperature [°C]
T_{sky}	Sky temperature [K]
$U'0$	Combined heat loss coefficient [$W \cdot m^{-2} \cdot K^{-1}$]
$U'1$	Heat loss coefficient influenced by wind [$W \cdot m^{-3} \cdot s \cdot K^{-1}$]
$v_{i,w}$	In-plane wind speed [$m \cdot s^{-1}$]
v_w	Wind speed on a surface [$m \cdot s^{-1}$]
$\dot{V}$	Fluid volumetric flow rate [$m^3 \cdot h^{-1}$]
V	Voltage [V]
V_{DUT}	Measured signal of the device under test [V]
V_{ref}	Measured signal of the reference device [V]
V_{th}	Thermal voltage [V]

Greek Symbols

α	Heat transfer coefficient [$W \cdot m^{-2} \cdot K^{-1}$]
α_{abs}	Absorptance coefficient [dimensionless]
α_{front}	Front heat transfer coefficient [$W \cdot m^{-2} \cdot K^{-1}$]
β	Module surface tilt angle [°]
ε_r	Absolute roughness [μm]
η_{eff}	Effective thermal efficiency [dimensionless]
η_{el}	Electrical efficiency [dimensionless]

η_{th}	Thermal efficiency [dimensionless]
η	Efficiency [dimensionless]
γ	PV power temperature coefficient [%/K]
λ	Wavelength [nm]
λ_{c}	Thermal conductivity [$\text{W} \cdot \text{m}^{-1} \cdot \text{K}^{-1}$]
λ_{ec}	Equivalent thermal conductivity [$\text{W} \cdot \text{m}^{-1} \cdot \text{K}^{-1}$]
μ	Dynamic viscosity [$\text{Kg} \cdot \text{m}^{-1} \cdot \text{s}^{-1}$]
Φ	Angle between the zenith and a line from the center of sphere [rad]
Ψ	Angle from north for a line from the center of spehere [rad]
ρ	Volumetric mass density [$\text{kg} \cdot \text{m}^{-3}$]
τ	Transmittance [dimensionless]
$\tau(0°)$	Relative transmittance of a PV module at $\theta = 0°$ [dimensionless]
$\tau(\theta)$	Relative transmittance of a PV module as a function of AOI [dimensionless]
θ	Angle of incidence [°]
θ_1	AOI of the light ray onto the optical medium [°]
θ_2	AOI of the light ray into the optical medium [°]

Acronyms / Abbreviations

AC	Alternating current
AM	Air mass
AOI	Angle of incidence
ASHP	Air-source heat pump
ASHREA	American Society of Heating, Refrigerating and Air-Conditioning Engineers
ASR	Angular-dependent spectral responsivity
BIPV	Building-integrated photovoltaic
BIPVT	Building-integrated photovoltaic and solar thermal

BoM	Bill of materials
c-Si	Crystalline silicon
CAD	Computer-aided design
CAN	Controller Area Network
CEC	California Energy Commission
CFD	Computational fluid dynamics
CIRE	Cologne Institute for Renewable Energy
DC	Direct current
DHI	Diffuse horizontal irradiation
DHW	Domestic hot water
DNI	Direct normal irradiation
EL	Electroluminescence
EVA	Ethylene-vinyl acetate
FeO	Iron oxide
FPGA	Field Programmable Gate Array
FWHM	Full width at half maximum
GHG	Greenhouse gas
GHI	Global horizontal irradiation
IAM	Incidence angle modifier
IEA	International Energy Agency
LAN	Local Area Network
LCOE	Levelized cost of energy
MBE	Absolute Mean Bias Error
MPP	Maximum point of power
NIR	Near infra-red

NTC	Negative temperature coefficient thermistor
PET	Polyethylene terephthalate
POA	Plane-of-array
PTB	Physikalisch-Technische Bundesanstalt
PV	Photovoltaics
PVT	Photovoltaic and solar thermal
RE	Residual Error
RMSE	Absolute Roots Mean Square Error
RTD	Resiststance temperatur detector
SAHP	Solar assisted heat pump
SiO$_2$	Silicon dioxide
SMARTS	Simple Model of the Atmospheric Radiative Transfer of Sunshine
SR	Spectral Responsivity
STC	Standard test conditions
THK	Technische Hochschule Köln
TMY	Typical meteorological year
UV	Ultra-violet

Chapter 1

Introduction

The conversion of fossil fuels into electrical and thermal energy is associated with high greenhouse gas (GHG) emissions and contributes significantly to global warming. In studies by climate researchers, without further efforts, by the year 2100, the greenhouse effect is estimated to cause an increase in temperature of up to 5 °C compared to the pre-industrial age [1]. The consequences of the rise in temperature include flooding, droughts and a rise in sea level. Therefore, in the COP 21 Agreement in Paris, the parties to the United Nations Framework Convention on Climate Change have agreed to a target to significantly lower the limit of global warming to below 2 °C [2]. A rapid transformation of the global energy system, moving away from the use of fossil fuels towards 100% renewable energy sources, is therefore essential.

1.1 Motivation

Solar energy is one of the most available energy sources on planet Earth, and electrical energy, as well as thermal energy, can be directly converted by photovoltaic (PV) and solar thermal systems. Regarding the building sector, and thus net-zero or low energy buildings, a reduction of GHG emissions can be achieved through the local use of renewable energy sources and efficient energy use. Application of these generating capacities in building roofs and façades can achieve greater acceptance from architects and house builders [3, 4]. Furthermore, building-integrated PV (BIPV) can greatly extend the potential installation capacities on building façades and roof covers, as shown in [5]. However, integrating PV into buildings has a decisive disadvantage regarding the performance of solar cells: Because there is no rear ventilation compared to mounted standard PV modules, solar cells, especially crystalline silicon ones (c-Si), show reduced electrical performance [6]. This raises the question of how the heat can be dissipated and how it is achieved. Combining BIPV and solar thermal system generation parts results in a hybrid system, also known as building-integrated photovoltaic and solar thermal (BIPVT) systems.

1.2   BIPVT modules and systems

By definition, a BIPVT module can be considered a hybrid solar energy generation system for electricity & heat production as well as an integral part of a building envelope, like a façade or a roof. The building is therefore incomplete without the BIPVT module, whereas the standard PV module and solar thermal collector represent an additional structure on an existing building or a roof [7]. For this reason, in addition to the energy function, other aspects like aesthetics and structural properties are taken into consideration in the production of BIPVT modules [8]. However, another distinction must be made between air- & water-based photovoltaic and solar thermal systems (PVT). Air-based systems are less complex and easier to implement, but they have disadvantages due to their lower efficiency in heat transfer. Therefore, these systems have lower thermal efficiencies in comparison to water-based systems. In contrast, thermal management, such as overheating protection, is more complex for water-based systems, as shown in [9]. This thesis focuses on a novel air-based BIPVT module presented in [10].

The fundamentals of air-based BIPVT modules are described in the following, using the improved module design under study as an example. These modules typically consist of two assemblies: A PV module and a housing, which contain the rear ventilation air duct. At the same time, the PV module is the thermal absorber for the solar thermal component, whose heat can be utilized. Therefore, the term glass package is used in this thesis for the PV module and thermal absorber as a combined component. Fig. 1.1 shows a three-dimensional model of the BIPVT modules under study in this thesis as well as an exploded assembly view of the glass package and aluminum housing. Yang and Athienitis

Fig. 1.1 Three-dimensional model of the BIPVT module design under study (top) and exploded assembly view (bottom) with glass package and aluminum housing. [10]

concluded in their review in [11] that studies about pre-fabricated BIPVT modules with easy as well as standardized installation and maintenance are lacking. The improved module design under study

addresses these topics. To allow access to the BIPVT modules without damaging the PV solar cells, the glass package is designed in a glass-glass configuration. This configuration, at the same time being small in size with a length × width × thickness of 339 mm × 293 mm × 7 mm, provides sufficient stability for accessibility, as presented in [10]. The glass package is mounted loosely in the aluminum housing, so it can still slide up and down to access the fastening elements and electrical interconnections of the BIPVT module after the roof has been covered. When the aluminum housing is opened, it can be used as climbing assistance to access the entire roof surface for installation and maintenance. In addition, the design enables easy replacement of individual modules.

The optimal PV c-si solar cell types and configurations, which are applicable for the small-scale design of the BIPVT module, were developed in [12]. Considered configurations are 4 × 5-inch full cells, 4 × 2 × 6-inch half-cut cells, 8 × 2 × 6-inch quarter-cut cells or different shingle cell technologies with theoretical power densities of 126 $W \cdot m^{-2}$, 147 $W \cdot m^{-2}$, 160 $W \cdot m^{-2}$ and 170 - 180 $W \cdot m^{-2}$, respectively. According to the optimal ratio of power density and cost efficiency, 2 × 8 quarter-cut PV solar cells with a theoretical power density of 160 $W \cdot m^{-2}$ are chosen.

Fig. 1.2 shows the cross-section of the individual layers of the glass package. The top and bottom
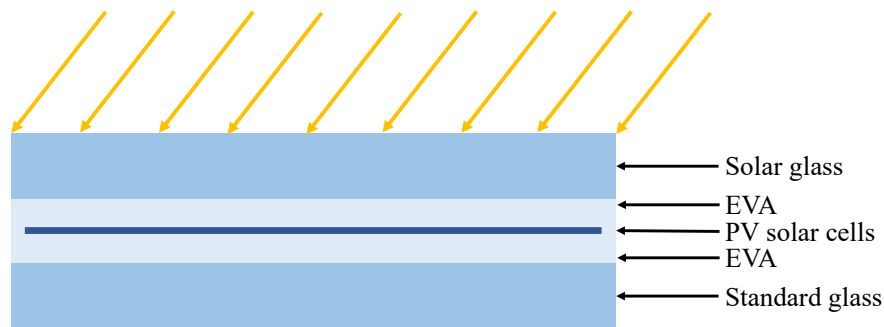
Fig. 1.2 Cross-section of the glass package layer structure of the BIPVT module under study.

layers are each soda-lime patterned glass, while the top layer is an ultra-white solar glass with high transmittance. The bottom layer is a standard soda-lime glass because no special transmittance properties are required. In the mid-section of the layer structure, the c-si solar cells are shown. These cells are embedded in two layers of ethylene-vinyl acetate (EVA) encapsulation material.

A significant disadvantage of BIPV modules is the lack of rear ventilation, which leads to higher PV solar cell temperatures and thus lower electrical efficiencies and a reduced lifespan of the materials. Passive rear ventilation for such systems has already been investigated and results in a minimal reduction in PV solar cell temperature [13]. Active rear ventilation leads to a higher energy consumption due to the fan, but also to a reduced PV solar cell temperature and hence a higher electrical efficiency. Accordingly, waste heat recovery is an effective measure to increase PV system efficiency, reduce GHG emissions in the building sector and reduce energy costs [14, 15].

Fig. 1.3 shows the cross-section of the air duct for rear ventilation of the BIPVT module under study. The air duct has dimensions with a length, height and width of 0.34 m × 0.02 m × 0.24 m, which results in a cross-sectional area of 0.0048 m². The glass package is actively rear-ventilated by the air duct system. On the bottom side of the BIPVT module, an inlet is placed through which the air flows in. On the top side, an outlet is placed through which the air flows to the air duct of the next module in series or to a manifold.
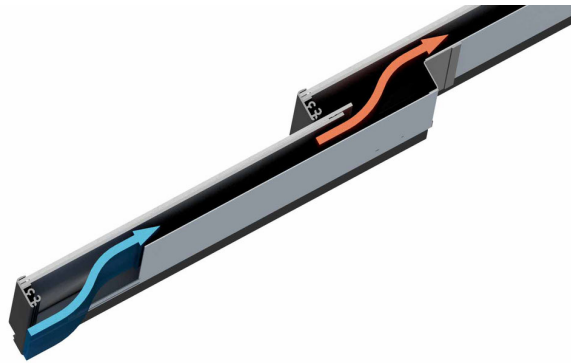
Fig. 1.3 Cross-section of the BIPVT module with a rear ventilation air duct on the rear side for heat utilization. [10]

In order to determine and assess the performance of BIPVT modules mounted on a building, it is necessary to consider the arrangement of the system. BIPVT systems are represented by connecting modules in series and strings in parallel. These parallel-arranged air duct systems are merged at the ridge onto a pipe and are connected to a fan. The fan actively draws the preheated air from the air duct system and can direct it to a heat exchanger of an air-source heat pump or directly to a water preheater. Such systems are operated slightly under atmospheric pressure, and thus air leakage in the transition area from one module to another has an influence on the systems performance. Through this leakage, cold ambient air streams into the air duct system and lowers the outlet temperature [16].

1.3   State of the art of BIPVT technology

Zondag et al. have published a very comprehensive review of PVT, including BIPV and BIPVT, in [17]. The review has shown that the first studies of air-based BIPVT were already conducted in the early 1990s because building integration had become more important. More interesting BIPVT reviews were presented by Quesada et al. in [18], Yang and Athienitis in [11], Debbarma et al. in [14] and Maghrabie et al. in [19]. A major disadvantage of BIPV is the lack of rear ventilation, which leads to an increase in PV solar cell temperature and thus a reduction in efficiency compared to standard PV systems. BIPVT systems tackle these problems by utilizing the heat from the PV solar cells. These reviews state a maximum increase of 10% in the electrical energy yield, due to the reduction of the

PV solar cell temperature by active rear ventilation compared to BIPV systems without active rear ventilation. BIPVT systems presented in the literature show a wide range of thermal efficiencies between $14\%_{abs}$ and $60\%_{abs}$. This can be attributed to many parameters. In particular, the mass flow row in the air duct system, the module design, the convective heat transfer coefficient of the absorber and the climate conditions of a specific location.

Based on review articles, a further classification of the BIPVT module and system under study can be done. It can be classified as an air-based, unglazed roof-integrated PVT module with mono-crystalline silicon PV solar cells and active rear ventilation in an open-loop system. In an open loop BIPVT system, the ambient air temperature is equal to the inlet temperature. The following studies examine optimizations, modeling and experimental measurements of modules and systems performance with this classification. Various designs of BIPVT modules for roof covering have been developed and analyzed in [20–31]. In order to analyze their electrical and thermal performance, different steady-state models have been set up and validated with experimental indoor and outdoor measurements. In addition, these models and experiments are used for energy & exergy analysis as well as performance assessment of air-based BIPVT modules and systems for roof coverage. The presented models are based on energy balance concepts and on equivalent circuits for the heat flows through the BIPVT module. However, the simulation accuracy of varying operating conditions in these models is limited since dynamic behavior is not represented. In addition, the presented models are customized and parameterized for the specific design, so these models can only be used for other designs to a very limited extent.

The authors in [32] presented a detailed overview of thermal and electrical air-based BIPVT performance models in the literature, and interested readers can refer to the article. Therefore, only the most recent and relevant publications are described in the following. A dynamic simulation model is required to obtain accurate results when considering changing operating conditions over the course of a day when simulating the electrical and thermal performance of a BIPVT system. Sohel et al. developed a dynamic simulation model for a PVT roof-integrated system under real operating conditions and validated it with experimental measurements in [33]. The analyzed PVT roof-integrated module consists of a thin-film PV module with 39 air channels for active rear ventilation. Moreover, the authors set up an electrical PV model to determine the electrical efficiency and energy yields. This model is based on the electrical efficiency at standard test conditions (25°C, $1000\mathrm{W\cdot m^{-2}}$, AM1.5G, STC) and simplified correction factors for cell temperature and irradiation. Despite simplifications, the electrical and thermal results are consistent with measurements and show a relative root mean square error (RMSE) between 2.2% and 4.2%. Nevertheless, the prediction accuracy of the electrical energy yields is limited to these simplified correction factors.

A further challenge in modeling the performance of a BIPVT system is to take into consideration the interaction between electrical and thermal energy cogeneration. Delisle et al. presented a performance assessment of an air-based BIPVT module, whose design is based on PV cells and absorber surfaces in alternate rows, in [34]. In order to analyze and assess the BIPVT module, a transient thermal and electrical model has been set up. The open-circuit voltage temperature coefficient model was used to

achieve the PV cell temperature as an input for the thermal model. The PV model is based on the power temperature coefficient model, which considers variations in PV solar cell temperature and solar irradiation compared to the electrical performance at STC. A maximum temperature rise of 38°C for a wind speed of $5 \text{ m} \cdot \text{s}^{-1}$ was observed in experimental measurements and indicated good agreement with the simulation model.

A few BIPVT systems are used for heat recovery in the building with hot water heat exchangers or air-source heat pumps. De Keizer et al. developed and validated a thermal simulation model for an air-based BIPVT system coupled to a modified air-source heat pump (ASHP) for different airflow configurations and heat transfer materials in [35]. However, the heat pump system is simulated, and therefore no experimental data on heat pumps in combination with BIPVT systems is available.

An increase in overall efficiency can be expected primarily through optimization of the geometry of the rear ventilation air duct, operating strategies and innovative materials. In the work of Wajs et al., air-based BIPVT modules are optimized by varying depths in [36, 15]. They conducted an experimental study on energy & exergy performance with measurements in the laboratory. The results showed a maximum thermal efficiency of 27% and an overall efficiency of 32%. Moreover, an increase of 9.5% in electrical efficiency by cooling the PV solar cells can be observed. However, the results are limited to measurements in the laboratory and steady-state operating conditions.

Another innovative application for BIPVT roof coverage is represented in the use of unmanned air vehicle shelter hangars, as demonstrated by Bot et al. in [37]. In order to analyze the BIPVT module under real operating conditions, a transient simulation model was setup with a lump mass. A maximum temperature rise of 9.2 °C was observed for the simulation period.

In a previous study, Fudholi et al. analyzed theoretical approaches for modeling air-based BIPVT modules based on the energy balance concept and concluded that some of these models have good agreement in terms of theory and experiment. The accuracy obtained depends significantly on the choice of the mathematical model and the key parameters of the BIPVT module design. Thus, the analyzed models are very limited when the key parameters of the system are inaccurate, as observed in [38]. A prior work by Meisenzahl et al. concluded in [39] that for glazed roof-integrated PVT modules, the optical optimization potential in terms of textured glass covers is very limited.

Debbarma et al. concluded in their review in [14] that there is a research gap in the field of BIPVT systems in the building sector and that there are only very few studies about the utilization of such systems. By analyzing the current state of unglazed BIPVT, it can be concluded that no studies have investigated optimization potential in terms of reduction of optical losses as a function of the angle of incidence (AOI). Studies that address angular-dependent optical losses are focused on PV modules without heat utilization. Furthermore, the impact of different aesthetic appearances on different front covers has not been considered in the previous studies. Several studies presented electrical performance and optical models with a low level of detail. Analyzing optical optimizations with these models is very limited, and thus accurate models must be developed. It has been shown that accurate thermal models of BIPVT systems with a high level of detail already exist, but the accuracy of the simulations is strongly dependent on the custom design parameters of the module and system.

Therefore, an adaptation of the state-of-the-art thermal simulation models for the analyzed BIPVT module design presented in [10, 40] and studied in this thesis is essential to assessing optimizations in terms of mass flow rate and air leakage variation. Nevertheless, there are only very few studies that consider the air leakage mass flow rate between the single BIPVT modules and air infiltration at the inlet in high detail. Finally, simulation models to analyze the optical and thermal performance optimization potential of custom-designed BIPVT systems with standardized electrical PV models are lacking in the literature.

1.4 Research objectives, approach and thesis structure

Three research topics and their respective objectives are defined for the analysis and optimization of BIPVT modules and systems based on the review are defined. Subsequently, the research approach is described. The research topics are each dedicated to a corresponding chapter of this thesis. In a broader context, the research objectives are related to the required actions of the International Energy Agency (IEA): Solar heating and cooling programme Task 56, "Building Integrated Solar Envelope Systems for Heating, Ventilation and Air Conditioning and Lighting: Manufacturers - To offer customizable architectural appearance" in [41]. In addition, the research objectives address the actions of the IEA Photovoltaic Power System Programme Task 15 in terms of solutions for aesthetic issues of BIPV systems, especially for colored BIPV, as reported in [42].

1.4.1 Optical and thermal modeling and analysis

Enabling the BIPVT module to generate electricity at a competitive levelized cost of energy (LCOE) on house roofs with suboptimal orientation, such as east and west-facing roofs, or tilt angle, the AOI performance must be optimized. The AOI performance is essentially dominated by the first surface on which the solar irradiation is incident. The relative transmittance $\tau(\theta)$, also known as the incidence angle modifier (IAM) in [43, 44], is normally used to account for reflectance losses at the glass-air interface. In order to analyze and assess the optical optimizations achieved by textured solar glasses and coatings, a detailed IAM loss model has to be integrated into a BIPVT simulation model. The studies in [45–47] revealed colored front covers with comparatively high transmittance rates. These front covers represent an optimization of the aesthetic appearance and can thus achieve greater acceptance by architects and building professionals. Nonetheless, these colored front covers decrease the amount of incident irradiation on the PV solar cell and thus cause increased optical losses in comparison to standard glass. In order to quantify these losses and predict the performance of modules with colored glasses, suitable models must be developed and validated. A more comprehensive literature review and description of research gaps are presented in Section 3.4.

Optimizations of the electrical and thermal energy yield are realized by adjustments of the mass flow in the air duct system and in the air leakage, as shown in [29, 31, 48]. These optimizations allow for more effective cooling of the PV cells, and hence more heat is transferred from the glass package to the

heat transfer fluid. To analyze the influence of these optimizations, it is necessary to apply appropriate models in a simulation framework. A recent study in [14] revealed a lack of flexible simulation frameworks to study BIPVT systems and identify optimization potential. Therefore, a simulation framework including optical, electrical and thermal models is to be developed and validated.

Previous studies by Getu et al. in [49], Roeleveld et al. in [50] and Bot et al. in [37] confirm that computational fluid dynamic (CFD) models are suitable to analyze the airflow, pressure drop and temperature contour profiles and derive modeling parameters of BIPVT modules and systems. Modeling air leakage and air infiltration is another particular challenge for air-based BIPVT modules. Delisle et al. defined the air leakage for the top- and back-surfaces of a BIPVT module with an equal mass flow in [28]. A different mass flow between the top side of the ambient and the back side of the roof can be expected and is taken into account in the simulation model to be developed.

The first research objective is therefore to answer the question of how the improved BIPVT module under study can be modeled in order to analyze the annual performance and quantify optimization potential. Suitable models are developed and integrated into a simulation framework to determine the overall performance of the module. Therefore, modeling parameters are derived from small-scale laboratory measurements and CFD simulations. In the development of this framework, a high level of detail is considered to evaluate optical and thermal optimization potential. Finally, the simulation framework is validated by large-scale field measurements with the improved BIPVT system.

The second objective in this research area is to answer the question of how to accurately simulate the AOI performance of colored modules. Therefore, an optical model using angular-dependent spectral responsivity measurement data is developed and validated by field measurements.

1.4.2   Optical and thermal optimization

Optical losses in terms of the AOI have an influence on the overall performance of BIPVT modules. A promising approach are nano-imprinted textures that reduce these losses and are easy as well as cost-effective to apply, as studied in [51, 52]. However, these studies focus on measurements of material properties and do not consider the reduction of annual AOI losses under outdoor AOI distribution. In order to quantify the influence of these textures on optical losses, time series simulations using measured IAM curves are required.

Beyond increasing the thermal efficiency and thus improving the heat utilization, the thermal optimizations can also affect the electrical performance by reducing the PV cell temperature. On the contrary, the electrical energy consumption of the fan increases with an increasing mass flow rate in the air duct system. In order to optimize the overall efficiency of BIPVT systems, the optimal mass flow rate must be determined by taking into account the energy consumption of the ventilation system and the reduction of PV cell operating temperature. Therefore, several studies in [53–56] recommend the effective efficiency approach to determine the optimal mass flow rate for solar air heating systems with a given module design. However, studies using this approach for air-based BIPVT systems are lacking.

The second research objective intends to answer the question of how the optical and thermal optimizations impact the performance of BIPVT modules. Therefore, annual simulations of the effective irradiance at two locations and various tilt angles are performed to quantify the detailed reduction of angular-dependent optical losses. Also, the effective thermal efficiency is simulated for a wide range of rear ventilation operating conditions for the improved module design with and without air leakage.

1.4.3 Assessment of measured and simulated energy yields

The authors in [11] identified that performance studies of improved BIPVT module designs using experimental and numerical approaches are an important research need. The third research objective is therefore to assess the measured and simulated annual energy yields of the improved BIPVT module design in a system. The measurements are done under real operating conditions in a large-scale outdoor experiment. To assess the thermal and electrical performance, weather data and characteristic values such as power output, module temperature, air outlet temperatures and mass flow rate of the test system are monitored. The experimental measurements are carried out for a period of one year in order to analyze also the seasonal influences. The experimental performance assessment includes the determination of Performance Ratio (PR), electrical yield increase by active PV cell cooling, steady-state thermal efficiency and coefficient of performance (COP) of the BIPVT system coupled to a heat pump. Moreover, the test system is compared with a reference system with conventional devices. In addition, the recorded measurement series data is used to validate the developed BIPVT simulation model and analyze the temperature characteristics of the system.

The validated models are integrated into a simulation framework to perform a case study and assess the improved BIPVT module design. The case study includes typical meteorological year (TMY) data and demand load profiles to calculate the characteristic values of BIPVT systems. These values include overall efficiency and energy yield, solar coverage rate, self-consumption rate and seasonal performance factor (SPF).

Chapter 2

Fundamentals

2.1 Optical and solar irradiance modeling

The effective solar irradiance supposed to be absorbed by the BIPVT module is derived by different methods. Firstly, the solar global irradiation incident on the plane of array of the module surface can be determined by measurement devices such as thermopile pyranometers, photodiode pyranometers or PV reference cells. In particular, these measurement data can be used to assess the field performance of a specific system under investigation. Secondly, available weather data sets can be used for the prediction of BIPVT systems energy yield at different locations. These data sets typically include measurements of the Global Horizontal Irradiation (GHI) provided by thermopile pyranometers. Thirdly, more detailed data sets include measurements with a pyrheliometer and pyranometer on a dual-axis tracker to provide the following components: Direct Normal Irradiation (DNI) and Diffuse Horizontal Irradiation (DHI), respectively. However, the availability of these irradiation components is required to account for optical losses in detail in order to predict accurate energy yields for different locations. Accordingly, the global irradiance on the plane-of-array (POA) G_i can be calculated by the sum of the respective in-plane irradiance as

$$G_i = G_{i,b} + G_{i,d} + G_{i,gr},\tag{2.1}$$

where $G_{i,b}$, $G_{i,d}$ and $G_{i,gr}$ are the in-plane direct, diffuse sky and diffuse ground reflected irradiance, respectively.

2.1.1 Incidence Angle Modifier simulation models

The rated power specifications in data sheets for PV modules and solar cells refer to STC. These STC measurements are performed at perpendicular irradiance, so there is no possibility to determine the oblique behavior. The IAM provides a way to determine performance for a wide range of AOI. The AOI θ is calculated by the respective sun position as well as the tilt angle β and azimuth orientation of a PV module. Firstly, it is introduced how the IAM is defined and measured. This is followed by

the introduction of various simulation models used to develop IAM predictions as well. Likewise, it is explained what influence the first layer has on the IAM of PV modules, as this has decisive implications for the assessment of optical optimizations.

The measurement of the relative transmittance $\tau(\theta)$, also known as IAM, is part of the standard IEC 61853-2 and is used to consider oblique behavior in the performance evaluation of PV modules [57]. The short-circuit current $I_{SC}(\theta)$ can be used to derive the $\tau(\theta)$ of PV modules, as this characteristic value is proportional to the amount of irradiance absorbed by the PV solar cells [8]. By means of an experimental setup as presented in [58, 39], the short-circuit current $I_{SC}(\theta)$ can be measured at different AOI θ and calculated as

$$\tau(\theta) = \frac{I_{SC}(\theta)}{I_{SC}(0°) \cdot cos(\theta)}. \tag{2.2}$$

$\tau(\theta)$: Relative transmittance of a PV module as a function of AOI [dimensionless]
$I_{SC}(\theta)$: Short-circuit current of a PV module as a function of AOI [A]
$I_{SC}(0°)$: Short-circuit current of a PV module at AOI=0° [A]
θ : Angle of incidence [°]

In (2.2) the IAM is calculated by the short-circuit current $I_{SC}(\theta)$ at various θ divided by the $I_{SC}(0°)$ and the cosine of the respective AOI. A cosine correction is applied to take into account the reduced incidence of light due to geometric influences.

Various simulation models to determine the IAM by means of material properties (Physical model [16]) and curve shape parameters (ASHREA model [59, 60], King et al. [61–63], Martín and Ruiz [64–66]) are developed. Martín and Ruiz developed an analytical model for the IAM to simplify the calculation of reflectance losses in simulation tools [64–66]. This model is recommended by the IEC 61853-2 standard to simulate IAM curves for standard PV modules based on an empirically determined shape parameter and indicates the most suitable prediction for standard solar glasses [57]. The simulation model is based on the following analytical equation

$$\tau(\theta) = \frac{1 - \exp(\frac{-\cos\theta}{a_r})}{1 - \exp(\frac{-1}{a_r})}. \tag{2.3}$$

a_r : Empirical shape parameter [dimensionless]

In this equation, the a_r represents a shape parameter to be determined empirically by experimental measurements, which is dependent on the AOI, module technology and the air/glass interface. Typical values of a_r range from 0.16-0.17 for standard PV modules up to 0.20 for soiled surfaces [64–66].

2.1.2   Diffuse irradiance angular correction factor

A crucial distinction in the application of these simulation models must be made with regard to the direct and diffuse irradiance components. The measured data from the IAM can be used analogously to model the angular reflection losses of the diffuse irradiance component on the front surface of a PV module. Since the solar rays of the diffuse irradiance are mostly isotropic and therefore hit the module surface from a wide range of the AOI, a suitable modeling approach is required. Models to account for these losses have been developed in [65, 67]. These models integrate the IAM from the measurements over a wide range of AOI of the respective diffuse irradiance and combine it into an angular correction factor F_d. The F_d is divided into separate fields of view: Diffuse sky $F_{d,sky}$, horizon $F_{d,hor}$ and ground reflectance $F_{d,grd}$.

The numerical method in [67] can be used with different IAM models as well as interpolation methods in order to calculate the diffuse angular correction factors. The factors are calculated for a fixed tilt angle β of the PV module as

$$F_d = \frac{\sum_{\Phi=\pi}^{\Phi=0} \sum_{\Psi=2\pi}^{\Psi=0} F(\theta) \cdot cos(\theta) \cdot dA_s}{\sum_{\Phi=\pi}^{\Phi=0} \sum_{\Psi=2\pi}^{\Psi=0} cos(\theta) \cdot dA_s}, \tag{2.4}$$

where Φ and Ψ are the respective angles in radians defined in a Φ-Ψ-coordinate system, and A_s is the projected area surface. This method applies for diffuse sky irradiance in the $\theta < \frac{\pi}{2}$ and $\Phi \le \frac{\pi}{2}$ range. In contrast, the diffuse ground reflected irradiance is considered within the $\theta < \frac{\pi}{2}$ and $\Phi \ge \frac{\pi}{2}$ range. The analytical approximation from [65] can be used to calculate an AOI correction factor for the diffuse component F_d based on a_r and fitting parameters. This approach is used in the standard IEC 61853-3 and assumes an isotropic diffuse irradiance distribution. Accordingly, the fitting parameters defined in the standard are used. The angular correction factors for diffuse sky and ground components are defined as:

$$F_d, sky/grd = 1 - \exp[-\frac{1}{a_r}(\frac{4}{3\pi}(s_{1/2})$$
$$+ (0.5a_r - 0.154)(s_{1/2})^2)] \tag{2.5}$$

$$s_1 = \sin(\beta) + \frac{\pi - \beta - \sin(\beta)}{1 + \cos(\beta)}$$

$$s_2 = \sin(\beta) + \frac{\beta - \sin(\beta)}{1 - \cos(\beta)}$$

In these equations β represents the tilt angle of the respective PV module under investigation. Accordingly, a diffuse correction factor F_d by (2.5) is considered for these irradiance components, respectively.

King et al. described an analytical equation to determine the effective irradiance considering optical loss factors for PV devices based on measurements and empirical correlations [61]. This model applies an IAM and a spectral correction factor to account for angle-dependent reflection and spectral

mismatch losses, respectively. Accordingly, the IAM correction factors can be applied to (2.1) to calculate the effective irradiance G_{eff}. The effective irradiance that can be absorbed by the PV module is defined as

$$G_{eff} = G_{i,b} \cdot \tau(\theta) + G_{i,d} \cdot F_{d,sky} + G_{i,gr} \cdot F_{d,grd}, \tag{2.6}$$

where $\tau(\theta)$, $F_{d,sky}$ and $F_{d,grd}$ are the correction factors for the direct, diffuse sky and ground reflected irradiance, respectively.

2.2   Thermal modeling of BIPVT modules

2.2.1   Energy balance of a BIPVT module

In order to analyze the energy yields and optimizations of the BIPVT system, a numerical performance model based on energy balance and heat transfer is set up. Helmers and Kramer [68] developed a multi-linear performance model for PVT modules and validated it with outdoor measurements. The performance model indicates a good agreement and therefore it is applied as a reference for determining the energy balance of the BIPVT module. They described a two-node model in which thermal energy transfer to the fluid is separated from electrical energy transfer by a thermal transmittance U_{fluid}.

The basic energy balance for the BIPVT module adapted according to Helmers and Kramer [68] is shown in Fig. 2.1. The effective heat flux density $\dot{q}_{eff}$ is derived from the energy balance and
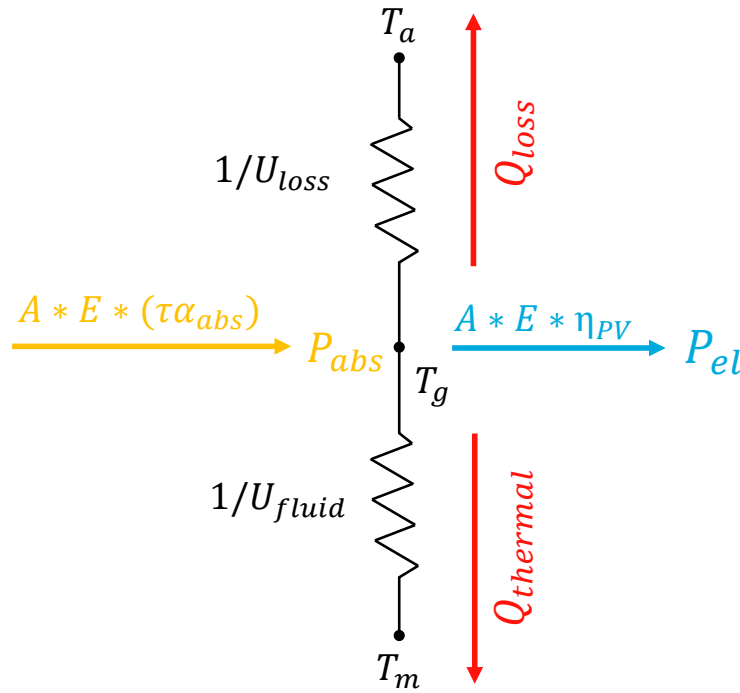
Fig. 2.1 Basic energy balance of a roof-integrated PVT module adapted from Helmers and Kramer [68].

represents the available absorbed power P_{abs} of the glass package after optical losses on a specific area A. This area-specific heat flux density $\dot{q}_{eff}$ can be simplified as

$$\frac{P_{abs}}{A} = \dot{q}_{eff} = G \cdot ((\alpha_{abs} \cdot \tau) - \eta_{PV}). \tag{2.7}$$

P_{abs} : Absorbed power after optical losses [W]
$\dot{q}_{eff}$: Effective area-specific heat flux density [$W \cdot m^{-2}$]
G   : Area-specific global irradiance [$W \cdot m^{-2}$]
α_{abs} : Absorptance coefficient [dimensionless]
τ : Transmittance [dimensionless]
η_{el} : Electrical efficiency [dimensionless]
A   : Surface area [m]

While G is the area-specific perpendicular global irradiance and τ is the optical energy transmittance trough the solar glass laminate. The absorptance coefficient of the glass package is represented by α_{abs} and the electrical efficiency of the PV solar cells by η_{PV}.

2.2.2   Convective heat and radiation transfer of the front surface

In this subsection the energy transfer to the environment U_{loss}, which is not utilizable by the BIPVT module, as shown in Fig. 2.1 is determined by empirical correlations. Quantifying the heat transfer with the ambient air temperature T_a due to convection by a given wind speed on the top surface of the BIPVT module requires assumptions of the heat transfer coefficient α_{front}. Models of already well documented experimental measurements are applied due to the expensive and time consuming nature of these experiments.

McAdams [69] conducted experimental wind tunnel tests with a 0.5 m $\times$ 0.5 m flat plate and found a empirical correlations for the heat transfer coefficient α. It is calculated by the analytical equations (2.8) and (2.9) as a function of the wind speed v_w on the flat plate.

$$\alpha = 5.7 + 3.8 \cdot v_w \quad for \quad v_w < 5m \cdot s^{-1} \tag{2.8}$$

$$\alpha = 6.47 \cdot v_w^{0.78} \quad for \quad v_w > 5m \cdot s^{-1} \tag{2.9}$$

α : Heat transfer coefficient [$W \cdot m^{-2} \cdot K^{-1}$]
α_{front} : Front heat transfer coefficient [$W \cdot m^{-2} \cdot K^{-1}$]
v_w : Wind speed [$m \cdot s^{-1}$]

Laemmle et al. examined the application of high-transmissive low-emission coatings to optimize water-based high efficiency PVT modules and stated an emissivity ε of 0.915 for collectors without low-emission coating [70]. Accordingly, this value is used for the simulation of the BIPVT module. Analogously to the heat transfer coefficient, the heat radiation transfer with the sky is to be determined. An empirical analytical correlation for the sky temperature is therefore necessary, which is calculated with the respective ambient temperature T_a. According to Swinbank [71] the sky temperature can be

calculated by the analytical equation (2.10).

$$T_{sky} = 0.0552 \cdot T_a^{1.5} \tag{2.10}$$

T_{sky} : Sky temperature [K]
T_a : Ambient temperature [K]

2.2.3   Thermal material properties of the glass package

In order to determine the material properties of the glass package for the simulation model, the density ρ, the specific heat capacity c_p and the thermal conductivity λ_c must be determined.

Table 2.1 Material properties of the glass package of the BIPVT module.

Material	λ_c $W \cdot m^{-1} \cdot K^{-1}$	c_p $J \cdot kg^{-1} \cdot K^{-1}$	ρ $K \cdot m^{-3}$	d mm
Glass 1	1	720	2500	3.2
EVA 1	0.311	760	920	0.9
c-Si	148	700	2500	0.2
EVA 2	0.311	760	920	0.45
Glass 2	1	720	2500	3

The material properties given in Table 2.1 are used for the calculations. To determine the density and specific heat capacity of the glass package, the equations (2.11) and (2.12) are used.

$$\rho = \frac{\sum_{i=1}^{n}(\rho_i \cdot d_i)}{\sum_{i=1}^{n} d_i} \tag{2.11}$$

ρ : Density $[kg \cdot m^{-3}]$
d   : Thickness [mm]

$$c_p = \frac{\sum_{i=1}^{n}(\rho_i \cdot d_i \cdot c_{p,i})}{\sum_{i=1}^{n}(\rho_i \cdot d_i)} \tag{2.12}$$

c_p : Specific heat capacity $[J \cdot kg^{-1} \cdot K^{-1}]$

According to Boeckh and Wetzel [72] the equivalent heat conductivity for the glass package can be

calculated by (2.13).

$$\lambda_{ec} = \frac{\sum_{i=1}^{n} d_i}{\sum_{i=1}^{n} \left(\frac{d_i}{\lambda_{c,i}}\right)} \tag{2.13}$$

λ_{c} : Thermal conductivity $[\text{W} \cdot \text{m}^{-1} \cdot \text{K}^{-1}]$
λ_{ec} : Equivalent thermal conductivity $[\text{W} \cdot \text{m}^{-1} \cdot \text{K}^{-1}]$

2.2.4   Convective heat transfer to the fluid

Heat is transferred between surface and fluid by convection, which is distinguished between free convection and forced convection. In the case of free convection, the flow is caused by temperature and density differences, and in the case of forced convection, it is caused by pressure differences. The heat flux density is calculated using (2.14), where α is the heat transfer coefficient, T_F is the fluid temperature and T_S is the surface temperature [72].

$$\dot{q}_{conv} = \alpha(T_F - T_S) \tag{2.14}$$

2.2.5   Determination of thermal power, energy and efficiency

A significant indicator to be determined in order to analyze and assess optimizations of BIPVT modules and systems is thermal performance and efficiency. The air mass flow rate $\dot{m}$ of the rear ventilation outlet is determined with the volumetric mass density ρ of air and fluid flow rate $\dot{V}$ as

$$\dot{m} = \rho \cdot \dot{V}. \tag{2.15}$$

The specific thermal power of the air collected from the rear ventilation of the BIPVT system can be calculated taking into account the temperature difference between the air inlet T_i and air outlet T_o as

$$\dot{q}_{th} = \frac{\dot{m} \cdot c_p \cdot (T_o - T_i)}{A}, \tag{2.16}$$

where $\dot{m}$ is the mass flow rate, c_p is the specific heat capacity of air and A is the total irradiated gross area of the module. The specific thermal energy of the system can be calculated as

$$Q_{th} = \int \dot{q}_{th} \, dt, \tag{2.17}$$

where q̇$_{th}$ is integrated over the time. The thermal efficiency η_{th} represents the ratio between the useful heat dissipated by the airflow and the solar irradiance and can be calculated as

$$\eta_{th} = \frac{\dot{q}_{th}}{G},$$ (2.18)

where G is the incident solar irradiance [15, 36]. Analogous to these equations, the electrical energy E$_{el}$ and efficiency η_{el} are calculated using the area-specific electrical power in the maximum point of power (MPP) p$_{el}$.

2.3 Electrical modeling of BIPVT modules

A detailed electrical model is required in order to analyze the PV performance of the BIPVT module. This model can be used to assess the optical and thermal optimizations. Moreover, the cooling effect due to the air duct can be quantified.

The electricity generation of PV solar cells, modules or systems can be determined by simple analytical expressions or voltage-current relationships. These relationships are derived of a single diode equation circuit model based on five parameters. In previous works, the electrical model of air-based BIPVT modules are expressed by simple analytical equations related to the electrical efficiency in the MPP [15]. More detailed models are considering the temperature dependency as function of mean PV cell temperature [34, 70, 62, 63]. The application of a current-voltage relationship provides the highest level of detail, but is more sensitive and elaborate in parameterization. However, in order to determine accurate electrical energy yields this modeling approach is recommended in the IEC standard 68153 for module testing and energy rating [73].

2.3.1 Five-parameter model for PV performance estimation

In order to predict electrical energy yields of PV modules under real operating conditions, the single diode equivalent circuit is an accurate and reliable model. This model is usually based on five parameters and expressed by (2.19) [74]. The five parameters: diode reverse saturation current I$_0$, light-generated current I$_L$, series resistance R$_S$, shunt resistance R$_{sh}$ and ideality factor parameter - each for a certain operating point, are needed to estimate the I-V curve of a PV module. The modified ideality factor parameter in (2.19) includes the number of cells in series N$_s$, the ideality factor n and the cell thermal voltage V$_{th}$. V$_{th}$ consists of the Boltzman's constant k$_B$, the temperature of the p-n junction T$_C$ divided by the electron charge q [74].

$$I = I_L - I_0 \left[\exp\left(\frac{V + I \cdot R_s}{N_D \cdot n_s \cdot V_{th}}\right) - 1 \right] - \frac{V + I \cdot R_s}{R_{sh}}$$ (2.19)

Five parameters are required to solve the single diode equivalent circuit equation of the PV module under investigation for the respective effective irradiance and cell temperature. De Soto et al.

presented a reliable and easy-to-use method to determine these five parameters by semi-empirical equations. Therefore, based on the I-V curve measurement at STC, the current-voltage relationship can subsequently be determined according for any other operating point [75].

2.3.2   Photovoltaic module and cell temperature models

Thermal models to predict the PV module and cell temperature are described by Fuentes [76], King et al. [62] and Faiman [77]. However, the IEC 61853 standards for performance testing and energy rating recommend the module temperature determination by the Faiman model [77, 57]. The module temperature T_m is derived according to this model in (2.20), taking into consideration variations in wind speed v_w and the in-plane irradiance G_i [77].

$$T_{mod} = T_{mod} + \frac{G_i}{U_0' + U_1' \cdot v_w} \tag{2.20}$$

Both constant coefficients U_0' and U_1' describe the heat loss of the modules in dependency of their optical efficiency as well as wind conditions and can deviate for different module types [77]. In this context, the heat loss coefficients for the solar modules on site are determined by using a least-squares fit approach as described by Faiman [77], based on in situ measurement data of the T_m, the corresponding weather and irradiation conditions.

2.3.3   Photovoltaic system inverter model

The PVWatts inverter model from the National Renewable Energy Laboratories (NREL) predicts the AC power output of a PV system. Briefly explained, the model estimates the inverters efficiency up to the nominal rated inverter efficiency θ_{Norm} as a function of the systems DC power output [78].

2.4   Spectral responsivity measurements of crystalline PV solar modules

Spectral responsivity $SR(\lambda)$ measurements are typically applied to determine insights of the wavelength dependent spectral loss effects of PV solar cells and modules. External and internal spectral loss effects like transmittance, reflectance and parasitic absorptance of a PV module are included in the spectral responsivity $SR(\lambda)$. It is measured by illuminating the PV device with monochromatic light of different wavelengths generated by a solar simulator with filter monochromator or grating monochromator. To determine the $SR(\lambda)$ of a PV module, the short-circuit current I_{SC} at each wavelength has to be measured. The measurement procedure for PV modules is defined in the standard IEC 60904-8 [79]. The spectral responsivity $SR(\lambda)$ is defined as a function of wavelength as the short-circuit current I_{SC} of a PV module divided by the spectral irradiance and the surface area of the

module [8]. Accordingly, it can be calculated by (2.21).

$$SR(\lambda) = \frac{I_{SC}}{G(\lambda) \cdot A} \tag{2.21}$$

$SR(\lambda)$: Spectral responsivity as a function of wavelength $[A \cdot W^{-1}]$
$G(\lambda)$: Spectral irradiance as a function wavelength $[W \cdot m^{-2}]$
A   : Surface area of a PV module $[m^2]$

Consequently, the short-circuit current I_{SC} can be represented by the integration of the $SR(\lambda)$ over the wavelength range up to the bandgap of c-si by (2.22).

$$I_{SC} = A \cdot \int_{300}^{1200} SR(\lambda) \cdot G(\lambda) d\lambda \tag{2.22}$$

2.4.0.1   Optical measurement setup for characterization of PV modules

The optical measurements in this thesis are performed with a modified measurement setup based on a solar simulator with filter monochromator for PV solar cells (FiMo SR EQE, Aescusoft). Fig. 2.2 shows the modified setup used, consisting of a solar simulator, an upstream optical chopper, two filter-monochromators, a sample stage with bias illumination, measurement equipment and a data acquisition system. The setup is divided into two rooms, which are only connected by an aperture for the light beam. The illumination source of the solar simulator is a xenon short-arc lamp (1000 W Osram XBO) connected to a stabilized DC power supply. The housing of the illumination source and DC power supply is water-cooled. The double filter monochromator contains 40 different bandpass filters and can hence provide a wavelength range from 300 to 1120 nm with a full width at half maximum (FWHM) of 25 nm [80]. The measuring beam of the solar simulator is guided directly through an aperture onto the measuring sample stage and irradiates an area of about 210×210 mm^2. A bias illumination, consisting of two tungsten halogen lamps for simulating outdoor conditions by setting an operating point and compensation of interferences, is mounted directly on the sample stage. The short-circuit current density J_{SC} of the PV solar cell under test is measured via the voltage drop across a low impedance shunt resistance and is transferred to a lock-in amplifier.

The rotation frequency of the optical chopper is measured continuously, using the lock-in amplifier, and then transmitted to a data acquisition system. The lock-in amplifier improves the signal-to-noise ratio by comparing the AC signal generated by the chopper with the DC signal from the bias illumination and the noise signal. This method allows to measure even the smallest short-circuit currents of PV solar cells [81].

The standard IEC 60904-8 recommends a reference cell calibrated against a primary reference for the measurement procedure of the absolute $SR(\lambda)$. A primary reference calibration is provided by very few accredited laboratories for other laboratories in industry and research [79]. For this thesis a reference cell calibration is provided free-of-charge by the European Telecommunications Standards
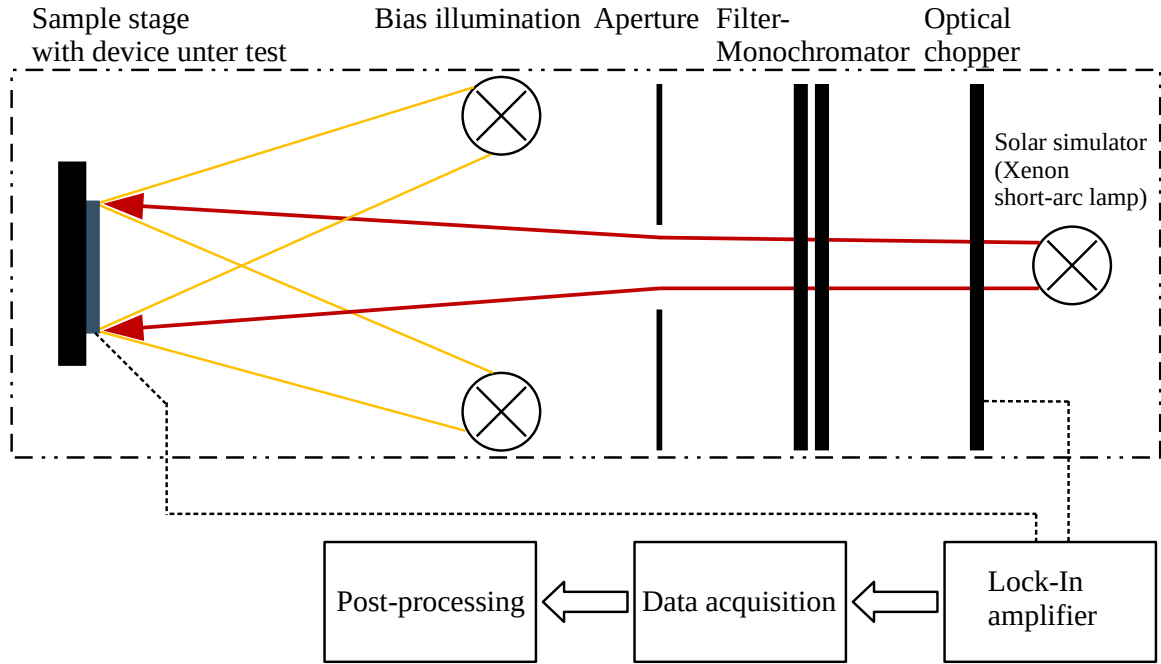
Fig. 2.2 Setup of the optical measurement test stand for angular broadband and spectral characterization of PV modules. [80]

Institute of the European Commission Joint Research Centre. Before the optical measurements are performed, a calibration of the used measurement setup is done by obtaining the perpendicular $SR(\lambda)$ of the reference cell. In the post-processing the calibration data and measurement signal is used to determine the absolute SR of the device under test according to (2.23) [80].

$$SR_{DUT}(\lambda) = SR_{ref}\frac{V_{DUT}}{V_{ref}} \cdot \frac{R_{ref}}{R_{DUT}} \cdot \frac{A_{ref}}{A_{DUT}} \tag{2.23}$$

$SR_{DUT}(\lambda)$: Absolute spectral responsivity of the device under test $[A \cdot W^{-1}]$
$SR_{ref}(\lambda)$: Absolute spectral responsivity of the reference device $[A \cdot W^{-1}]$
V_{DUT} : Measured signal of the device under test [mV]
V_{ref} : Measured signal of the reference device [mV]
R_{DUT} : Shunt-resistance setting of the device under test [mΩ]
R_{ref} : Shunt-resistance setting of the reference device [mΩ]
A_{DUT} : Active cell area of the device under test [cm^2]
A_{ref} : Active cell area of the reference device [cm^2]

2.5 Textured and colored solar glasses

The term solar glass covers both glass for photovoltaic and solar thermal applications. Due to its low manufacturing cost, high transmittance, mechanical properties and durability, all relevant solar glasses are made of soda-lime silicate glass [8]. This glass is typically composed of silicon dioxide (SiO_2) and is produced at low cost by adding lime and soda at a melting temperature of 1450°C. Standard soda-lime silicate glass has a high iron oxide (FeO) content by the nature of its raw materials. This high iron content leads to broad and strong absorptance in the near infra-red (NIR), which is particularly high in the 1100 nm wavelength range. This reduces the transmittance at this wavelength by up to 12%. The band gap of crystalline silicon is exactly in this wavelength range and therefore especially low iron raw materials are used for the production of solar glass. This glass with a thickness of 4 mm has a transmittance of around 91% and is designated extra-white. The spectral transmittance of solar glass contributes decisively to the generated power of a solar cell in a PV module [82]. Another essential aspect is that the FeO content is reduced by oxidation into Fe_2O_3. This is achieved by adding antimony pentoxide (Sb_2O_5) in the melting process. This process increases the transmittance of glass up to 91.5%, giving it the designation ultra-white. Due to the manufacturing process, this solar glass is only available as patterned glass. In the manufacturing process of float glass, the tin would also be oxidized by the Sb_2O_5 and preserve traces on the glass surface. Float glass flows over a hot tin bath after the glass is melted, providing it its mirror-smooth surface. Patterned glass is rolled directly after the glass melting at about 1000°C and gets its textured surface here. Next, solar glass is thermally toughened in a tempering furnace to increase its mechanical strength.

The differences between float and patterned glass during production and other advantages and disadvantages are not discussed in detail here. For more information, please refer to the literature of Blieske et. al [82].

2.5.1 Textured solar glasses

In order to improve the oblique light behavior of a PV solar cell, it is textured on the side facing the sunlight in an etching process, resulting in a so-called light-trapping effect. This effect leads to multiple reflectance of a light ray as well as a longer effective optical path length in the solar cell and thus increases the probability of being absorbed in the semiconductor [82].

This light-trapping effect is also used in textured solar glasses. The previously described rolling process enables the texturing of glass surfaces and is used for the production of textured and deep-textured solar glass. The main improvements of textured solar glasses in PV modules are the previously introduced light-trapping effect and a reduction of reflectance at the glass/air interface with oblique incidence of light.

Fig. 2.3 shows the light-trapping effect (A) and how multiple reflectance occur at the texture, increasing the probability that the light rays reach the PV solar cell. The light-trapping effect is represented by refractive light rays using the Snellius' law of refraction. Consequently, the refraction
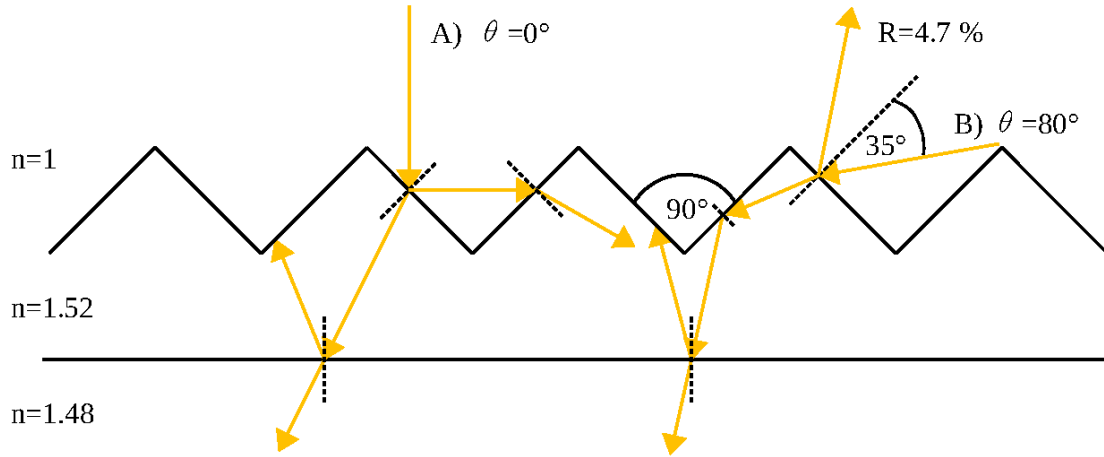
Fig. 2.3 Simplified geometric representation of deep-textured solar glass coupled with EVA (n=1.48, ([8], p. 75)). Example for the light-trapping effect and perpendicular incidence on the module plane (left, A) and oblique light incidence on the module plane (right, B) with reduced reflectance [82].

of light rays at the interface between two isotropic optical media can be determined by Snellius' law of refraction according to (2.24) [83].

$$\frac{\sin(\theta_1)}{\sin(\theta_2)} = \frac{n_2}{n_1} = const.$$ (2.24)

θ_1 : AOI of the light ray onto the optical medium [°]
θ_2 : AOI of the light ray into the optical medium [°]
n_1 : Refractive index of the first medium at the interface [dimensionless]
n_2 : Refractive index of the second medium at the interface [dimensionless]

Furthermore, the texture can lead to a reduction of the effective AOI on the glass surface despite oblique light incidence, as shown in Fig. 2.3 (B). Minimizing the AOI results in a reduction of reflectance, which can be determined for uniform polarized light by (2.25) [84].

$$R = \frac{1}{2} \cdot \frac{tan^2(\theta_1 - \theta_2)}{tan^2(\theta_1 + \theta_2)} + \frac{1}{2} \cdot \frac{sin^2(\theta_1 - \theta_2)}{sin^2(\theta_1 + \theta_2)}$$ (2.25)

Thus, the texture reduces the reflectance at an AOI of 80° on the module plane from roughly 39% to only 4.7%, compared to solar glass without texture.

Moreover, the light refraction of textured solar glass provides a homogeneous appearance of PV modules from an aesthetic point of view [58, 82].

Another promising technology to enhance the optical properties of solar glass for oblique light conditions are imprinted nano- and microtextures of UV-curable resin. These textures have dimensions from < 10 nm to > 1000 μm and are imprinted in a role-to-plate lithography process on solar glass

and polymer sheets. Veldhuizen et al. found that the nanotexture imprint reduces the spectral
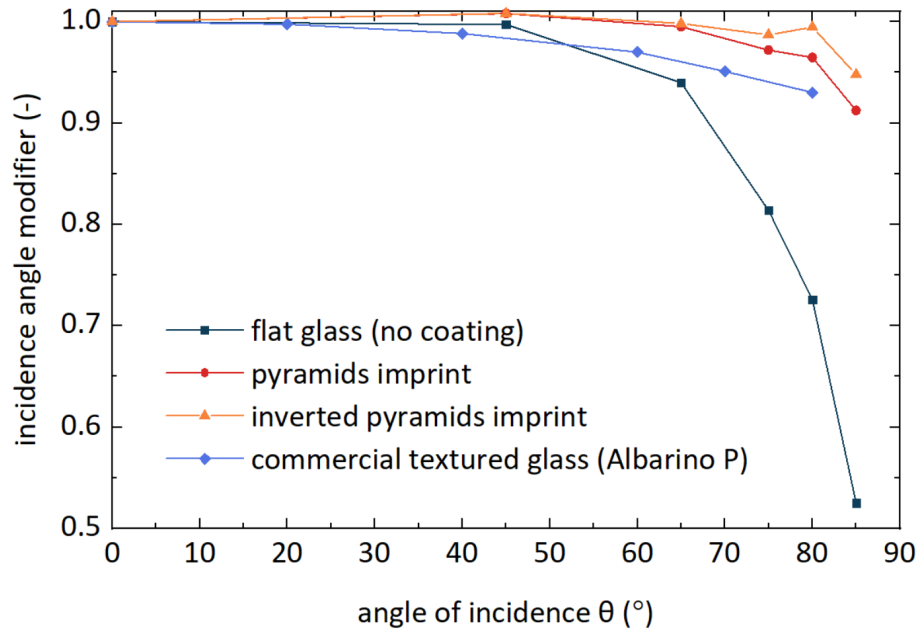
Fig. 2.4 IAM measurement comparison of deep-textured solar glass and solar glass with nano-imprinted pyramidal and inverted pyramidal textures. [51]

reflectance below 2% in a wide range of wavelengths and that the transmittance consists of 99% diffuse transmittance. Moreover, angular measurements of coated glass with pyramid- and inverted pyramid structure have revealed an IAM > 0.9 for AOI up to 85° as shown in Fig. 2.4 [51].

2.5.2   Colored solar glasses

The application of colored solar glass in BIPVT modules can enhance the aesthetic appearance of buildings and therefore achieve more acceptance at house builders and architects. On the other side, energy losses are caused by an increased reflectance of the respective color. In the following subsection, promising technologies of colored solar glasses with relatively high transmittance rates are introduced.

Jolissaint et al. presented a combination of two optical effects to achieve a colored appearance, by at the same time high transmissivity. An etching treatment of the front surface, faced towards the sun, creates a diffuse reflectance and transmittance. Diffuse reflectance, in comparison to specular reflectance, generates a surface which provides a matte appearance and prevents glare effects. In a field test, colored BIPV modules with this technology were installed on a test house in the building façade and roof to determine the energy loss in comparison to a black reference module. It can be observed that the energy loss shows a wide range from -16% up to -24% for green and gold colored modules, respectively [85].

Colored solar glasses inspired by the morpho-butterfly effect are another promising technology to customize aesthetics of building-integrated solar energy systems. Bläsi et al. presented an adoption of the morpho-butterfly-effect, which is a thin-film interference effect combined with a structure effect. Therefore, a thin film layer is applied by a combination of structuring and sputter coating on the inner surface of a solar glass. It has been observed that these colors have an excellent angular stability and reduced glare [45]. Kutter et al. investigated the power loss for this technology and found it is relatively low in comparison to ceramic print and colored encapsulants. A power loss between -7.2% and -3% for red and blue color is stated, respectively [46].

2.6   Statistical error metrics

In order to assess the prediction accuracy and quality of the developed simulation models in this thesis, suitable error metrics are introduced. First, the residual error (RE) is calculated by the difference between the measured n_{meas} and predicted value n_{sim} as

$$RE = n_{meas} - n_{sim}. \tag{2.26}$$

The RE in (2.26) represents the absolute difference between a single value in its corresponding unit. In contrast, Mean Bias Error (MBE) is used to evaluate the accuracy of predictions within data series and is based on the mean absolute difference as

$$MBE = \frac{1}{n} \sum_{i=1}^{n} (n_{meas,i} - n_{sim,i}). \tag{2.27}$$

The RMSE not only considers the positive or negative error, but also includes the significance of the deviation in its amplitude. The absolute RMSE is the root of the mean squared RE of all values of a

data set and expressed as

$$RMSE = \sqrt{\frac{1}{n}\sum_{i=1}^{n}(n_{meas,i} - n_{sim,i})^2}. \tag{2.28}$$

However, the error metrics in (2.27) and (2.28) are not related to the measured values and are therefore difficult to interpret. The MBE relative to the measured mean values can be expressed as follows

$$\Delta MBE = \frac{\frac{1}{n}\sum_{i=1}^{n}(n_{meas,i} - n_{sim,i})}{mean(n_{meas})} \tag{2.29}$$

and, analogously, the relative RMSE as

$$\Delta RMSE = \frac{\sqrt{\frac{1}{n}\sum_{i=1}^{n}(n_{meas,i} - n_{sim,i})^2}}{mean(n_{meas})}. \tag{2.30}$$

The developed BIPVT simulation model is validated with the relative MBE in order to determine the relative error of measured and simulated energy yields. The prediction accuracy of the model in terms of energy quantities can thus be evaluated. Moreover, the angular-dependent spectral responsivity model to simulate colored PV modules is assessed with these error metrics.

Chapter 3

Optical and thermal modeling of BIPVT modules

3.1 Development of an automated rotational sample stage

The investigation and characterization of light-trapping structures or coatings, which can optimize the oblique and low light performance of PV solar cells and -modules or aesthetic appearance, requires accurate indoor measurement equipment setup. Furthermore, reproducibility must be ensured, which allows the comparison of results from different samples and laboratories.

The standard IEC 61853-2:2016 defines the procedure of characterization of the angular losses of PV solar cells and -modules [57]. The standard recommends adjusting the AOI to the sample from the light source in an AOI range in between ±60° by minimum 10° steps and from ±60° to ±85° by 5° steps. Minimum three repeated measurements of the procedure should be performed to decrease the random errors. This procedure results in a minimum of 69 measurements for each sample, which is time-consuming and error-prone due to positioning errors. Therefore, an in-house developed automated rotation sample stage is developed in [86, 87]. This sample stage is used for angle-dependent measurements in this thesis in order to determine relative angular transmittance curves.

A previous interlaboratory comparison study has shown results vary in worst case deviation from -3% to +5% to the weighted mean in an AOI range of ±80° and even worst for AOI > 80° [88, 89]. Especially the accuracy of the rotation stage adjustment, offset adjustment from the rear side to the front of the PV solar cell and volume non-uniformity of the light source are common sources of error [90].

The technical realization of the automated rotation sample stage is shown (see Fig. 3.1) in a three-dimensional CAD model. The setup hardware consists of a mechanical construction connected to a stepper motor for the sample stage and a data acquisition system (NI cDAQ-9174, National Instruments). The data acquisition for the short-circuit current I_{SC} is realized with the measurement setup described in the previous Section 2.4. Module temperature monitoring during the measurement

A: Sample frame

B: Sample

C: Frame rail

D: Off-set rail

E: Connection shaft

F: Bearing

G: Base frame

H: Motor and motor flange
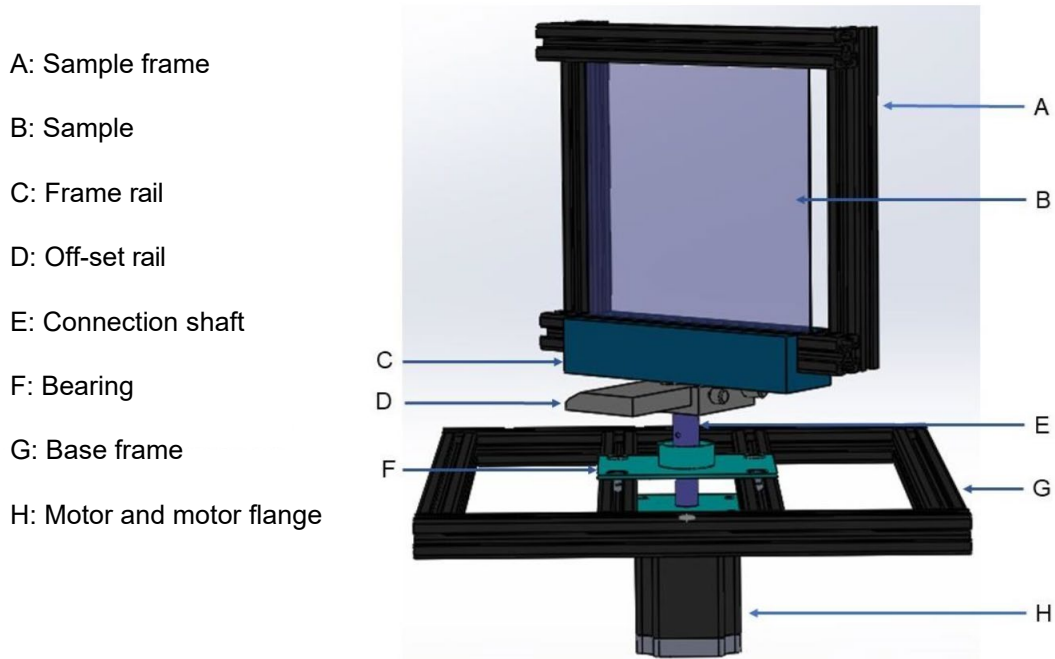
Fig. 3.1 Technical realization of the automated rotational sample stage. [86]

procedure is done by a standardized resistance temperature detector (RTD) with a dedicated module for the data acquisition system. Moreover, digital signal processing modules for adjustment of the rotation stage are used. The measurement data processing and control of the rotation stage adjustment are realized in the development environment LabView. The measurement data from both systems is then merged and post-processed. An optical encoder provides the positional feedback of the stepper motor, powered by a micro step driver, with a theoretical accuracy of 0.04°. In addition, a ferromagnetic ring encoder, to verify the adjusted angles of the rotation stage and to qualify the setup according to the standard IEC 61853-2 recommended accuracy, is installed. The calibration of the two encoders shows a fulfillment of the required rotation angle of ±1°.

A comparison to other laboratory measurement data of the exact same PV module sample is done to validate the developed automated rotation stage. Therefore, the measurement data of a sample with the exact same bill of materials (BoM) from the Physikalisch-Technische Bundesanstalt (PTB) is used for validation. Results of the interlaboratory comparison are shown in Fig. 3.2. It can be observed that the standard deviation of the developed fully-automated rotational sample stage and measurement setup is below 1% for an AOI range of ±80°. Angular SR measurements are rather uncommon and have been performed in only a few studies and by very few facilities [91, 92]. Therefore, the measurement procedure described in Section 2.4 is used with a rotational sample stage to setup different AOI.[1]

---

[1]Fragments of the following section are published in "Dynamic Simulation Model of an Air-Based BIPVT Roof Tile System" (Clasing et al., Proc. 8th World Conference on Photovoltaic Energy Conversion, Milan, Italy, 2022, pp. 662–665) in [93].
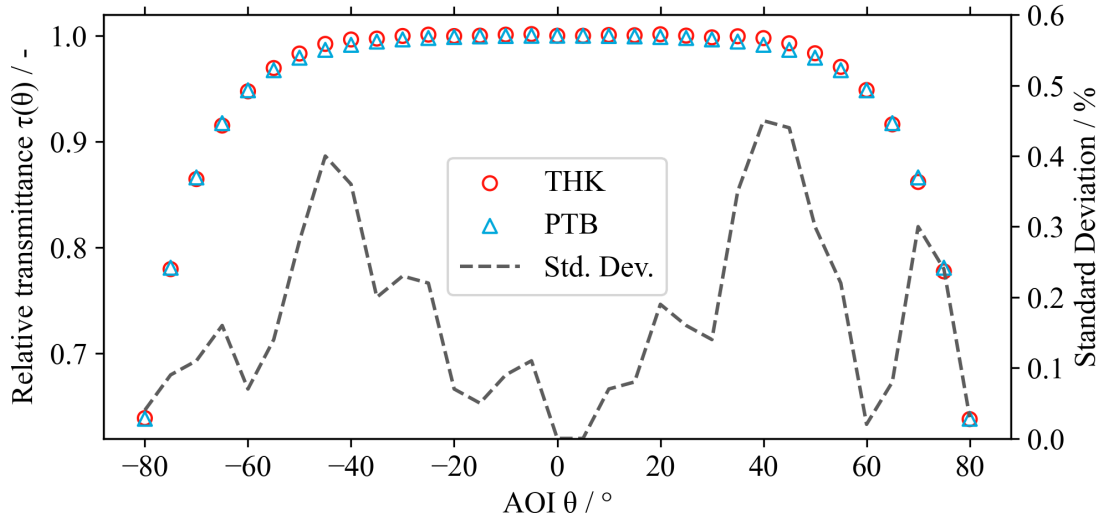
Fig. 3.2 Interlaboratory IAM measurement comparison between Cologne University of Applied Sciences (THK) and Physikalisch-Technische Bundesanstalt (PTB) to validate the developed fully-automated rotational sample stage.

3.2 Computational fluid dynamics BIPVT model

A three-dimensional steady-state CFD model is set up to analyze the fluid dynamics and thermal performance of the BIPVT system under investigation in this thesis. Air flow from the inlet through 12 of these modules connected in series and an outlet manifold at the roof ridge is modeled and simulated in ANSYS Fluent as shown in Fig. 3.3.

The objective is to identify initial optimizations of the BIPVT modules in terms of air flow behavior and thermal performance. Additionally, specific parameters like pressure drop in the air duct system, mass flow trough the air-leakages and convective heat transfer coefficient to the fluid are determined and used as an input in the MATLAB-Simulink and Python simulation model. Therefore, the CFD model is coupled with an energy model to calculate the thermal performance of the BIPVT modules in series. Thus, the pressure drop, temperature contour profile and thermal efficiency can be determined as a function of different geometries, mass flows, irradiance and ambient temperatures. Finally, the results and findings from these simulations are used to supplement the assumptions used to simulate the annual yields of the optimized BIPVT module.

3.2.1 Computational fluid dynamics modeling and boundary conditions

Three geometries are setup with different air-gap sizes s, as shown in Fig. 3.4, to model the air-leakages between each BIPVT module with 0 mm, 1 mm and 2 mm on the top and bottom side. The mesh for the numerical calculation is generated by discretization, which should be as homogeneous and uniform as possible. For the models with a gap of 2 mm, the mesh is generated with an element
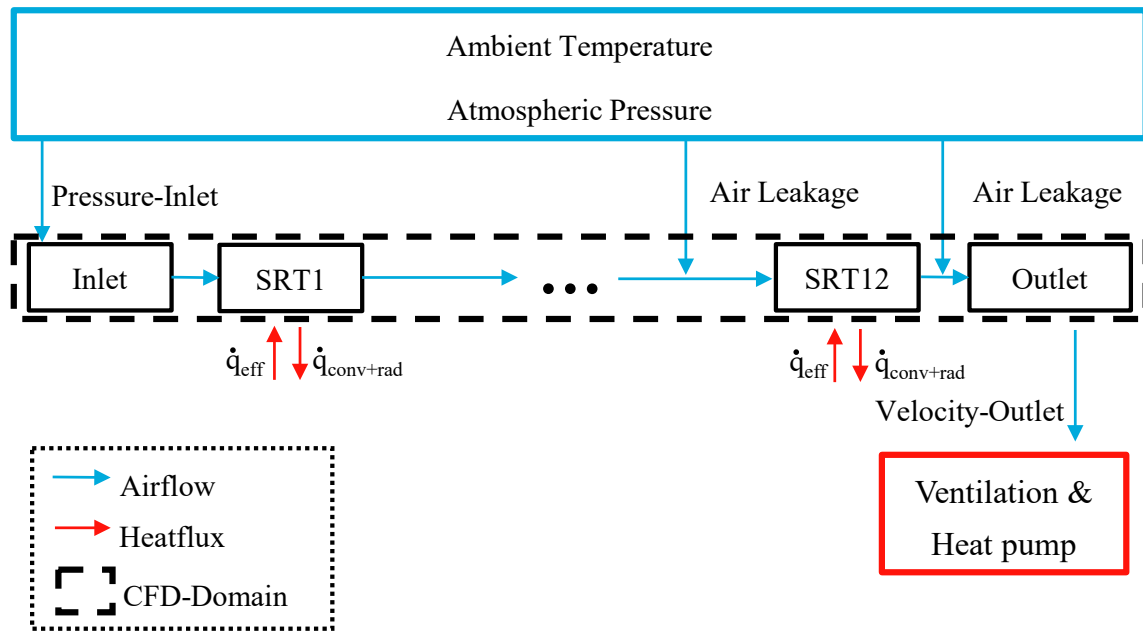
Fig. 3.3 Schematic overview of the CFD model.

size of 2 mm. For the models with a gap of 1 mm, the element size of 1 mm is selected. Furthermore, a constant roof pitch of 45° is setup for all simulations.
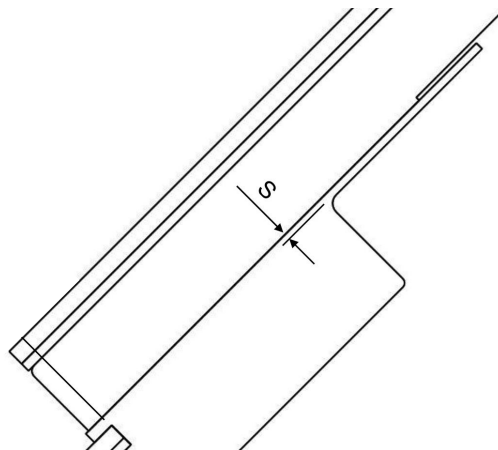
Fig. 3.4 Schematic representation of the modeled air leakage inlet size s in the interconnection between two BIPVT modules.

The boundary layer, a prismatic layer is created near the interfacing surface to the rear ventilation air duct for all models, since this area is important for the heat transfer. In addition, a multizone layer is inserted to structure the mesh as homogeneous as possible.

Getu et al. concluded that CFD simulations are suitable to analyze the air flow characteristics and temperature profiles of air-based BIPVT systems. Moreover, they concluded CFD simulations can be applied to optimize them in terms of convective heat transfer coefficients and air flow velocity [49]. A good agreement between experimental measurements and CFD simulations with the k-ω turbulence model of air-based BIPVT systems was found by D. Roelevelda et al. [50]. Therefore, a pressure-based steady-state CFD simulation is performed with the SST-k-ω turbulence model considering energy balance concept for energy analysis of the presented BIPVT system under various operating conditions.

The fluid is defined as air and incompressible ideal gas, as recommended by Getu et al. at mach numbers $M_a < 0.3$ [49]. This setting changes the air density only with the operating pressure and temperature.
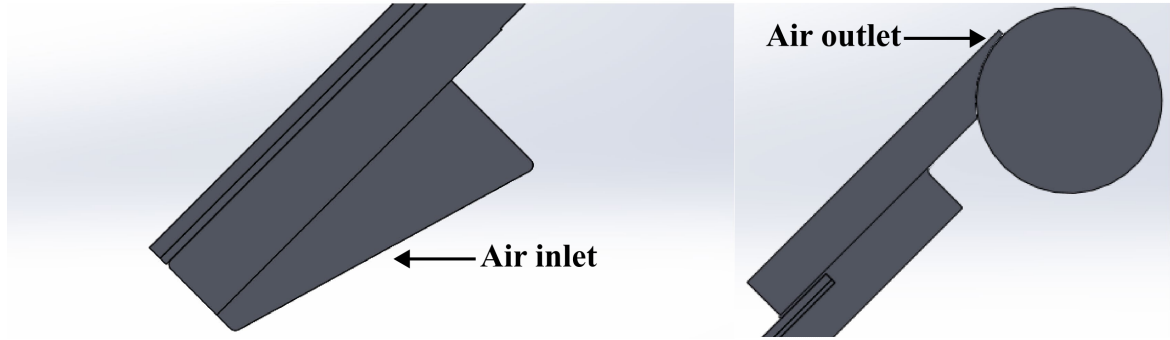
Fig. 3.5 Three-dimensional CAD model of the inlet (left) and outlet (right) of the BIPVT system.

In Fig. 3.5 the simplified geometries of the inlet and outlet of the air duct system are shown in a three-dimensional CAD model.

At the outlet of the manifold, a fan sucks the preheated air out of the air duct system at a constant fluid velocity. The outlet area is defined as a velocity inlet with a negative value. The velocity to be specified is determined by the volume flow generated by the fan and the area at the outlet. The volumetric flow at the outlet of the manifold is defined for various volume flow rates within a parameter study. The inlet surfaces are therefore defined analogously to the leakage inlet surfaces with a pressure inlet. The ambient temperature is assumed as the inlet air temperature into the air duct system.

3.2.2 Thermal modeling and boundary conditions

The thermal model of the BIPVT module is based on a two-node model in which the useful electrical and thermal energy is separated by a thermal transmittance, as described in Section 2.2. Optical losses are calculated analytically for perpendicular incidence and set as constant values in the model. A convective heat transfer coefficient is determined analytically using (2.8) and (2.9) to consider heat losses by convection at the front side of the BIPVT module. Radiation heat losses are calculated with the corresponding sky temperature from (2.10). In order to include the influence of irradiance on

the collector surface, the area between the glass-glass modules is defined as a wall with the thermal material properties (see Table 2.1) of the PV solar cell. The previously mentioned thermal loss mechanisms and the heat transfer from the glass package to the fluid are calculated in ANSYS fluent. A heat generation area is used to represent the heat flux density of the absorbed power after optical losses in the glass package. The volumetric heat flux density $\dot{q}_h$ is used as an explicit input value for the heat generation area d_h and is calculated by (3.1).

$$\dot{q}_v = \frac{\dot{q}_{eff}}{d_h} \tag{3.1}$$

d_h : Thickness of the heat generation area [mm]

The area-specific heat flux density $\dot{q}_{eff}$ is calculated by (2.7) and represents the thermal power density in the glass package as a function of the global irradiance after optical losses.

The boundary conditions for the parameter study are based on the ISO9806-2017 test standard for solar thermal collectors [94], the IEC61853 test standard for PV modules [73, 57], and on the design of the BIPVT module under test.

An exemplary calculation for STC (G=1000 W$\cdot$m^{-2}) results in 617 W$\cdot$m^{-2} at 93% transmittance τ, 90% absorptance α_{abs} of the glass package and 22% electrical efficiency η_{el} of the PV solar cell.

3.2.3 Parametric study

In ANSYS Fluent, different operating points with varied input parameters are to be investigated with the same simulation setup by a parameter study. For each combination of input parameters, a parameter set (PS) is created and simulated. Table 3.1 shows the combinations of parameters for all parameter sets. The parameters to be varied are irradiance, ambient temperature, wind speed, and volumetric flow rate at the outlet. The PS0 is the default parameter set, and for the other PS one of these parameters is varied to study its influence on the airflow characteristics. To develop the MATLAB-Simulink model, the influence of these parameters on the heat transfer coefficients in the air duct and the volumetric flow rate at leakage must be determined. The volume flow rate has the most significant influence on the thermal power output of the BIPVT system. Therefore, the results of six parameter sets with varying volume flow rates between 10 m$^3\cdot$h^{-1} and 100 m$^.$3h^{-1} are interpolated. These interpolated results are used in the MATLAB-Simulink model for the parameterization of the mass flow in the air leakages, pressure drop and convective heat transfer coefficient.

3.2.4 Results and discussion

In order to analyze the performance of the BIPVT module in relation to the operating conditions, the heat quantity as well as the thermal efficiency are calculated with the CFD results for each set of

Table 3.1 CFD simulation parameter sets with varying operating conditions.

Parameter set (PS)	G_i $W \cdot m^{-2}$	T_a °C	v_w $m \cdot s^{-1}$	$\dot{V}$ $m^3 \cdot h^{-1}$
0	1000	25	1	100
1	1000	40	1	100
2	800	25	1	100
3	1000	25	3	100
4	1000	25	1	50
5	1000	25	1	75
6	1000	25	1	30
7	1000	25	1	20
8	1000	25	1	10

parameters. Table 3.2 shows selected results calculated with (2.16) and (2.18).

Table 3.2 Heatflux and thermal efficiency CFD simulation results for the analyzed BIPVT module under different operating conditions.

Parameter set (PS)	P_{th} W	η_{th} %
0	260.69	23.30
1	258.95	23.14
2	213.59	23.86
3	212.98	19.03
4	184.33	16.47

Fig. 3.6 shows the results of the CFD simulation in a temperature contour plot of the center cross-section of a BIPVT module air duct connected in series. The simulation is performed with PS8 (Table 3.1). Accordingly, the operating conditions are set at $1000 \, W \cdot m^{-2}$ global irradiance on the module surface, 25°C inlet air temperature, $1 \, m \cdot s^{-1}$ wind speed and $10 \, m^3 \cdot h^{-1}$ volume flow rate. The air leakage inlets are defined by 1 mm on the front and rear sides. The simulation results are based on assumptions and simplifications. Therefore, a comparison with experimental measurement values of the results is recommended. Nevertheless, the CFD simulations performed can help identify initial optimization potential in terms of the thermo hydraulic performance of the BIPVT module.
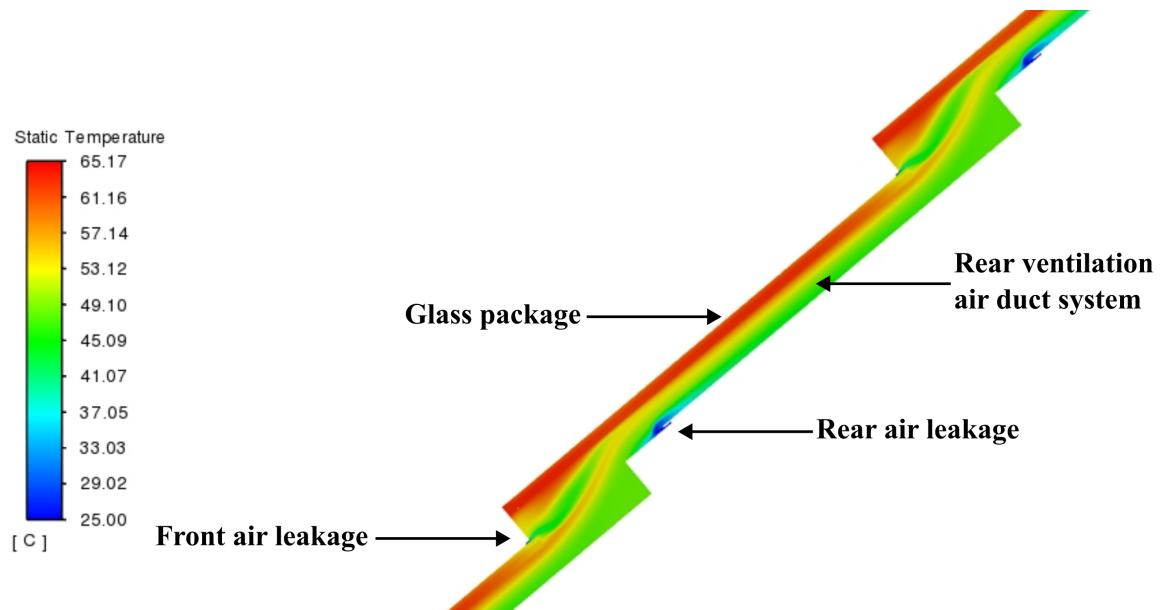
Fig. 3.6 Simulation results of the parametric study. Temperature contour plot of the center cross-section of the BIPVT rear ventilation system CFD model.

3.3   Time-series based BIPVT simulation framework

A time-series based BIPVT simulation framework is setup to analyze and assess the proposed optimizations of the module. Fig. 3.7 shows an overview of the model.
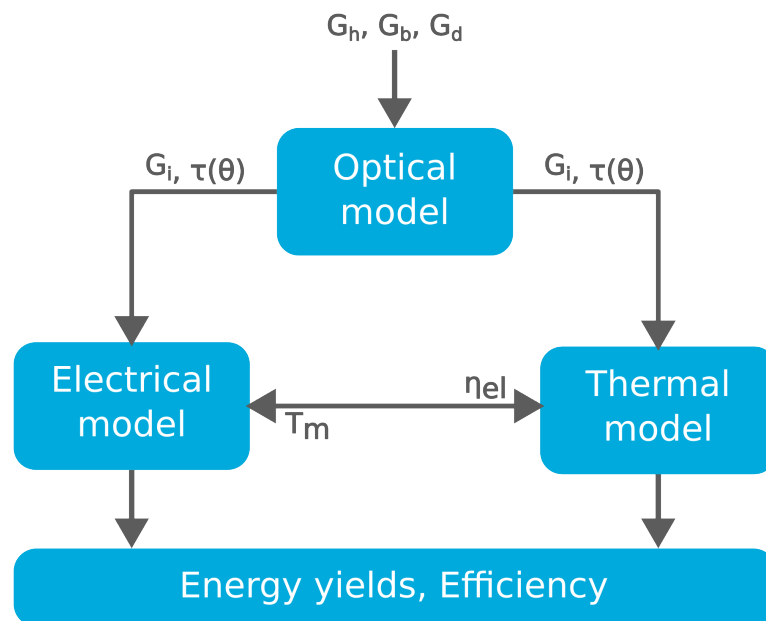
Fig. 3.7 Schematic overview of the developed BIPVT simulation model.

The irradiance model first converts time series data of direct G_b and diffuse G_d irradiance components to the in-plane irradiance G_i for the particular tilt angle and orientation of the simulated system. This is done using direct and diffuse irradiance transposition models. In addition, the $\tau(\theta)$ of different front glass covers is simulated to analyze the gains and losses in energy output of BIPVT modules with textured or colored glass compared to standard solar glass. The $\tau(\theta)$ of the BIPVT module is derived from data measured in the laboratory. These parameters are used for calculations in the electrical and thermal models. Next, the electrical efficiency η_{el} is approximated based on the module temperature $T_{m,f}$ derived by the empirical model in (2.20). Subsequently, the η_{el} is used in the thermal model to calculate the thermal power output. Then, η_{el} is re-calculated with the module temperature T_m derived by the thermal model. Finally, the electrical and thermal efficiencies for the BIPVT system are calculated.

3.3.1 Optical model

The optical model calculates the effective irradiance on the tilted surface of a BIPVT system by (2.6). This optical model combines irradiance transposition, correction of angular-dependent losses on the front glass and spectral corrections. In the following, the assumptions and modeling approach for the calculation of the effective irradiance are described.

3.3.1.1 Diffuse irradiance transposition model

Various diffuse irradiance transposition models with strengths and weaknesses have been developed in [95–99]. The most frequently used and accurate of these models are the Perez in [97] and the Hay/Davis in [98] as described in [100]. Table 3.3 shows a statistical error analysis based on POA global irradiance G_i values calculated with selected models. The observed values are measured at the THK test site with a class A pyranometer (CMP11) on the test roof with a tilt angle of 40°, as described in Section 5.1.1. The irradiance components used as input parameters for the transposition models are measured with a dual-axis sun tracker. The same measurement data set is used as for model validation in Section 3.3.4.

Table 3.3 Statistical error analysis of selected diffuse irradiance transposition models.

Transposition model	MBE		RMSE	
	$W \cdot m^{-2}$	%	$W \cdot m^{-2}$	%
Isotropic [95]	-26.2	-8.5	46.3	15.0
Perez [97]	-1.5	-0.48	21.3	6.9
Hay and Davies [98]	-8.6	-2.7	28.2	9.1
Klucher [96]	-9.3	-3.0	24.3	7.9

The data set is used in 15-minute averages of 20-second samples. This data set has been recorded over a continuous period of 59 days in the winter and, accordingly, includes all sky conditions. The relative

MBE of calculations with the Perez model shows the lowest values with $-0.48\%_{\text{rel}}$. Calculation with the Hay/Davis model shows larger errors with $-2.7\%_{\text{rel}}$. In comparison, the authors in [100] observed values between $1.4 - 1.7\%_{\text{rel}}$. Although the error margins are slightly increased for the Perez model, the observations in [100] confirm the results in this thesis. The authors also found that the Perez model provided the most accurate predictions when DHI measurements are available. Since DHI data is available in the TMY data sets used for the simulation study in this thesis, the diffuse irradiance in the POA of the BIPVT modules is transposed by the Perez model in [97].

3.3.1.2 Angular-dependent losses

The optical model also describes the angular-dependent reflection losses on the front side of the BIPVT modules. The relative transmittance $\tau(\theta)$ of the samples is measured to consider these optical losses and derive angular loss parameters. The optical losses can be reduced by textured front glass. Therefore, the BIPVT module is optimized by means of a textured glass cover. The analyzed test samples are manufactured with the same textured glass cover but do not have ceramic ink-jet printing on the inner side. Moreover, the test samples are equipped with a single PV cell of the same cell type. Fig. 3.8 shows the measured $\tau(\theta)$ of a flat standard (Control) and textured solar glass.

The measurements are done according to the IEC61853-2 standard in [57] by (2.2). A suited modeling approach to account for angular losses for direct and diffuse irradiance components for textured glass is required. Therefore, different $\tau(\theta)$ models are fitted to the measurement values. Fig. 3.8 shows the Martín and Ruiz model for the flat standard solar glass. Moreover, it shows interpolated values
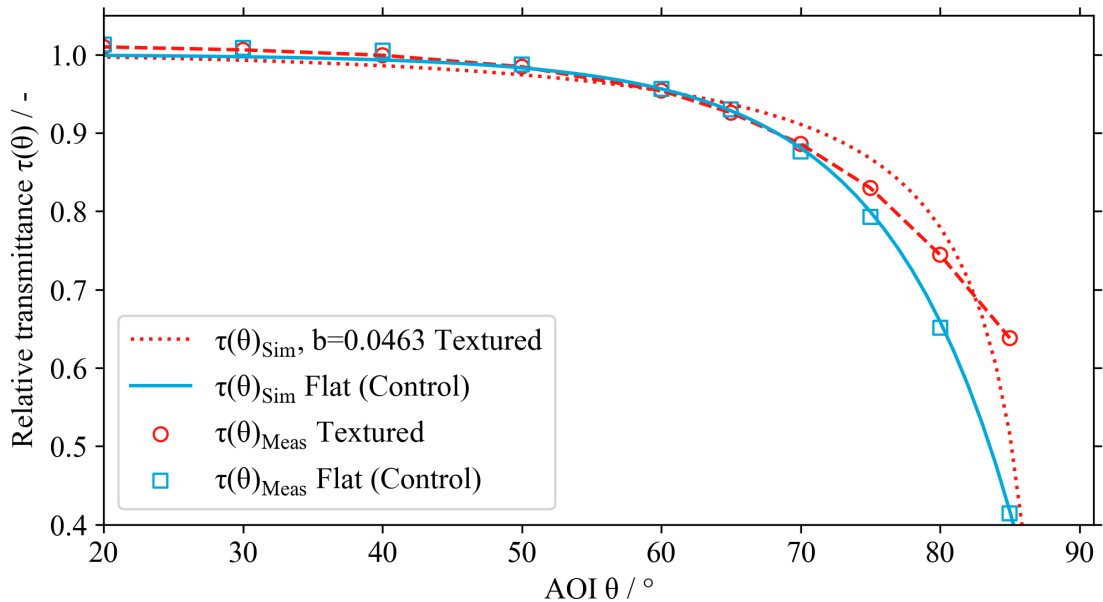
Fig. 3.8 Relative transmittance measurements of standard and light-textured solar glass.

and a fitting with the ASHREA model for the textured glass. The Martín and Ruiz model shows good agreement with the measurement values for standard glass. In contrast, the models described in Section 2.1.1 show a poor fit for the textured glass. This can be explained by the fact that these models only apply for flat glass surfaces. Therefore, the angular losses are considered by using linearly interpolated measurement values of a test sample with the same texture on the front side. Finally, the effective irradiance on the active surface of the BIPVT module on a tilted plane using angular-loss parameters is calculated by (2.6).

3.3.2 Electrical PV model

King et al. presented a model to predict the energy yields of PV modules at MPP by analytical equations based on empirical derived coefficients determined by measurements at different operating conditions, not provided by the manufacturers data sheet [62, 63]. In contrast, the five-parameter model described by De Soto et al. (Section 2.3.1) requires only one measurement of the IV-curve at STC [75]. Therefore, the single diode equivalent circuit equation, based on five parameters determined according to De Soto et al., is used to predict the electrical energy yields of the analyzed PVT roof tile under varying operating conditions. The PV model was implemented in [101]. Furthermore, the five-parameter model for predicting the electric energy yields of PV modules is recommended by the IEC standard 61853, as well as for the used T_m and effective irradiance model [73].
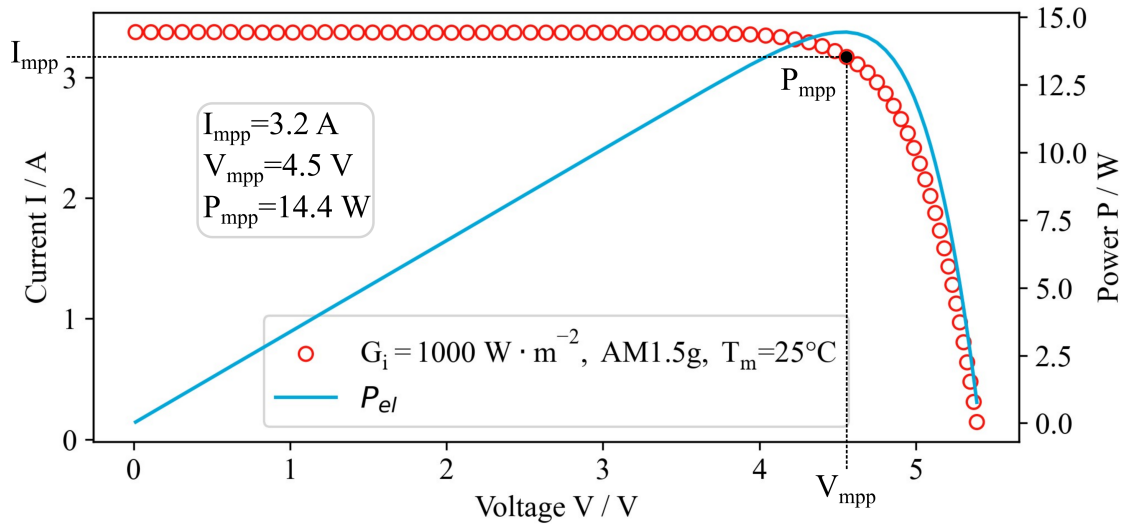
Fig. 3.9 Measured IV-curve of the analyzed BIPVT under STC ($1000 \; W \cdot m^{-2}$, 25°C, AM1.5G) according to IEC standard 61853.

Due to the requirement for the model to be easily modified for simulating BIPVT systems with optimized system components, this modeling approach appears to represent a suitable choice. This is justified with the determination of the five parameters exclusively relying on module data delivered by

the manufacturer or on measurements under STC as input parameters. While the models accuracy for forecasting the MPP is proven to be in a similar range as those from the model described by King et al., the five-parameter model is capable of estimating the complete I-V curve of the module instead of only key points. This allows estimating the systems power output under part load operation and relatively large DC/AC ratios, assumed to be of importance for the investigated BIPVT system being simulated under varying operating conditions [62, 63, 75].

Fig. 3.9 shows the IV-curve measurements of the BIPVT module under study. The measurements are done under STC in accordance with the IEC61853-1 standard on the solar simulator at the accredited test facility of TÜV Rheinland. To obtain the corresponding coefficients for determining the five parameters according to the De Soto et al. model, the California Energy Commission model and estimation method is used to fit the measurement data [102]. Subsequently, the fitted data can be used to determine the five parameters required for solving the single diode equivalent circuit equation in (2.19).
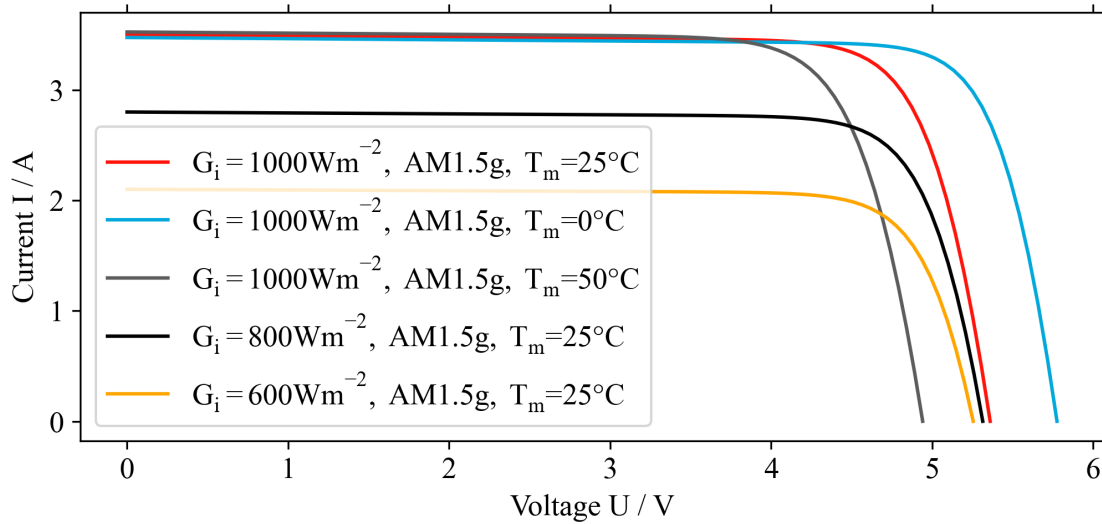
Fig. 3.10 Simulated IV-curve of the BIPVT module under investigation with De Soto single diode model parameterized with IV-curve measurements at STC.

The predicted IV-curves of the PV cells in the analyzed BIPVT module under different operating conditions are shown in Fig. 3.10. These curves are obtained by solving the single diode equivalent circuit equation with different input parameters. The required parameters are determined by De Soto et al. five-parameter model based on measurements at STC. Furthermore, the model can be used to predict the electrical power output of a PV system by summing the voltages of in series connected solar cells. The current is typically limited by the cell with the lowest photocurrent.

3.3.2.1   Parameterization of the PV module temperature model

The empirical PV module temperature model is described in Section 2.3.2. The model is parameterized with measurement data from the experimental setup described in Section 5.1.1. It is applied to assume the PV module backside temperature under real operating conditions. This temperature is used to calculate the electrical efficiency η_{el}. η_{el} is used to quantify the heat flux, which is required as an input parameter for the thermal model. The objective of the parameterization is to identify the constant coefficients $U'0$ and $U'1$ that approximate the heat loss of the modules in dependence on their optical efficiency as well as wind conditions for the BIPVT system.

The coefficients can deviate for different module types [77] and therefore, a careful determination of these modeling parameters is mandatory to ensure the quality of the approximations. These coefficients were determined in [101] in accordance to [77] for the BIPVT system at the THK test site using a least-squares fitting approach. The fitting is based on field measurement data from 18 days in June 2022. The data includes the PV module backside temperature T_m of four sensors attached with thermal conductive paste as well as measurements of the corresponding weather and irradiance conditions. The positions (D4, D8, G4, G8, see Fig. A.1) of the module temperature sensors are in the center of the test roof to consider the maximum cell temperatures in the measured PV array. In comparison, the heat loss coefficients are also calculated by averaged values of 32 uniformly distributed module temperature sensors. This is done to evaluate the influence of edges of the test roof in the empirical temperature model. It is also important to highlight that the active rear ventilation has been operated constantly with $\dot{V}$=350 $m^3 \cdot h^{-1}$ during the measurement period.

Fig. 3.11 shows the results of the model parameter fitting. The heat loss coefficients are correlated
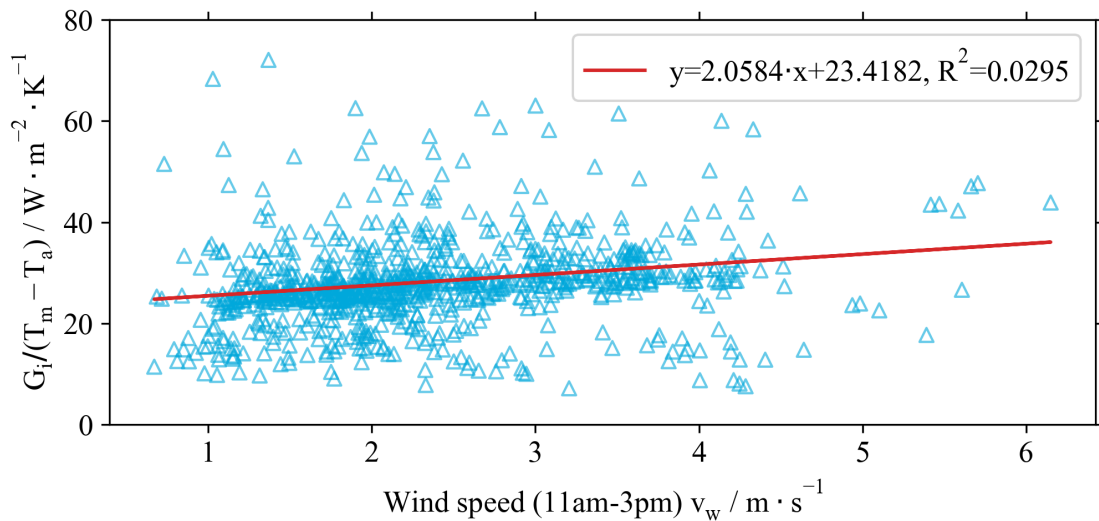
Fig. 3.11 Measurement data of $G_i/(T_m - T_a)$ as a function of the daily wind speed recorded of 18 days between 11:00 am and 3:00 pm in 5 min intervals, including the least squares linear fit of the data set.

to the slope and intercept of the regression line, with 23.4182 $\mathrm{W \cdot m^{-2} \cdot K^{-1}}$ for $U'0$ and 2.0584 $\mathrm{W \cdot m^{-3} \cdot s \cdot K^{-1}}$ for $U'1$. Moreover, the heat loss coefficients of the parameter fitting with 32 sensors shows only slightly decreased values for $U'0$ with -0.2%$_{\mathrm{rel}}$ and increased values for $U'1$ with 5.1%$_{\mathrm{rel}}$ in comparison to the previous study in [101] with four sensors. However, the least-square shows a poor fit to the data. One reason for the poor fitting results can be that the model in [77] applies only for PV modules mounted in an open rack. The results show that the BIPVT module temperature is less influenced by the wind speed. These modules are not rear ventilated by the wind due to building integration and thus this behavior is to be expected. Accordingly, the wind direction also has a greater influence when calculating the module temperature compared to PV modules mounted on an open rack. The increased heat loss coefficient for wind speed can be attributed to the consideration of more temperature sensors. In particular, the module temperatures at the gable of the test roof are more influenced by the wind and therefore these observations are consistent. In addition, the resulting heat loss coefficients describe the module temperature with active-rear ventilation. This mode of operation is not considered in the module temperature model and therefore the significance of the coefficients is limited. Nevertheless, the parameterized PV module temperature model can be used as a first approximation to predict the electrical efficiency as input parameter for the thermal model. The more accurate module temperature for determining the electrical efficiency under real operating conditions is derived by the dynamic thermal model. Accordingly, the module temperature of the dynamic model is used as input parameter in the electrical model to calculate the final electrical efficiency.

Measurement data of the BIPVT system during periods without operating the ventilation system is considered to model the module temperature while stagnation of the air. This is done to provide realistic module temperature values to the PV model when simulating a solar assisted heat pump system (SAHP) in Section 5.2.1.[2]

3.3.3 Dynamic thermo hydraulic model

This section describes the dynamic model developed to analyze the performance of the optimized BIPVT system. In this thesis, the model is used to predict annual collected thermal energy for different locations, orientation and sizing. In addition, the optimal mass flow rates for specific air duct system designs are identified. A physical model is setup in MATLAB-Simulink, which partially published in [93].

The required input modeling parameters, such as the heat transfer coefficients and air leakage volume flow rates of the rear ventilation system, are identified by CFD flow simulations in ANSYS Fluent, as described in Section 3.2. This modeling approach is able to avoid transient CFD simulations with high computation times and describe the thermo hydraulic system with a physical model of the BIPVT system, taking into account specific design characteristics such as air leakage inlet size.

In addition, the model can be used to perform a numerical study to analyze the BIPVT module

---

[2]Fragments of the following section are published in "Dynamic Simulation Model of an Air-Based BIPVT Roof Tile System" (Clasing et al., Proc. 8th World Conference on Photovoltaic Energy Conversion, Milan, Italy, 2022, pp. 662–665) in [93].
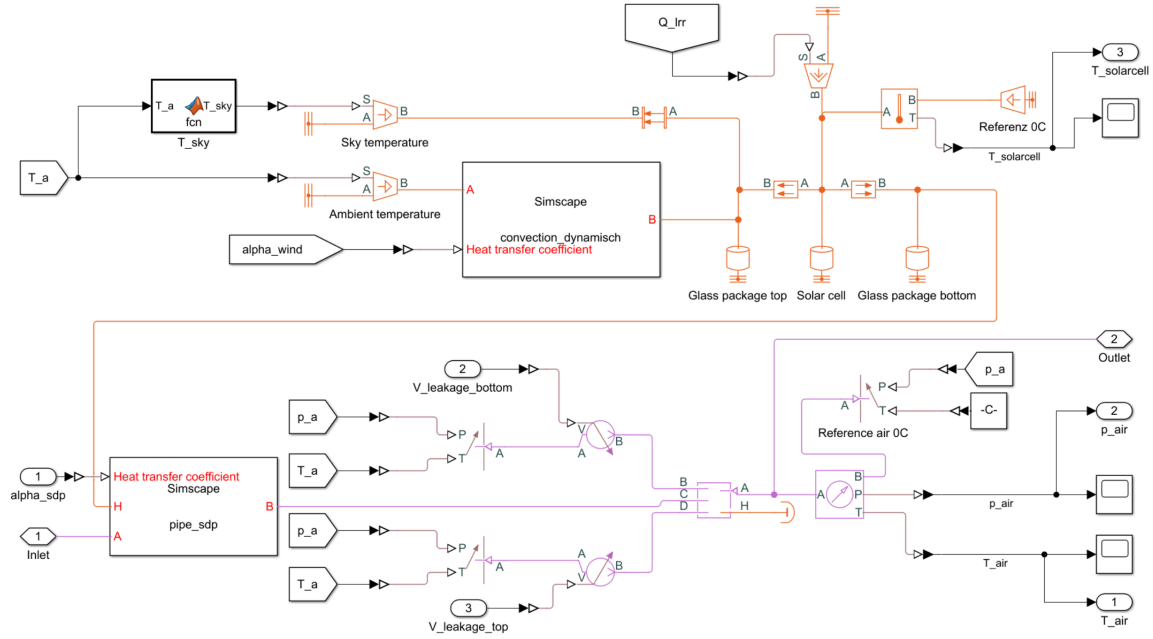
Fig. 3.12 Depiction of the simulation model of a BIPVT module as a subsystem in MATLAB-Simulink.

performance as a function of mass flow rate. Accordingly, the optimal mass flow rate for different air duct designs can be identified in terms of air leakage. Hence, the collected thermal energy for a specific collector design can be increased.

The thermo hydraulic model of the BIPVT system consists of a coupled gas and heat network modeled with physical components from the Simscape library. Fig. 3.12 shows the simulation model of a BIPVT module with a gas network (purple) and a thermal network (orange) in one subsystem. Throughout the gas network, the inlet, 12 of these subsystems, and the outlet are connected in series.

3.3.3.1   Gas network

Fig. 3.13 shows the structure of the gas network of a BIPVT module subsystem. The rear ventilation system is modeled as a pipe, which calculates the convective heat transfer between the airflow and the PV glass-glass module as well as the pressure loss. A constant volume chamber represents an air gap, where ambient air flows in through the leakages and mixes with the air in the ventilation system. According to [103], the pressure difference between the inlet and outlet of a pipe is calculated as

$$p_1 - p_2 = \rho_2 \, \dot{V}_2^2 \, - \, \rho_I \, \dot{V}_1^2 \, + \, \Delta p_f, \tag{3.2}$$
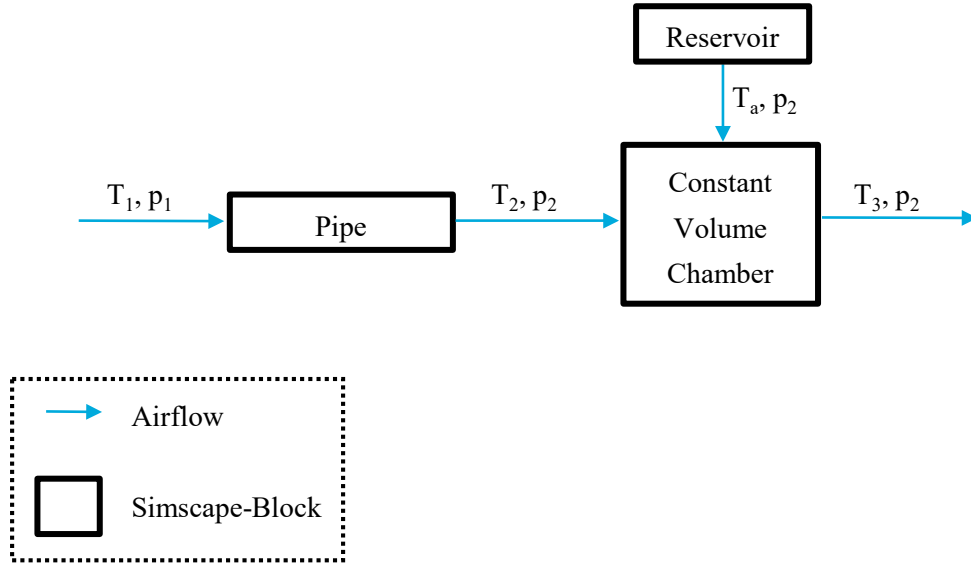
Fig. 3.13 Schematic diagram of the BIPVT gas network subsystem setup in MATLAB-Simulink.

where ρ is the air density, $\dot{V}$ is the volume flow rate, and Δp_f is the pressure drop due to friction on the pipe wall. The pressure drop is calculated as

$$\Delta p_f = f_D \frac{\dot{m}^2 \, L}{2 \rho_I \, D_h \, A_p^2}, \tag{3.3}$$

where f_D is the Darcy friction factor, $\dot{m}$ is the mass flow rate, L is the length of the pipe, ρ_I is the internal air density in the pipe, D_h is the hydraulic diameter, and A_p is the cross-sectional area of the pipe [104]. The hydraulic diameter is calculated as

$$\Delta D_h = \frac{4 \, A_p}{P}, \tag{3.4}$$

where P is the wetted perimeter [104]. The Darcy friction factor is calculated for laminar flow as

$$\Delta f_{D,lam} = \frac{64}{Re} \tag{3.5}$$

and for turbulent flow as

$$\Delta f_D, t = \left[-1.8 \log \left(\frac{6.9}{Re} + \frac{\varepsilon_r}{3.7 \, D_h}^{1.11} \right) \right]^{-2}, \tag{3.6}$$

where Re is the Reynolds number and ε_r is the absolute roughness of the inner pipe wall [104]. The Reynolds number is calculated according to

$$Re = \frac{\rho_I \, \dot{V} \, D_h}{\mu} = \frac{\dot{m} \, D_h}{A \, \mu} \tag{3.7}$$

However, (3.6) is only valid for fully developed flows with large mass flows, and therefore increased errors are to be expected for small volume flows. The lower Reynolds number limit for the scope must be specified as a parameter in the simulation.

Although the flow in the back-ventilation channel is not expected to be laminar due to the non-uniform geometry, the pressure drop is small and can be estimated with (3.5). The absolute error is expected to be small and therefore negligible. The upper Reynolds number limit must be defined to consider only small mass flow when using (3.5). In the case where the Reynolds number is between the limits of both values, the pressure drop is approximated by interpolation. The input values for (3.2) - (3.7) are obtained from the results of the CFD simulations in Section 3.2. Finally, the absolute roughness for single BIPVT can be calculated and used in the simulation.

A reservoir at ambient temperature and atmospheric pressure is coupled to the inlet of the first module subsystem. A mass flow source is connected to the outlet of the last module to describe the fan. Assuming that the mass flow is evenly distributed in all parallel module rows.

The volume flow rate at the air leakage is determined by interpolating the data from CFD simulations. A constant volume chamber with constant air pressure at all inlets and outlets is used to mix the airflow from the pipe. The mixed airflow flows into the next BIPVT module or to the outlet at the estimated temperature.

Fig. 3.14 shows an overview of the arrangement of subsystems describing the modules connected in series. In the simulation model, 12 subsystems are connected in series to describe the experimental test system. In addition, a subsystem is setup for the aluminum sheet in the ridge construction. This subsystem is modeled as a pipe with the material properties of aluminum.

3.3.3.2   Thermal network

Fig. 3.15 shows the structure of the thermal network. The PV glass module is modeled in three parts: the solar glass on top of the solar cells (Thermal mass 1), the solar cells (Thermal mass 2) and the glass under the cells (Thermal mass 3). First, irradiance input data is used to calculate the effective heat flux $\dot{q}_{eff}$ according to (2.7). Second, the PV cells are defined as a heat flow rate source with $\dot{q}_{eff}$ to describe the thermal conduction to the front and rear glass of the module. Convective and radiative heat loss from the front glass is modeled in relation to the ambient temperature (Temperature Source 1) and the clear sky temperature (Temperature Source 2). The rear glass is directly connected to the thermal connection of the pipe, so it is defined as a pipe wall in the model. Thus, the heat transfer to the airflow in the pipe can be calculated. The required design parameters for the model are determined by a steady-state CFD numerical study, as described in Section 3.2. These are the heat
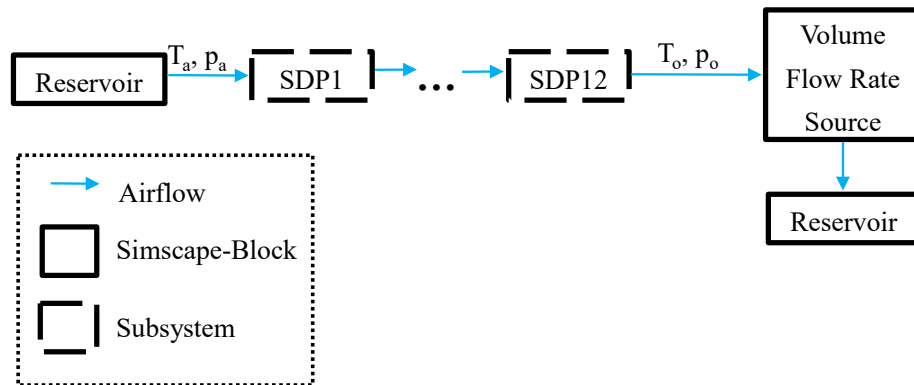
Fig. 3.14 Schematic representation of the gas network of 12 BIPVT module subsystems connected in series in MATLAB-Simulink.

transfer coefficients, the airflow rate in the leakages and the pressure loss.

A parametric study was conducted with the CFD model. The results show that these parameters vary
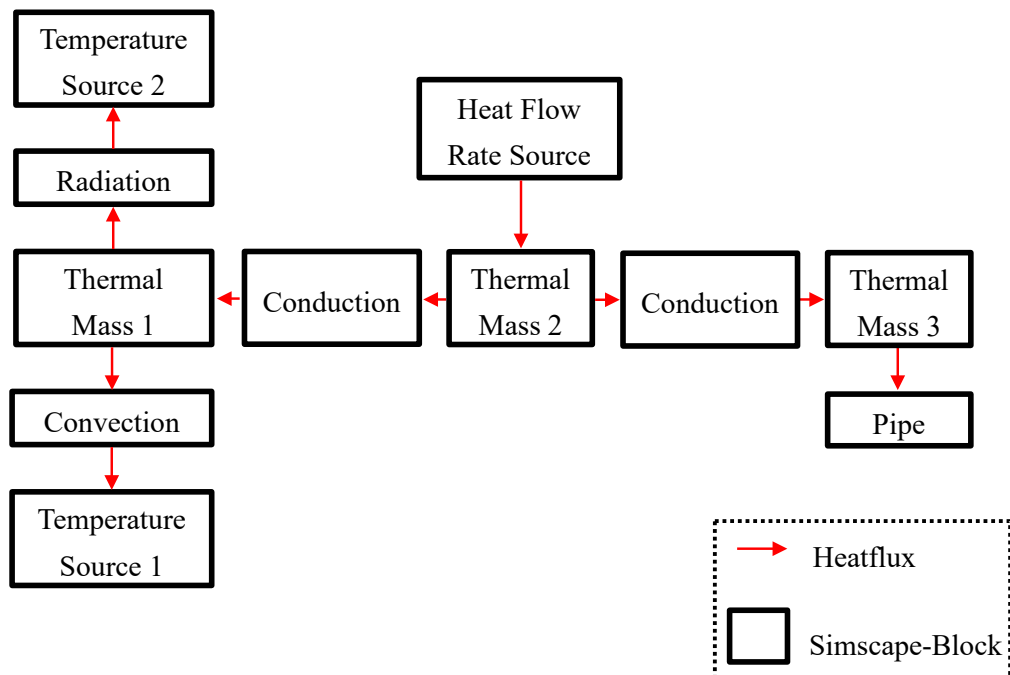
Fig. 3.15 Schematic diagram of the BIPVT modules thermal network subsystem setup in MATLAB-Simulink.

with the airflow rate in the rear ventilation air duct. Thus, the output data from CFD simulations with varying flow rate are interpolated and the resulted functions are implemented into the model.

3.3.3.3   Parameterization of convective heat transfer coefficients

For the calculation of heat transfer coefficients for convective heat transfer in the rear ventilation of individual BIPVT modules, the heat flux, fluid temperature T_f and surface temperature T_s of the glass package are required. These parameters are typically determined from CFD simulations or

Table 3.4 Average values and calculation approaches for fluid and surface temperature.

Averaged Value	Calculation model
$T_f(M)$	Mass weighted average on the center plane of the air duct
$T_f(V)$	Mass weighted average in total air duct volume
$T_s(A)$	Area weighted average on the bottom of the glass package
$T_s(V)$	Volume weighted average in float glass EVA component

experimental measurements [105]. The results of CFD simulations used in this work are shown in Section 3.2. Since the temperature distribution in the glass-glass module and in the fluid volume is not homogeneous, average values are used for the calculation, which can be determined by different approaches. Thus, two average values are determined for each of the two temperatures (see Table 3.4). With combinations of these values, the heat transfer coefficients for PS0 (see Section 3.2) are calculated and used in the simulation model. The accuracy of different models is analyzed by performing steady-state simulations with constant boundary conditions in MATLAB-Simulink and comparing the calculated temperatures at transitions between BIPVT modules as well as at the outlet with CFD results. RMSE are calculated for each model approach and presented in Table 3.5 and Fig. 3.16. Calculation model 4 with the lowest RMSE is used for the calculation of heat transfer coefficients of the analyzed BIPVT module.

Since the volume flow rates at leakages and the heat transfer coefficients depend mainly on the volume flow rate at the outlet, both parameters can be interpolated with 1D functions. The MATLAB function pchip (Piecewise Cubic Hermite Interpolating Polynomial) is used, which avoids overshoot and can interpolate smooth functions. When simulating in MATLAB-Simulink, the parameters are updated dynamically for each time step after the volume flow.

Table 3.5 Comparison of models with different convective heat transfer coefficients based on fluid and surface temperature calculation models.

Model	Fluid temperature	Surface temperature	RMSE / °C
1	$T_f(M)$	$T_s(V)$	0.53
2	$T_f(M)$	$T_s(A)$	0.38
3	$T_f(V)$	$T_s(V)$	0.27
4	$T_f(V)$	$T_s(A)$	0.22
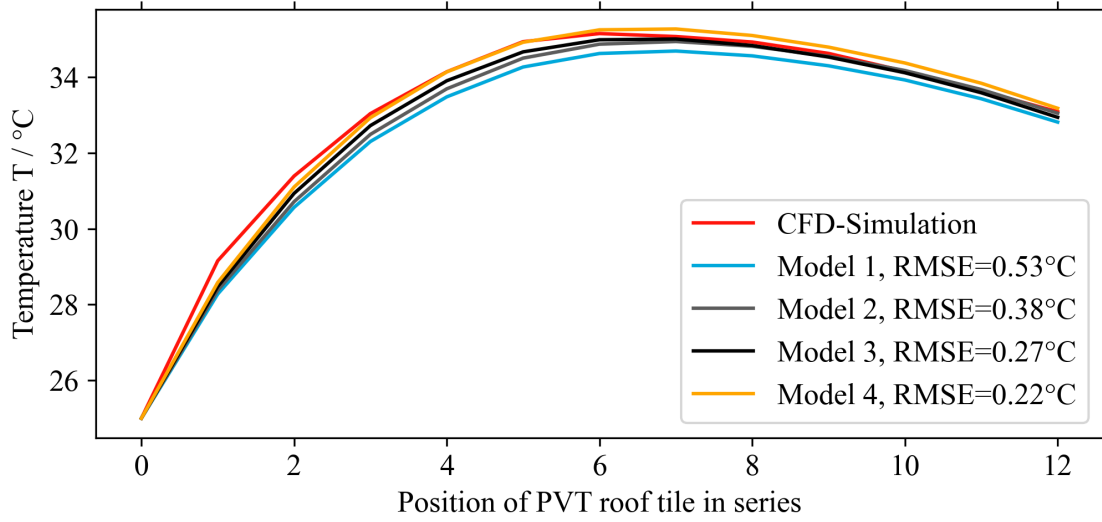
Fig. 3.16 Steady-state simulations of the outlet temperature of 12 BIPVT modules in series using MATLAB-Simulink and CFD, taking into account convective heat transfer coefficients derived by CFD simulations.

3.3.3.4 Fan power model

To optimize the thermo hydraulic performance of the BIPVT system, the mechanical power required to operate the active rear-ventilation system must be considered. Previous studies on solar thermal air heaters in [53–56] report that the output increases with mass flow rate up to a design-dependent maximum and then drops sharply. Therefore, the energy consumption to drive the fan of the system has a non-negligible influence on determining the optimal mass flow rate. The authors in [56] calculate the mechanical power P_{mech} by mass flow rate $\dot{m}$, pressure drop of the air duct system Δp and air density ρ as

$$P_{fan,mech} = \frac{\dot{m} \cdot \Delta p}{\rho}. \tag{3.8}$$

The conversion of electrical to mechanical energy is considered as a constant factor $\eta_{fan} = 0.18$ from [106] to determine the required electrical power input of the fan P_{fan} as follows

$$P_{fan,el} = \frac{P_{fan,mech}}{\eta_{fan}}. \tag{3.9}$$

This assumption implies an optimally sized fan connected to a given air duct system for each mass flow rate, which is realistic in terms of an optimized design approach. However, the authors in [53, 54] suggest this procedure for a harmonized testing method for solar thermal air heaters in order to compare different collector designs.

3.3.4   Field validation of the BIPVT model

Outdoor performance data is compared to simulation results in order to validate and evaluate the real operating conditions prediction accuracy of the BIPVT model. Section 3.3 describes the model in detail. The objective is to validate the electrical as well as the optical and thermal-hydraulic models under real operating conditions. The model predicts the energy yields of the system under study based on weather data such as irradiance, ambient temperature, relative humidity, ambient pressure and wind data. This data is widely available in hourly resolution for various locations in [107].

The experimental setup used for field measurements is described in Section 5.1.1 and includes DC- and AC power output of the PV cells as well the outlet mass flow rate and air temperature of the rear-ventilation system. In addition, solar irradiance, ambient temperature, relative humidity, ambient pressure and in-plane wind speed are measured and used as input parameters for model validation. While the step size of the solver in the simulation is set to be variable, the weather data set is interpolated by 15-minute average values. Thus, the simulation includes the dynamics of environmental conditions at a higher level of detail compared to the hourly weather data in [107]. The time resolution of the input data set used for the validation is higher compared to the data used for the simulation of annual energy yields in Section 5.2. This is done to ensure comparability of the validation with the simulation results. The PV system is grid-connected and operated in MPP mode during the field measurements. Accordingly, the interaction between electrical and thermal power conversion is considered in the measurement data sets. However, the overall system consists of two different PV string configurations. On the one hand, the left string is a conventional system. On the other hand, the right string features MPP tracking on module level. In this work, only the conventional PV string with 96 BIPVT modules with a total surface area of 9.6 m² is simulated and used for validation. In contrast, the collector pipe in the ridge of the test roof is connected to 12 parallel vertical air ducts of the rear ventilation system. Accordingly, the total gross area A_g of the solar thermal system is 15.6 m².

A continuous data set with recorded measurements for a total of 59 days in winter is used for validation. The measurement period has been in winter season from January to February 2023. The dataset contains clear sky, partly clouded as well as overcast sky conditions. It is based on periods with different fan operation modes and thus volume flow rates in the air ducts of the BIPVT system. The fan is operated with a constant volume flow rate within 21 days with 350 $m^3 \cdot h^{-1}$ and 210 $m^3 \cdot h^{-1}$ for 9 days. An ASHP coupled to the air duct system has been operated for 29 days and therefore the data set includes periods with varying flow rates and stagnation times as well. The mass flow input of the model in Section 3.3 considers only a single air duct system. Therefore, the measured mass flow rate in the setup is divided by the number of parallel rows n_r to simulate a single BIPVT air duct system. Consequently, the simulated output mass flow is multiplied by the n_r to calculate the total collected thermal energy of the system. Furthermore, the ridge construction has air leakage which can not be quantified in detail due to the complex design. Therefore, the mass flow rate distribution of the air leakage in the ridge and in the air duct system of the BIPVT module is assumed with a constant

factor applied to the output mass flow rate.

The thermo hydraulic simulation model shows increased errors in terms of low-light conditions. Therefore, the measured $G_{i,meas}$ is limited to values $\geq 50W \cdot m^{-2}$. Likewise, the measurement errors of the irradiance sensors increase due to the low signal amplitudes and the resulting reduced signal-to-noise ratio at these conditions. The resolution is resampled from 20-second to 15-minute average values. For this reason the data sets are filtered and pre-processed according to the following rules:

1. Irradiance conditions: $G_{i,meas} > 50W \cdot m^{-2}$

2. Resolution: 15-minute average (sampling 20 seconds)

To evaluate the prediction accuracy of the model, the simulated energy yield is compared to the measured energy yield using the relative mean bias error in (2.29). The absolute MBE and RMSE values are not as relevant as the relative values for assessing the predicted energy yields, but these error metrics calculated for selected parameters provide insight into potential sources of error in the model. Therefore, the absolute error metrics are determined for the air outlet temperature and module temperature. The module temperature is validated for the two modeling approaches used in this thesis, the empirical PV module temperature model according to the IEC 61853 (Faiman et al. [77]) standard and the numerical model in MATLAB-Simulink.

3.3.4.1   Results and discussion

Fig. 3.17 shows the measured and specific power output of the electrical and thermal system for one day in winter. Likewise, the specific solar irradiance as well as the in-plane wind speed are presented. The DHI/GHI ratio shows $12\%_{abs}$ and indicates clear sky conditions on this day. The BIPVT rear ventilation system has been operated in combination with the ASHP from 8 am until 2.45 pm. In addition, a temperature-difference controlled auxiliary tube fan was operated during the period specified. The simulated electrical power output values show good agreement with the measured values for the corresponding environmental conditions. The simulation of the electrical output shows a slight overestimation in the morning and an underestimation in the evening. The simulated electrical power reaches a maximum value of $127 \text{ W} \cdot m^{-2}$ at 12:00. Likewise, the simulated thermal power output shows an overestimation until 12 am. The simulated thermal output reaches its maximum at 1 pm with $194 \text{ W} \cdot m^{-2}$. The thermal power output follows varying mass flows in the rear ventilation system due to the operation of the ASHP and auxiliary fan. The mass flow rate increases from 230 to about $400 \text{ kg} \cdot h^{-1}$ between 8 and 9 am. Subsequently, the mass flow increases only gradually up to $500 \text{ kg} \cdot h^{-1}$ until 2.30 pm. The air in the rear ventilation stagnates from 2:45 pm on, which can be explained by the operation mode of the ventilation system. This is indicated by the thermal performance, which drops accordingly to around zero. The in-plane wind speed shows maximum values of $2.1 \text{ m} \cdot s^{-1}$ at around 11 am, 4 pm and 5 pm. Although the simulated and measured thermal power are different, the influence of wind speed is visible in both values at about 11 am. A similar behavior can be observed in the afternoon from around 1.45 pm on.
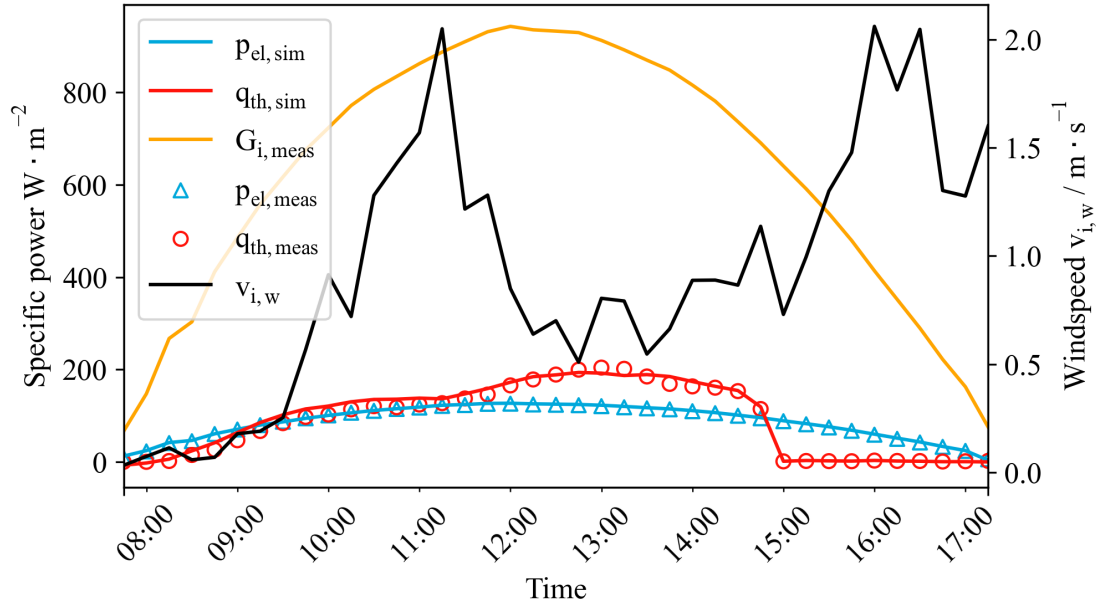
Fig. 3.17 Measured and simulated specific power output of the BIPVT system under real operating conditions. The graph shows a day with clear sky conditions. In-plane wind speed parallel to the collector surface is plotted.

Fig. 3.18 shows the specific power outputs for the simulated and measured BIPVT system on a day with partly cloudy and overcast sky conditions. The DHI/GHI ratio indicates $77\%_{abs}$ for the corresponding sky conditions. The ventilation system has been operated constantly with a mean mass flow rate of $250\,\mathrm{kg\cdot h^{-1}}$ by the auxiliary fan. The heat pump was not in operation and, accordingly, was not coupled to the air duct of the BIPVT rear ventilation system. The simulated power output values show good agreement with the measured values for this day. The simulated values are both slightly over- and under-estimated during the day. The thermal power output is increasingly underestimated in the afternoon, starting at 2.30 pm. The wind speed reaches maximum values of $4\,\mathrm{m\cdot s^{-1}}$ at 11.45 pm. The results of model validation by comparison with field measurements are summarized in Table 3.6. The model shows good agreement in terms of the electrical and thermal yields. The simulated electrical DC energy yield is $18.16\,\mathrm{kWh\cdot m^{-2}}$ whereas the measured yield is $18.02\,\mathrm{kWh\cdot m^{-2}}$. Accordingly, the simulated electrical yield shows a slight overestimation of $0.8\%_{rel}$ compared to measurements. In comparison, the thermal yield is simulated and measured with $11.9\,\mathrm{kWh\cdot m^{-2}}$ and $12.0\,\mathrm{kWh\cdot m^{-2}}$ for the same time period, respectively. The ΔMBE shows an underestimation of $-0.8\%_{rel}$ for the collected thermal energy. Table 3.6 shows also the MBE, RMSE and RE(max) of the selected temperature values in the BIPVT system. The air outlet temperature shows an absolute MBE of 0.5 K and an RMSE of 2.7 K. The relatively large RMSE indicates larger deviations in the simulated values within the data set. However, the comparatively low MBE shows that these deviations are compensated in the predicted energy yield. This can be confirmed by RE(max), which
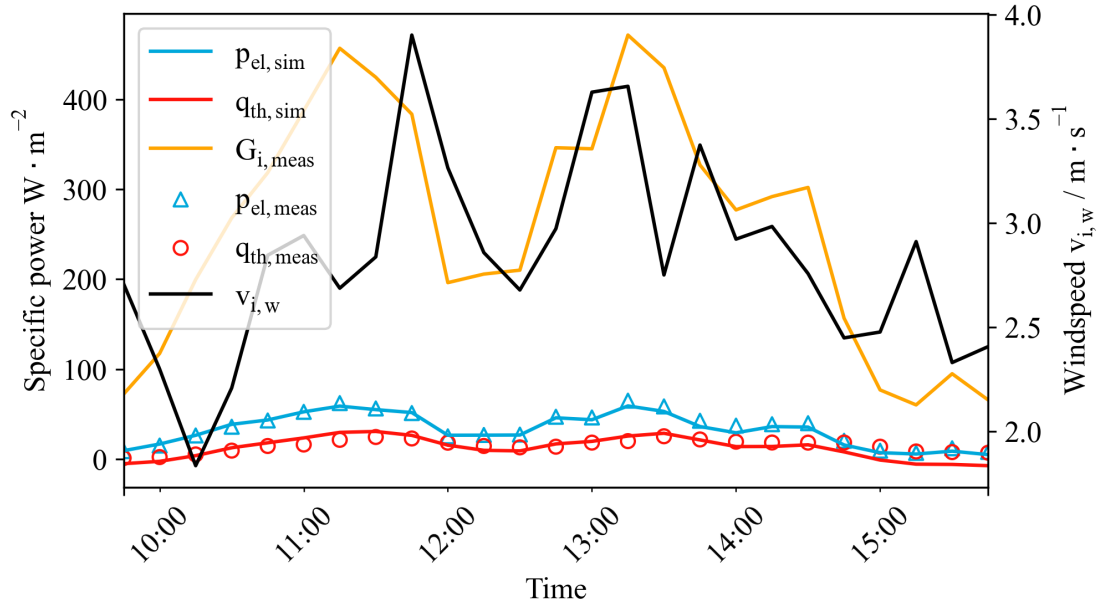
Fig. 3.18 Measured and simulated specific power output of the BIPVT under real operating conditions. The graph shows a day with partly cloudy and overcast sky conditions. In-plane wind speed parallel to the collector surface is plotted.

shows a maximum value of 8.5 K. Likewise, the module temperature has a similar error, although it is larger for the MBE. Finally, the error of the parameterized empirical module temperature calculated by (2.20) is analyzed. Section 3.3.2.1 describes the parameterization of this model with experimental measurement data. It shows that the simulation error of the empirical model is significantly larger for the predicted module temperature $T_{m,f}$ values in comparison to the values of the dynamic model T_m. The difference in RMSE between the two models is 1.9 K. These observations justify the procedure of recalculating the electrical power output with the more accurate module temperature derived by the dynamic model T_m.

Table 3.6 BIPVT model validation results.

Symbol / Unit	Measured	Simulated	MBE / %
Electrical energy yield E_{el} / kWh·m^{-2}	18.02	18.16	-0.82
Collected thermal energy Q_{th} / kWh·m^{-2}	11.97	11.86	0.83
	MBE / K	**RMSE / K**	**RE(max) / K**
Air outlet temperature T_o	0.54	2.65	8.47
Module temperature T_m	0.95	2.32	7.29
Module temperature $T_{m,f}$ [3]	-2.68	4.52	23.8

Overall, the model validation shows good agreement with the experimental measurement values. The

---

[3]Empirical model, Faiman [77]

model can be used to predict the energy yields of the BIPVT under real operating conditions. The validation includes varying operation mass flows and therefore the model can be used to describe the dynamic system behavior in combination with a heat pump. However, the results of the validation are limited due to several assumptions in the model. These assumptions are based on experimental data from measurements on components in the laboratory and system-level measurements on the test roof. Empirical models from the literature are used to estimate the heat losses by convection and radiation on the front side. Moreover, the influence of the air leakage in the ridge construction can not be quantified in the simulation model. A constant mass flow rate factor is used to approximate the fraction of the mass flow rate attributable to ridge air leakage. Nevertheless, the model is suitable for the simulation of electrical energy yield and collected thermal energy based on time series weather data due to the comprehensive and continuous measurement data set. Therefore, this model is used for the simulation study in Section 5.2 of this thesis.[4]

3.4 Experimental analysis and modeling of colored BIPV modules

The aesthetic perception of photovoltaic modules is an important and motivating factor for installation and promotion of BIPV systems [4]. On the one hand, the deployment of these solar systems in building components must be considered with the protection of existing urban environments [109]; on the other hand, the value and character of a building can be even enhanced by different design possibilities [110]. For example, colored glass in BIPV façades and roof installations can be used as a means to meet this objective because they offer a wide variety of custom design options for architectural professionals and building planners [46, 85, 111, 112, 47]. However, to introduce modules with these glasses to the market, it is crucial to give realistic yield predictions to potential investors. The IEA PVPS Task 15 market, research and development report on colored BIPV in [42] reveals that in addition to cost reduction of coloring technologies, the simulation on outdoor performance is gaining importance.

BIPV modules in façades typically have a non-ideal orientation, thus the distribution of oblique angles of incidence on the module surfaces is much higher compared to standard PV systems. Therefore, it is important to have accurate simulation models for the oblique incidence cases. The $\tau(\theta)$ is normally used to account for reflection losses at the glass-air interface. According to the IEC standard 61853-2:2016, the $\tau(\theta)$ is derived from the measured change in I_{SC} with changing AOI [57]. Furthermore, a few PV system simulation tools use additional spectral correction factors for specific cell and module types. Such spectral corrections are generally given as simple correlations with air mass and with dependence of the clearness index[113–115]. These procedures do not typically include spectral measurements and do not consider that the $\tau(\theta)$ varies with spectra [91, 116].

Performance simulation studies of colored BIPV modules under real operating conditions are sparse in literature in comparison to conventional PV systems. Previous work by Saw et al. [117, 118]

---

[4]Fragments of the following section are published in the article "Simulation of Colored BIPV Modules Using Angular-Dependent Spectral Responsivity" (Clasing et al., IEEE Journal of Photovoltaics (Early Access), 2023) in [108].

presented a machine learning algorithm to simulate the I_{SC} of digital-ceramic printed colored BIPV modules with different colors and opacity levels. However, this modeling approach is limited to modules manufactured with digital ceramic printing technology and to laboratory measurements under STC. Due to the influence of angle-dependent losses that vary with spectra, the performance of BIPV modules with colored glasses based on comparatively highly light-transmissive multilayered interference coatings, as described in [46, 85, 47], can only be simulated with limited accuracy. A simulation study by Gonçalves et al. [119] compared a complex multi-physics model and simplified linear power model to predict energy yields of BIPV modules with standard solar glass. The average difference in energy yield on a daily basis compared to field measurements was 6.2% and 8.7%, respectively. However, the authors used broadband irradiance measured in the POA and therefore neglected the influence of the AOI on SR. Angular-dependent spectral reflectance of PV solar cells and angular-dependent spectral transmittance of standard solar glass covers are applied in a case study by Sharma et al. in [120] to quantify the effect of the AOI on conventional spectral mismatch factor method defined by IEC 60904-7 standard [121]. Therefore, the authors used solar spectral irradiance data obtained from "Simple Model of the Atmospheric Radiative Transfer of Sunshine" (SMARTS) [122]. The results show an underestimation of around 3.5% for the conventional method. However, field validation with PV test data and measured spectral irradiance data is not included in this study, which indicates a gap in previous research.

No simulation studies could be identified in the literature that address the performance of BIPV modules colored with a multilayered interference coating on the cover glass under real operating conditions. However, due to the importance of the custom design options of BIPV modules by this highly light-transmissive glass coloring technology, more accurate and customized simulation models are required. Experimental angular-dependent spectral responsivity measurement data is used to simulate the I_{SC} of colored PV single-cell laminates under field conditions. Furthermore, the I_{SC} is simulated with a modeling approach which requires only the normal incident SR and a broadband angular loss parameter (broadband IAM model). This is done to compare the accuracy and assess the suitability of the angular-dependent spectral modeling approach (ASR model). Field validation of angular-dependent spectral simulations of colored BIPV modules is done for the first time. Prior works about angle resolved SR data have focused laboratory measurements [123–125, 92] or theory [126–128]. Our recent work published in [129] shows good agreement in terms of simulating the I_{SC} using angle-dependent spectral responsivity measurement data with 10 days of PV field test data. However, the work included a simplified model approach for a blue and gray colored PV single-cell laminate mounted on a horizontal surface. Here, this work is extended by simulation of the respective I_{SC} of a gray, blue, blue-green, and gold PV single-cell test sample mounted on a south-oriented rack under a tilted angle (β=42°) including model validation and statistical error analysis of 25 days of PV test data.

3.4.1 Experimental details

3.4.1.1 Test samples

Four PV single-cell laminates (200 mm × 200 mm) with gray, blue-green, blue and gold colored 3.2 mm solar glass are used as test samples to simulate the I_{SC} of colored BIPV applications by means of spectral and angle-dependent measurement data. In addition, a test sample with solar glass is measured as a reference (control). These samples are shown in Fig. 3.19 and are equipped with two busbars, black back sheet and EVA encapsulant.

The color of the glass covers is obtained by a thin-film multi-layer deposition on the inner glass surface. The color-imparting layer uses the effect of interference on thin layers, which reflect selected wavelengths more than others. The color to be reflected is adjusted by the thickness of the applied layer. The process typically shows a high dependence of the perceived color on the AOI. In addition, an etching treatment of the outer glass surface provides a diffuse reflection on the front side and thus a uniform color distribution [85, 47]. However, the standard solar glass of the control sample is low-iron cast glass that is not treated and therefore not structured.
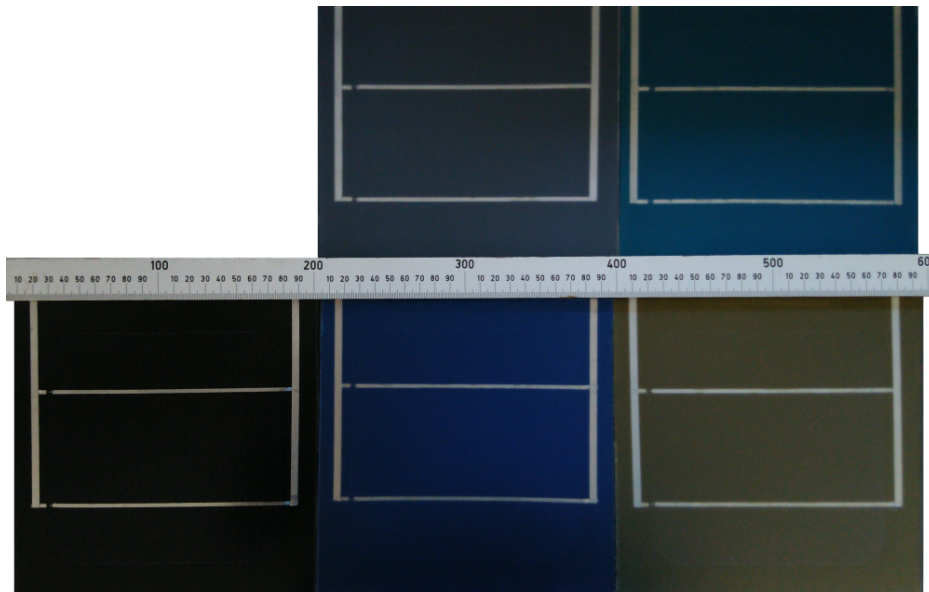
Fig. 3.19 PV cell laminate test samples with four different colored and a transparent (control) glass cover under investigation.

3.4.1.2 Angular-dependent spectral responsivity measurements

The angular-dependent spectral responsivity (ASR) measurements were performed using an experimental setup consisting of a stabilized xenon short-arc solar simulator with optical chopper and lock-in amplifier, two filter wheel monochromators and an automated rotational sample stage. The filter monochromator consists of 40 different filters and thus can provide a wavelength range from

300 to 1120 nm with a FWHM of $\triangle\lambda = 25$ nm. An aperture is used to reduce the light to a small homogeneous area projected completely onto the solar cell even at high irradiation angles. As a result, the measurement signal can be very low at certain wavelengths, and therefore a high-precision voltage measuring device is used. In order to achieve an operating point close to the STC, which are defined as 1000 W·m^{-2}, 25 °C, AM1.5g, additional bias illumination is used. To measure absolute spectral response SR(λ), a reference cell calibrated against a primary reference is used according to the IEC 60904-8 standard [79].

Finally, the angular-dependent spectral responsivity SR(λ, θ) is measured according to IEC 61853-2 between 0° and 90° AOI. While the AOI interval for AOI $\leq$ 60° is 10°, an interval of 5° is used for all other AOI up to 90°. A data pre-conditioning and -processing is done to ensure that a sufficiently accurate resolution of the AOI and wavelengths can be used as input for the outdoor performance simulations and that the measurement effort is not too high. Therefore, the measurement data are first linearly interpolated to 1° AOI and 1 nm spectral resolution and then verified with individual measurements of interpolated SR(λ, θ) for interim values of AOI. It is observed that no significant deviations occur when interpolating the SR(λ, θ) for AOI in between the measurement intervals.

3.4.1.3 Relative transmittance measurements

The $\tau(\theta)$ is used to account for the angular reflection losses at the optical boundary layers of PV modules. The test samples used for modeling the I$_{SC}$ in this work are measured in the laboratory using the experimental setup described in Section 3.4.1.2 and [39]. To ensure a homogeneous irradiance distribution, the samples are measured with broadband spot illumination by means of an aperture. A bias illumination is used to approximate field conditions during the measurements. Therefore, an optical chopper is connected to a lock-in amplifier to compensate bias illumination and improve signal-to-noise ratio of the measurement signal. The measurement series are done according to the IEC 61853-2 standard [57] between an AOI range of -90° and +90°. Finally, the $\tau(\theta)$ is calculated by the ratio of short-circuit current measurements at a specific AOI I$_{SC}(\theta)$ and at the normal AOI I$_{SC}(0°)$ by (2.2). However, this concept neglects the changing wavelength distribution of the sunlight under real operating conditions, and thus it corrects angle-dependent losses only in terms of broadband irradiance, depending on the light source used in the laboratory.

3.4.1.4 Solar resource and field measurement data

The solar resource data-set used to simulate the I$_{SC}$ of the fabricated PV single-cell laminate test samples has been recorded at the Technical University of Denmark (DTU) Risø campus, Denmark (55.7° N, 12.1° E). The data include broadband global horizontal irradiance G_h and diffuse horizontal irradiance G_d measured with two class A pyranometers in 10-second intervals. Direct normal irradiance G$_b$ is measured with a class A pyrheliometer in 10-second intervals. Additionally, spectrally resolved G$_d(\lambda)$ and G$_b(\lambda)$ are measured by two diffraction grating spectroradiometers. These spectrometers measure light between 300 nm and 1100 nm with a FWHM spectral resolution of 7 nm in 1 nm steps.

The spectral measurement data is recorded in 5-minute intervals [130]. Likewise, spectral albedo data is recorded for the test site using a handheld spectroradiometer specified for a wavelength up to 900 nm. This spectroradiometer provides an FWHM spectral resolution of less than 3 nm and a wavelength accuracy of less than ±0.5 nm.

The specified wavelength range of the used spectrometers is limited to 1100 nm. In contrast, the relevant wavelength of crystalline silicon solar cells ranges from 300 to 1200 nm. Therefore, the solar resource data set is extended in the wavelength range of 1100 nm up to 1200 nm by means of the SMARTS presented by Gueymard [122]. For each timestamp, the SMARTS is used to simulate clear-sky spectral $G_b(\lambda)$ and $G_d(\lambda)$. Hence, measured weather data and calculated sun position are transferred to the model as input parameters. Furthermore, a cloud scaling factor according to Ernst et al. [131] is applied to the extended clear sky data to take the clouds into account. Furthermore, the spectral albedo data is extended with data of the SMARTS database. More specifically, the ground material gravel is chosen, which shows the best agreement to the measured spectral albedo data.

Fig. 3.20 PV test facility of the DTU at campus Risø, Denmark. The short-circuit current and module temperature measurement data of different colored PV single-cell laminates are recorded to validate the angular-dependent angular responsivity model approach.

The spectrometers, used to measure spectral $G_b(\lambda)$ and $G_d(\lambda)$ are connected in series to the data-logger. As a consequence, the required integration time results in a time offset of approximately 15 seconds between the start and end of the measurement. Hence, atmospheric conditions with high cloud variability can lead to significant irradiance changes during this offset. As a result, increased uncertainties compared to clear sky conditions can be expected. In order to filter these timestamps, a variability index (VI) according to Stein et al. [132] is introduced. Therefore, a VI with a threshold of > 1.1 is applied to the data set. Hence, measured broadband G_h values are used in a 2-minute

interval around the respective timestamp. If these timestamps show a VI > 1.1 the corresponding measurement is filtered. As a consequence, only timestamps with stable irradiance conditions between the spectrometer measurements remain in the data-set.

In order to validate the spectrally resolved angular-dependent I_{SC} simulations in this work, the measurement data of the test samples under investigation and of a transparent reference (control) have been recorded. This is done under field conditions in summer in 10-second intervals at the test site of the DTU at Risø Campus (55.7° N, 12.1° E). The measurement data consists of 25 days of short-circuit current measurements of the test samples mounted on a rack at an tilt angle (β=42°) and south orientation (Fig. 3.20). During the field tests, the backsheet temperature T_m of each test sample is measured with a J-type thermocouple attached to the backside with thermally conductive paste and tape. Furthermore, the back sheet temperature T_m of the test samples is measured. The measured I_{SC} values are adjusted to STC (25°C) with the T_m data and short-circuit current temperature coefficient. Measurement data of the in-plane spectral irradiance of the samples during field testing are not available; these data could be used to validate and improve the irradiance modeling approach in this work.

3.4.2 Short-circuit current modeling

The short-circuit current $I_{SC,ASR}$ using $SR(\lambda, \theta)$ of a PV cell or module with a specific active surface area A can be determined by integrating the angular-dependent $SR(\lambda, \theta)$ for a specific AOI θ and the incident solar spectral irradiance $G(\lambda)$ over the relevant wavelength λ range according to:

$$I_{SC,ASR} = A \int_{\lambda} SR(\lambda, \theta)G(\lambda)\, d\lambda \tag{3.10}$$

In (3.10) the spectral solar global irradiance $G(\lambda)$ expresses the total incident irradiation on a PV solar cell or module and needs to be specified more in detail to simulate the I_{SC} under field conditions. Therefore, the particular irradiation components are distinguished in direct and diffuse spectral irradiance in (3.11). By multiplying the measured $G_b(\lambda)$ by the cosine of the AOI θ, the measured $G_b(\lambda)$ is converted to direct in-plane irradiance. Normal incident spectral response $SR_0(\lambda)$ is used to model the I_{SC} for the diffuse sky and ground irradiation components. Finally, an isotropic transposition model for sky and ground reflected diffuse irradiance is applied to simulate the I_{SC} for the PV single-cell laminates mounted on a tilted (β=42°) plane as done in [95]:

$$\begin{aligned}
I_{SC,ASR} = A \int_{\lambda} &SR(\lambda, \theta)G_b(\lambda)cos(\theta) \\
&+ SR_0(\lambda)\left(G_d(\lambda)\left(\frac{1+cos(\beta)}{2}\right)\right. \\
&\left.+ G_{gr}(\lambda)\left(\frac{1-cos(\beta)}{2}\right)\right)d\lambda
\end{aligned} \tag{3.11}$$

The influence of $\tau(\theta)$ for direct and diffuse irradiance to consider reflection losses of oblique incident light in a high-level of detail is modeled as well. Martín and Ruiz presented an analytical model for the $\tau(\theta)$ to simplify the simulation of angular-dependent reflection losses based on a angular loss parameter a_r [64–66]. This parameter is determined by using experimental $\tau(\theta)$ measurements and a least squares Levenberg-Marquardt fitting algorithm. According to [65] the $\tau(\theta)$ is approximated by the analytical expression in (2.3). Furthermore, the measured $\tau(\theta)$ of the test samples is used to take into account the diffuse sky and ground reflected irradiance reflection losses with (2.5). These modifications result in

$$
\begin{aligned}
I_{SC,ASR} = A \int_{\lambda} & SR(\lambda,\theta)G_b(\lambda)cos(\theta) \\
& + SR_0(\lambda)\left(G_d(\lambda)\left(\frac{1+cos(\beta)}{2}\right) F_{d,sky} \right. \\
& \left. + G_{gr}(\lambda)\left(\frac{1-cos(\beta)}{2}\right) F_{d,grd} \right) d\lambda \quad ,
\end{aligned}
\tag{3.12}
$$

for simulation of the short-circuit current $I_{SC,ASR}$ for the respective samples mounted on a tilted plane. In terms of diffuse sky and ground irradiance the broadband reflection losses are considered using the correction factors $F_{d,sky}$ and $F_{d,ground}$ for diffuse irradiance. These correction factors represent the AOI reflection losses of the diffuse irradiation, which is coming from all directions, taking into account a broad range of AOI reflection loss values integrated over a 2π hemisphere.
$SR(\lambda,\theta)$ laboratory measurements are done with $G_b(\lambda)$ and therefore consider spectral reflection losses at varying AOI for direct irradiance component. Thus, an relative transmittance model is not applied for the direct irradiation component in the I_{SC} simulation with the ASR model approach. Since derivation of $I_{SC,ASR}$ requires angular-dependent responsivity data, which is not likely available to most users, the $I_{SC,IAM}$ is also calculated with more commonly available measurements of SR at normal incidence and $\tau(\theta)$, respectively IAM, to correct angular losses of broadband light. Simulated relative transmittance values are used in this broadband IAM modeling approach to consider angular-dependent reflection losses in terms of $G_b(\lambda)$:

$$
\begin{aligned}
I_{SC,IAM} = A \int_{\lambda} & SR_0(\lambda)\left(G_b(\lambda)cos(\theta)\tau(\theta) \right. \\
& + G_d(\lambda)\left(\frac{1+cos(\beta)}{2}\right) F_{d,sky} \\
& \left. + G_{gr}(\lambda)\left(\frac{1-cos(\beta)}{2}\right) F_{d,grd} \right) d\lambda
\end{aligned}
\tag{3.13}
$$

In order to assess the accuracy of the ASR modeling approach in (3.12) with a model that considers only the angular losses of broadband light, the simulation results of both approaches are compared.

3.4.3   Results and discussion

3.4.3.1   Angular-dependent external quantum efficiency

The external quantum efficiency (EQE) is defined as the ratio of incident photons of a certain wavelength that contribute to the photocurrent. Fig. 3.21 shows the plotted linear interpolated
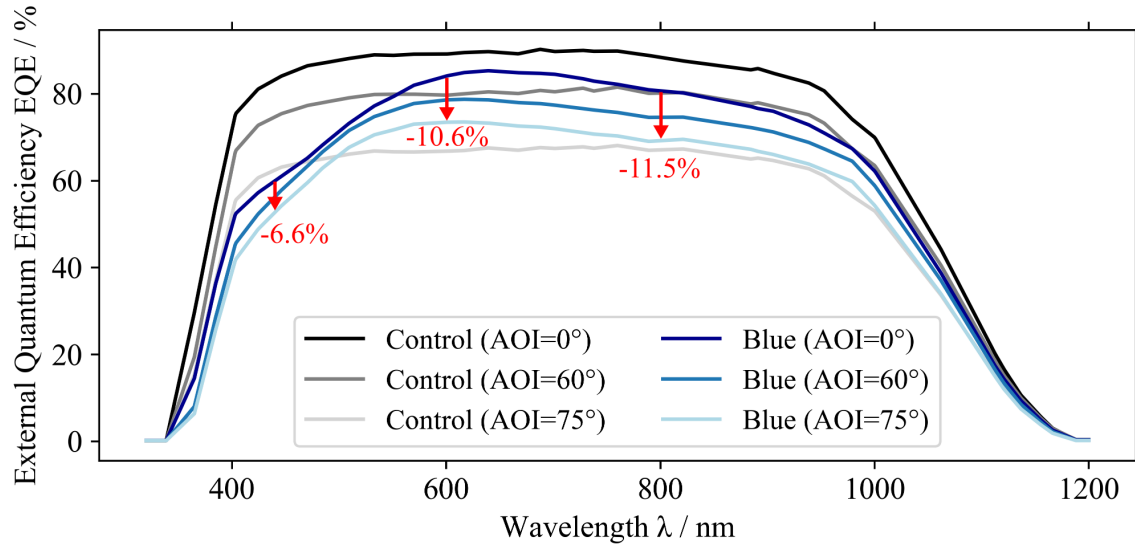
Fig. 3.21 Measured and linear interpolated external quantum efficiency (EQE) of PV cell laminates with transparent (control) and colored (blue) glass cover at different angle of incidence (AOI).

angular-dependent EQE of the transparent (control) and blue colored glass sample. The EQE is determined by means of angular-dependent SR measurements for 0°, 60° and 75° AOI. The influence of the blue colored cover glass on the EQE is visible even at a normal AOI (0°). The blue response reduces the EQE by 27.0%, 18.7% and 5.7% at 450 nm, 500 nm and 600 nm, respectively. The angular-dependent EQE of the transparent sample (control) shows a uniform decreasing spectral difference with increasing AOI. In contrast, a non-uniform decreasing EQE can be observed for the colored samples at increasing AOI. Annotated in red is the reduction of the EQE for an AOI of 75° in comparison to 0° at 450, 600 and 800 nm wavelength, respectively. The EQE of the blue sample drops only slightly in the wavelength range between 300 and 550 nm, while the EQE drops significantly in the range up to 1000 nm. The non-uniform decrease in the EQE can be explained by a characteristic shift of the spectral reflectance peak at the thin-film coating to the shorter wavelength range. The authors in [47] observed a characteristic shift of the spectral reflectance peak to the shorter wavelength range (blue shift) with increasing AOI for the thin-film interference coloring technology. Likewise, for the blue sample in Fig. 3.21, a shift of the EQE maximum with increasing AOI can be observed. The non-uniform reduction of the EQE with increasing AOI shows that the angular-spectral influence of the glass color effect occurs systematic errors when using an broadband IAM model approach.

3.4.3.2 Relative transmittance simulation

Fig. 3.22 shows the measured relative transmittance values of the colored PV single-cell laminates in the respective color of the glass as well as of the transparent reference (control), calculated according to (2.2). In comparison to the control sample, the change of the AOI has less influence on the colored
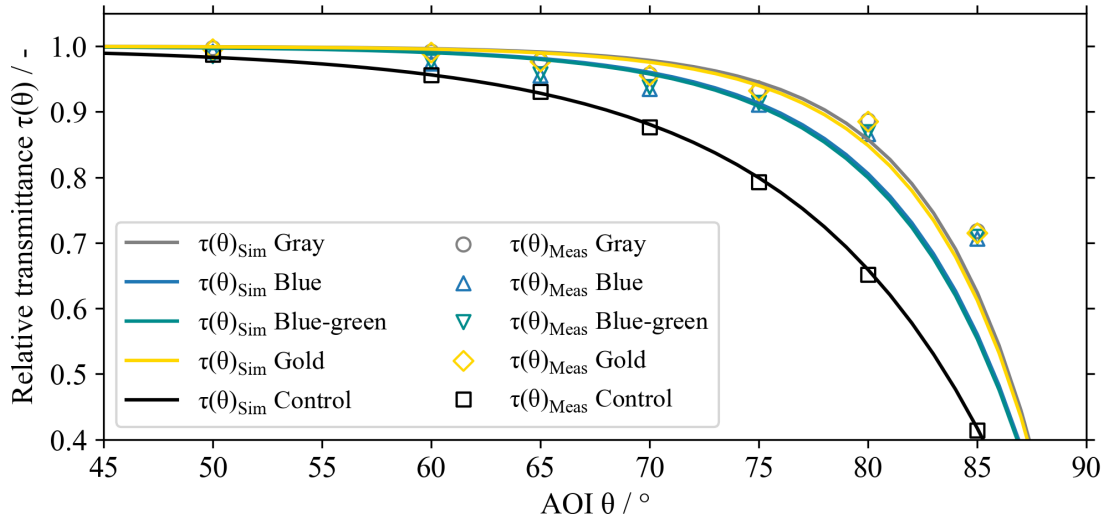
Fig. 3.22 Measured and simulated relative transmittance $\tau(\theta)$ with Martín and Ruiz model for test samples with colored glass and a test control sample.

PV test samples. In addition, the simulated $\tau(\theta)$ of each sample determined according to (2.3) is shown in Fig. 3.22. The a_r-parameter is derived by a least-squares fit of relative transmittance measurement data to (2.3). Table 3.7 shows the respective calculated a_r-parameter and coefficient of determination. Furthermore, the angular diffuse sky and ground irradiance correction factors

Table 3.7 Relative transmittance simulation results.

Sample	a_r	R^2	$F_{d,sky}$	$F_{d,grd}$
Gray	0.089	0.915	0.966	0.989
Blue	0.106	0.859	0.943	0.982
Blue-green	0.108	0.85	0.946	0.981
Gold	0.092	0.911	0.962	0.988
Control	0.162	0.992	0.868	0.955

$F_{d,sky}$ and $F_{d,grd}$ calculated by (2.5) for each test sample with a tilt angle of $\beta=42°$ are shown. In comparison to the control sample, the change of the AOI has less influence on the $\tau(\theta)$ of the colored PV test samples. These observations can be attributed to the structured outer surface of the colored glasses. Comparable measurement results of non-colored etched low-iron float glasses are reported

in [133]. Accordingly, the differences in $\tau(\theta)$ that can be attributed to the thin-film coating are comparatively small. The authors in [134] suggest that these differences are caused by additional reflections depending on the refractive index of the colorants. The colorant changes the refractive index of the glasses and therefore it is not necessarily the color itself that determines AOI performance. However, the suggestions in [134] are limited to inkjet-printed colored glasses with non-structured outer surface.

The Martín and Ruiz angular loss model in [65] shows a good fit regarding standard solar glass. In contrast, a poor fit of the Martín and Ruiz model to the measured $\tau(\theta)$ of the colored test samples can be observed. The poor fit of the colored glasses can be attributed to the fact that their outer surfaces are structured and the model applies only for PV modules with flat outer surfaces. A simulation of the I_{SC} is also done with linearly interpolated relative transmittance measurement data to compare the Martín and Ruiz and interpolation methods. It is observed that linearly interpolated relative transmittance values result in a mean deviation of 0.2% and -6% in terms of the RMSE of the simulated I_{SC} for 25 days of validation for all colored test samples and the transparent (control) sample, respectively. From this test, it is concluded that similar I_{SC} values can be obtained if the relative transmittance data is interpolated or fit to the Martín and Ruiz model. Although the use of $\tau(\theta)$, $F_{d,sky}$ and $F_{d,grd}$ based on a_r is not the most accurate modeling approach to account for the angular-dependent reflection losses of the colored samples considered, these correction factors are used for the I_{SC} simulations in this work. The reason for using this approach despite the observed RMSE deviations is that it is widely used in PV modeling and recommended in the IEC61853 standard. Finally, using a_r and the correction factors for the diffuse irradiance component $F_{d,sky}$ and $F_{d,grd}$, this model enables the consistency of the simulation.

3.4.3.3   Short-circuit current simulation

The I_{SC} of four different colored PV test samples under field conditions are simulated according to (3.12) using $SR(\lambda, \theta)$. Fig. 3.23 shows I_{SC} simulation and measurement results for all test samples in 30-minute resolution on a clear sky day in summer. Likewise, results from the reference (control) with standard glass and residual errors (RE) relative to the respective I_{SC} are shown. Clear-sky conditions prevailed continuously on this day, while the VI can be stated as very low. Under these conditions, the share of the direct beam component in the total incident irradiance is comparatively large compared to the diffuse component. Under these operating conditions, the influence of the $SR(\lambda, \theta)$ on the I_{SC} simulation results is particularly large.

The RE shows a good agreement for both test samples under clear-sky conditions. Furthermore, it shows that the RE increases with increasing AOI for most of the samples, while the RE of the gold and control sample at high AOI decreases to less than 1%. The differences of the RE at high AOI shows the strong influence of alignment errors in measurements, which is consistent with the observation in Riedel-Lyngskær et al. [89]. Therefore, the increased RE at higher AOI can be the result from alignment errors in the lab or in the field. The strongest influence of these errors can be seen in the
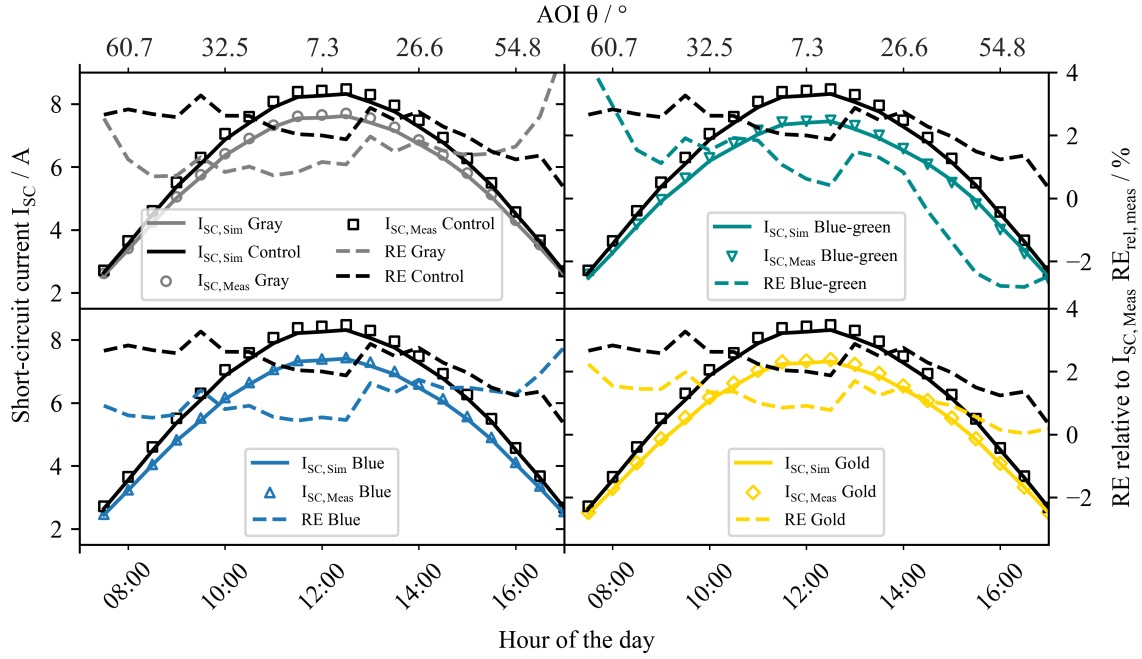
Fig. 3.23 Short-circuit current I_{SC} field measurements and simulations of PV single-cell laminates with colored and transparent (control) glass cover using measured angular-dependent spectral responsivity and spectral irradiance data. Residual Error (RE) is shown relative to the respective measured I_{SC}.

RE of the blue-green sample, the RE ranges from 4% in the morning down to around -2% in the evening. In addition, at certain times of the day, e.g. between 9 am and 1 pm, increased RE can be observed, which could be caused by reflections of surrounding objects. Finally, the transparent test sample shows a slightly larger RE compared to the colored samples.

3.4.3.4   Model validation and statistical error analysis

The ASR model introduced in (3.12) is validated with field data in order to analyze the quality of the predicted I_{SC}. Therefore, the RE between measured and predicted values simulated with the ASR model is calculated. Table 3.8 shows the MBE and RMSE of each colored BIPV test sample under clear sky irradiance conditions. The MBE and RMSE are presented in absolute and relative terms. In addition, Fig. 3.24 shows the RE and a linear regression line as a function of AOI. The data set contains 769 measurements taken over six days in summer with mostly clear sky irradiance conditions. The simulation results for these operating conditions indicate good agreement for all colored test samples, as well as for the transparent reference (control). In particular, the absolute MBE ranges from -30.9 mA to 6 mA for the control and gray sample, respectively. While the control sample has the lowest relative ΔRMSE at 1.4%, the blue-green colored sample has the highest at 2.4%.

The RE of the simulation results for the colored test samples for a data set consisting of 25 days is shown as a function of AOI in Fig. 3.25. This dataset includes 2145 data points during overcast,

Table 3.8 Summarized MBE and RMSE of model validation for 6 clear sky days.

Symbol	MBE	ΔMBE	RMSE	ΔRMSE
Unit	mA	%	mA	%
Sample	**ASR model approach**			
Gray	6.25	0.11	106.1	1.92
Blue	24.9	0.47	92.96	1.76
Blue-green	40.5	0.76	126.3	2.38
Gold	32.13	0.61	91.7	1.74
Control	-30.9	-0.52	82.3	1.38
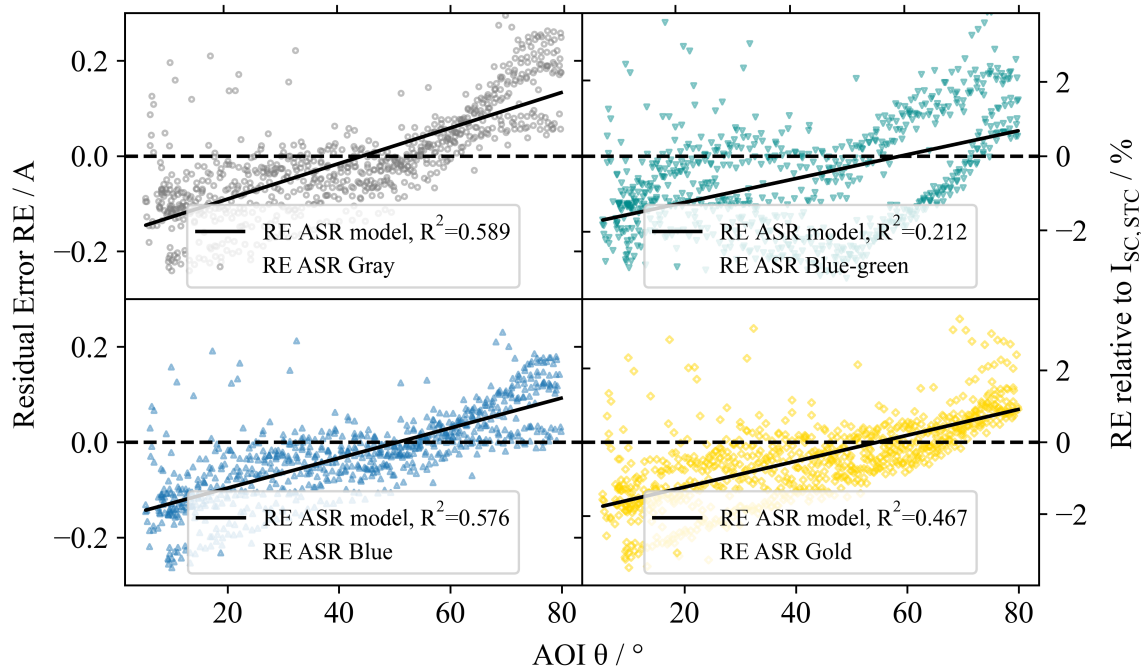
Fig. 3.24 Residual error (RE) of measured and simulated short-circuit current I_{SC} of PV single-cell laminates with colored glass cover over a 6-day period with clear sky irradiance conditions. Simulations are done by using angular-dependent spectral response and spectral irradiance measurement data (ASR model approach).

partly cloudy, and clear sky conditions. Table 3.9 shows the MBE and RMSE for both models (ASR and Broadband IAM). The absolute RMSE ranges from 88 mA to 117 mA and the ΔRMSE ranges between 1.9% and 2.5%. It can be observed that the RE increases with increasing AOI. Moreover, the RMSE and MBE show mostly lower values under clear sky irradiation conditions compared to all-sky irradiance conditions. The simulation results of the I_{SC} using the broadband IAM model are compared to the ASR model results in order to quantify the differences between both modeling approaches. While the ASR model in (3.12) considers spectral, angle-dependent losses, the broadband
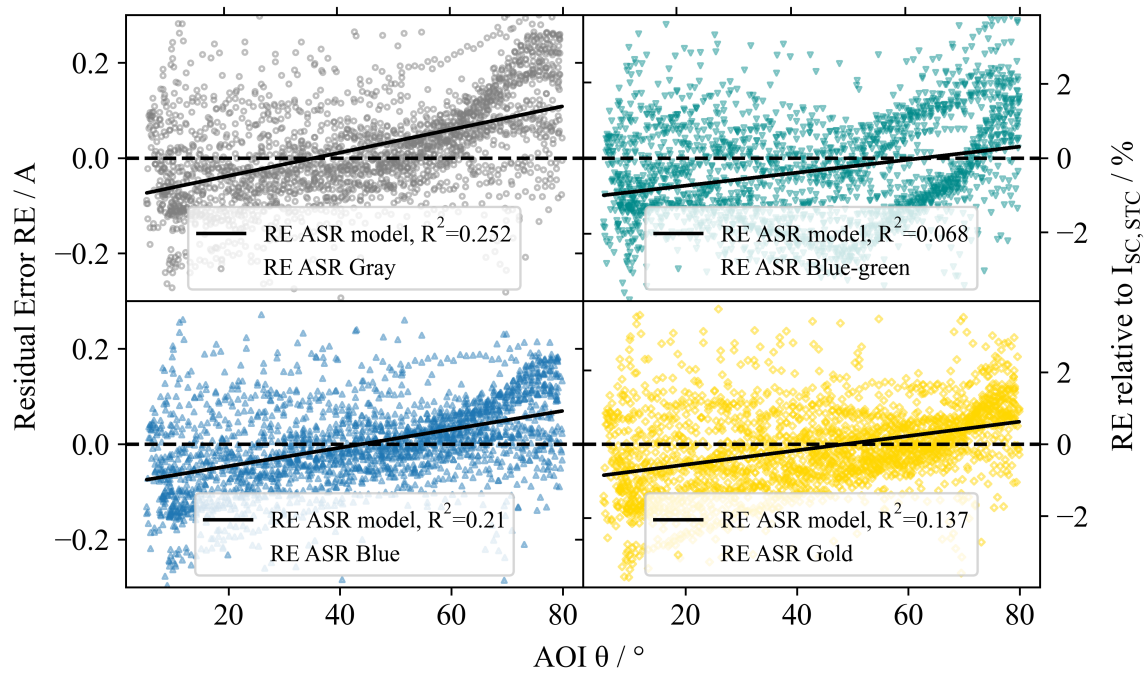
Fig. 3.25 Residual error (RE) of measured and simulated short-circuit current I_{SC} of PV single-cell laminates with colored glass cover for 25 days with all-sky irradiance conditions. Simulations are done by using angular-dependent spectral response and spectral irradiance measurement data (ASR model approach).

Table 3.9 Summarized MBE and RMSE of model validation for 25 days under all-sky conditions.

Symbol	MBE	ΔMBE	RMSE	ΔRMSE
Unit	mA	%	mA	%
Sample	ASR model approach			
Gray	-21.9	-0.45	107.9	2.22
Blue	-1.84	-0.04	91.4	1.96
Blue-green	23.6	0.50	117.1	2.50
Gold	5.1	0.11	88.3	1.90
Control	-52.7	-1.01	104.7	2.00
	Broadband IAM model approach			
Gray	-23.1	-0.47	91.7	1.88
Blue	62.5	1.34	111.4	2.39
Blue-green	74.13	1.58	141.1	3.01
Gold	31.0	0.67	90.1	1.94
Control	-5.4	-0.10	91.0	1.74

IAM model in (3.13) only considers angle-dependent losses with the wavelength distribution of the broadband light source used to determine the IAM. The comparison shows that the MBE and RMSE of the simulations with broadband IAM model are slightly increased or decreased, depending on the glass color, compared to the simulations using the ASR model. In particular, the blue and blue-green colored test sample have increased ΔRMSE of around 0.4% and 0.5%, respectively. In contrast, the gray and control test sample show decreased ΔRMSE in comparison to the ASR model. The gold test sample shows only slight differences in RMSE values using the ASR modeling approach. It is also important to highlight that the RMSE of the laminates with colored glass covers (blue, blue-green, and gold), which show a non-uniform reduction in EQE with increasing AOI, is consistently lower compared to the broadband IAM model. Finally, the results show consistently lower errors and therefore improved accuracy compared to the BIPV simulation studies found in literature [126, 119]. The mean absolute differences between measured and simulated I_{SC} of the colored test samples are shown in Fig. 3.26. In addition, the 95% confidence intervals are calculated and shown for each model approach and test sample. The used data set includes 2145 values from 25 days with all-sky conditions. Although the mean absolute difference values differ only in milliampere, the graph shows that the error for the blue and blue-green colored glasses is significantly lower using the ASR model approach. Moreover, the error values of the gold colored sample are only slightly lower for the ASR
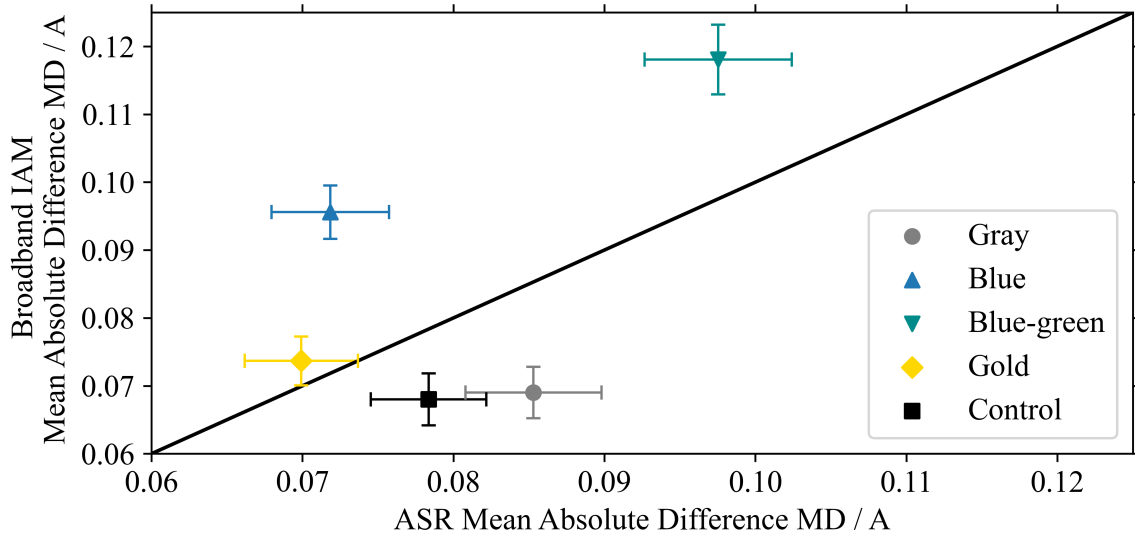
Fig. 3.26 Mean absolute differences and respective 95% confidence intervals of measured and simulated short-circuit current I_{SC} of PV single-cell laminates with various colored glass covers. The simulations are done using two different model approaches, applying either angular-dependent spectral responsivity (ASR) or a broadband incidence angle modifier (IAM) to correct angular-dependent losses.

model approach. These observations confirm the statistical significance of the results and indicate an

improvement in the accuracy of simulations of BIPV modules with colored glasses, which show a non-uniform reduction in EQE with increasing AOI (Fig. 3.21).[5]

---

[5]Fragments of the following section are published in "Experimental assessment of nanoimprinted textured frontsheets for PV modules" (Clasing et al., Proc. 8th World Conference on Photovoltaic Energy Conversion, Milan, Italy, 2022) in [52]

Chapter 4

Optical and thermal optimization of BIPVT modules

4.1 Optical optimizations by means of textured glasses

The installation of BIPVT modules on buildings with suboptimal orientation causes increased optical losses. This has particular disadvantages for building-integrated systems where the orientation and inclination are fixed, such as for BIPVT modules. Light-trapping textures can significantly reduce optical losses at high AOI on the front surface of PV modules and solar thermal collectors, as described in [92, 135]. These textures at mm-scale are already applied to commercially rolled solar glass and are comparatively costly to produce. In contrast, nanoimprints of polyacrylate textured layers are a cost-efficient alternative. A prior study in [51] revealed that nano-imprinted textures on PV modules show improved angular-dependent behavior. Moreover, the authors observed a gain in short-circuit current of around 4% at normal incidence due to anti-reflection properties. However, studies on the annual angle-dependent optical performance of these textures on different substrate materials are lacking in the literature. A recent study published in [134] investigated the effects of inkjet-printed colored glasses on the IAM and their additional optical losses. In this work, an experimental and numerical study is conducted to examine the influence of different textured front covers on the annual angular-dependent optical losses of BIPVT collectors. The relative transmittance of PV single-cell laminates is measured in order to quantify the optical losses of PV modules with nano-imprinted micro-textured front covers in detail. These measurements provide insights into the angle-dependent behavior of PV modules with non-textured polycrystalline solar cells and different textured frontsheet substrates. Next, the recorded measurement data is used to predict the annual improvement of the optical performance of BIPVT modules with textured samples in comparison with non-textured samples. This is done for different orientations, tilt angles and locations. The objective is to assess differences in the IAM between textured and non-textured samples. As a result, significant influences of the textured surfaces on the optical losses of PV modules at high AOI can be identified.

4.1.1   Experimental analysis of textured front covers

This section focuses on angle-dependent losses occurring at the surface of PV modules. In particular, the aim is to determine and assess the influence of micro-textured coatings (with μm-magnitude features) on top of different PV frontsheet substrates at different AOI. Therefore, the IAM of PV modules with different textured and non-textured substrates are measured in a small-scale experiment under constant artificial light in the laboratory. The textures are nano-imprinted on 3 mm thick soda-lime- silicate float glass or 0.125 mm thick polyethylene terephthalate (PET) substrates and are composed of periodically arranged pyramids with heights of 30 μm and a base area of 50×50 μm. Both substrate types were imprinted using an acrylic resin that was cured using UV radiation with a wavelength of 365 nm. The resin differs in the exact chemical composition to maximize the adhesion to the respective substrate. In comparison, two of the respective samples have non-textured surfaces of the same substrates.

Fig. 4.1 shows PV single-cell laminates with nano-imprinted textured and non-textured front covers fabricated at TH Köln (THK). Firstly, 156×156 mm² non-textured poly c-Si solar cells are charac-
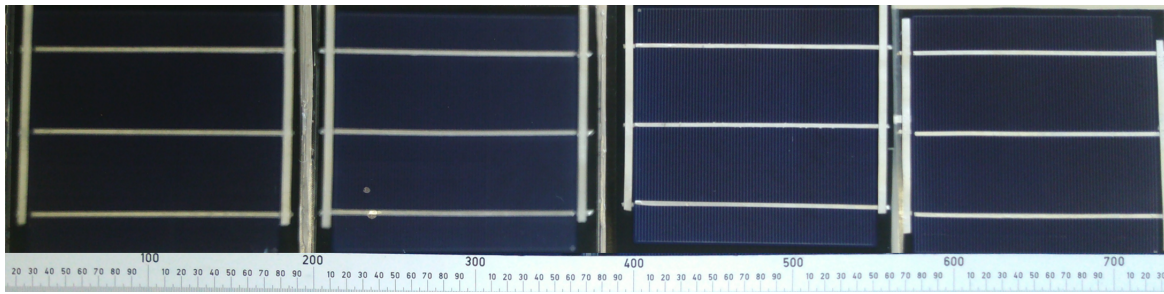
Fig. 4.1 Samples with textured (2 & 4) and non-textured (1 & 3) glass and PET front covers.

terized using a flash light sun simulator and IV tracer to ensure functionality and similar electrical properties at standard test conditions (AM1.5g, 25°C, 1000 W·m^{-2}, STC). Secondly, the electrical contacts are fixed on the cell by manual soldering. Thirdly, the cells are laminat ed using different front covers, conventional 0.45 mm EVA as embedding material and a black PET based foil back sheet. In order to isolate the influence of other parameters during the measurement, the frontsheet substrate is the only one varying component among the samples. Furthermore, non-textured cells are used to isolate the effect of the micro-texturing on the frontsheet. Next, electroluminescence (EL) images are used to analyze the PV modules for damages and defects that could significantly affect the subsequent measurement. Fig. 4.1 shows recorded EL images. The images indicate that the samples under test have no significantly damages or defects. The IAM measurements are conducted indoors, with a constant sun simulator as described in Section 2.4.0.1. The light source is classified as "CAA" according to the IEC standard 60904-9 [136]. To avoid an influence of the busbars on the measurements results, only a small area of the solar cell is illuminated by an aperture. Furthermore, the light beam is more homogenous and even at high AOI there are no cosine-related corrections necessary, as the irradiation on the cell is constant. In addition, there are no temperature induced
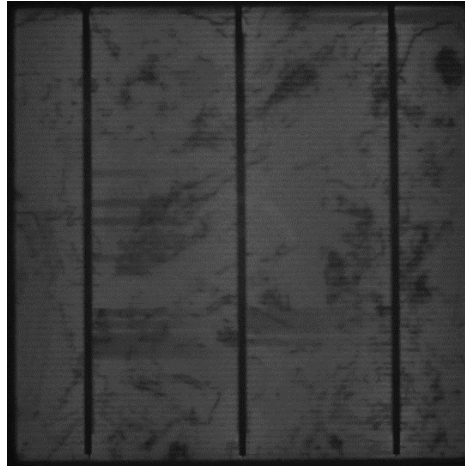
Fig. 4.2 Electroluminescence image of a PV single-cell laminate with non-textured frontsheet fabricated at TH Köln.

side-effects that influence the measurement because the amount of irradiation is not significantly changing the temperature of the samples during the measurement series. Nevertheless, the module temperature is monitored by an RTD on the rear side of the laminate.

The samples are being positioned at the respective AOI automatically on a rotational sample stage, as described in Section 3.1 in order to provide accurate and reliable measurements. The recorded measurement series include an AOI range of 0° to 85° in both directions for each sample. The sample stage provides a positioning accuracy lower than ± 1° regarding the AOI according to the IEC standard 61853-2 [57]. To obtain reliable results, three repetitive measurements are conducted. Therefore, error margins are calculated for random errors, which are evaluated by determining the standard deviation between the resulting six values per angle for every sample.

4.1.2   Impact of textured front covers on annual angular-dependent optical losses

The impact of the improved IAM of textured front covers is analyzed by annual simulations for Cologne, Germany (50.9° N, 7.0° E) and Risø, Denmark (55.7° N, 12.1° E). Therefore, the linearly interpolated relative transmittance data of two nano-imprinted textured and non-textured are used. Likewise, the interpolated data of textured rolled glass, light- and deep-textured, as shown in Fig. 3.8, are used. Moreover, the data of a non-textured rolled standard low-iron solar glass is used for comparison. The relative transmittance of the standard solar glass is derived from the model of Martín and Ruiz in (2.3) and (2.5) with $a_r = 0.16$. The simulations are based on decomposed TMY irradiance data derived from PVGIS in [107]. More details of the used data sets is described in Section 5.2.2. The TMY data sets are used to calculate the angular-dependent optical losses for these two locations. The decomposed data includes GHI, DHI and DNI and is used to model different tilt angles and orientations. Four different tilt angles from 30° to 75° with an azimuth orientation of 90° (0°=North) are considered. The diffuse transposition model of Perez in [97] and an albedo

of 0.2 for dry concrete are used to calculate the in-plane irradiance components. The optical losses are simulated using linearly interpolated relative transmittance measurements of the textured and non-textured test samples to correct direct beam irradiance. In addition, angular correction factors for diffuse sky and ground-reflected irradiance are applied as described in [67]. Next, the effective irradiance G_{eff} is calculated using (2.6) for each sample to analyze the angular optical losses. Finally, the relative increase in angular-dependent annual optical performance ΔE_{eff} is calculated as the ratio between the textured and corresponding non-textured samples as

$$\Delta E_{eff} = \frac{E_{eff,tex}}{E_{eff,non-tex}} = \frac{\int G_{eff,tex}\, dt}{\int G_{eff,non-tex}\, dt}, \tag{4.1}$$

where E_{eff} is the effective irradiated solar energy determined by integrating G_{eff} over time.

4.1.3   Results and discussion

The plots in Fig. 4.3 and 4.4 show the averaged values of three repeated measurements for each sample and AOI, as defined the standard IEC 61853-2. The error bars represent the standard deviation
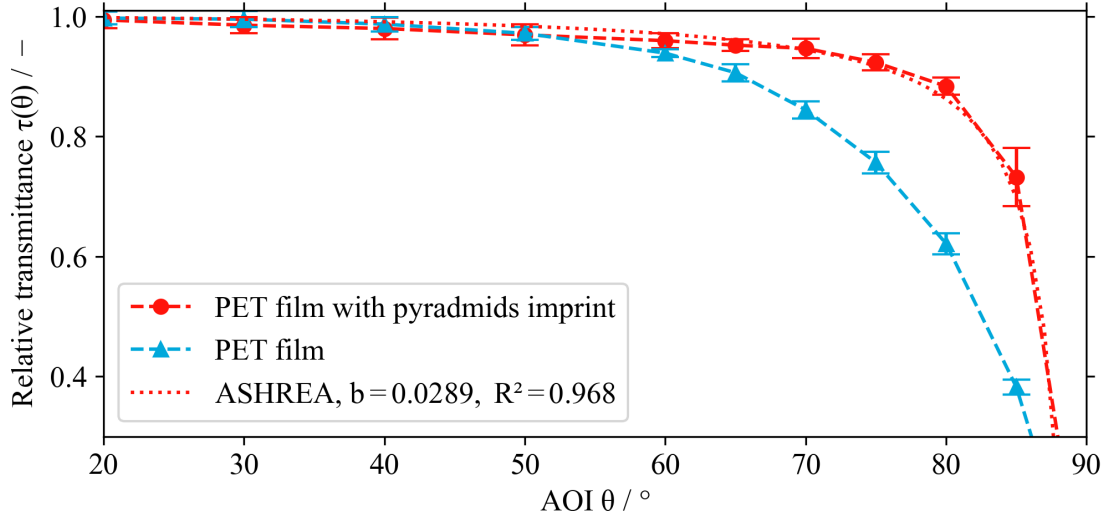
Fig. 4.3 Averaged relative transmittance measurement values and least-squares fitted ASHREA angular loss model of the micro-textured PET frontsheet test samples as a function of angle of incidence (AOI).

of every averaged value. In Fig. 4.3, the relative transmittance measurements for the samples with PET frontsheet are shown for AOI up to 85°. While both samples show low angular-dependent optical losses up to an AOI of 50°, a slight difference can already be observed at an AOI of 60°. While the non-textured PET sample shows relative transmittance values of only 0.38 at 85°, the relative transmittance for the textured sample amounts to 0.73. The IAM gain of the textured sample compared to the non-textured one amounts to around 12 $\%_{rel}$ at 70°, around 42 $\%_{rel}$ at 80° and around 92 $\%_{rel}$ at 85°.

Fig. 4.4 shows the relative transmittance measurements for the samples with flat glass for AOI up to 85°. In comparison to the PET samples, the glass samples show increased angular-dependent optical losses up to 50° AOI. In addition, the relative transmittance show only slight differences at 60° AOI. The relative difference at AOI > 60° is slightly lower but comparable with the PET samples. The non-textured flat glass sample shows relative transmittance values of 0.34 at 85°. In comparison, the relative transmittance for the textured sample showed 0.69. The relative transmittance gain of the textured glass sample compared to the non-textured one is around 9$\%_{rel}$ at 70°, around 21$\%_{rel}$ at 80° and around 101$\%_{rel}$ at 85°. The standard deviations for AOI $\leq$ 80° are between 0.01 and 0.02. In contrast, the error margins for the non-textured glass sample are larger at 0.03. The largest standard deviation for relative transmittance measurements is observed for AOI > 80° with 0.08 for
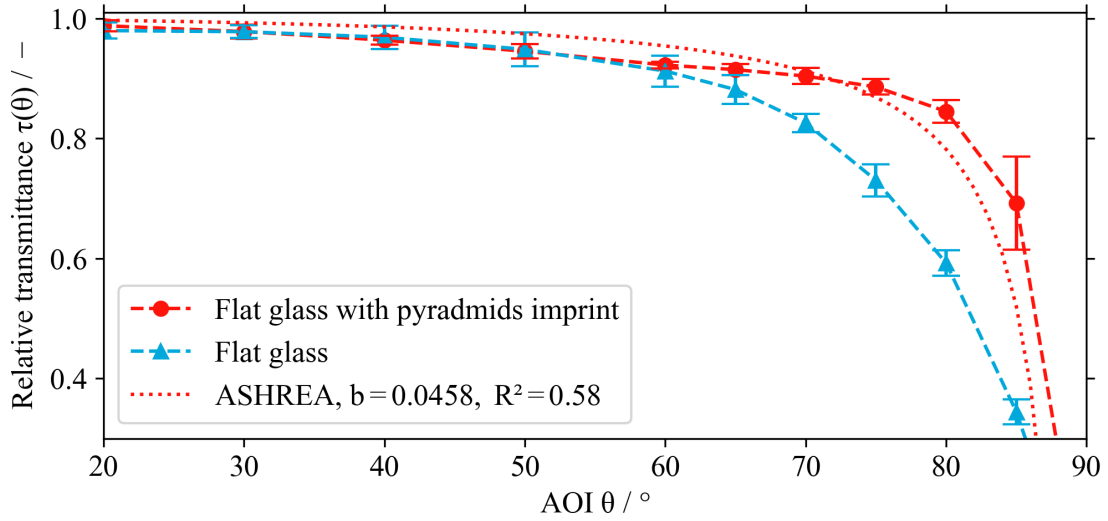
Fig. 4.4 Averaged relative transmittance measurement values and least-squares fitted ASHREA angular loss model of the micro-textured flat glass frontsheet test samples as a function of angle of incidence (AOI).

the textured glass and 0.01 for the non-textured PET.

As expected, the textured samples show an improved angular behavior. Although the flat glass samples show slightly less angular performance at high AOI, the results are consistent. This can be explained by the non-textured glass sample which shows increased angular-dependent optical losses compared to the non-textured PET samples. Accordingly, the relative transmittance is lower, but in a similar ratio. The error margins are in an acceptable range for both textured substrates for AOI values < 80° AOI. In contrast, the error margins of the 85° values are considerably larger. The authors of an interlaboratory study in [89] found that relative transmittance measurements in an AOI range from 70° to 85° deviated from the weighted mean by 2.5% to 23%. In particular, the largest uncertainties were found for the AOI range of 85° and therefore further the authors suggest corrective actions in the IEC standard. Thus, the results are limited in this AOI range. The least squares fit with the ASHREA angular loss model as applied in [59, 60] shows good agreement for the PET sample. For the glass sample, rather a poor fit is found for commonly used models, as described in Section 2.1. In order to increase comparability within the annual simulations, the measured data used to model the angular-dependent optical losses are linearly interpolated.

The measurement values are used to determine the potential increase in angular-dependent optical performance under real operating conditions by means of time-series based simulations. Therefore, the effective irradiance of non-textured and textured front covers is simulated and compared to quantify this increase. Fig. 4.5 shows the relative gains for tilt angles between 30° and 75° for different front covers and textures in Cologne, Germany. The reference is based on the corresponding cover without texture. The nano-imprinted glass and PET show similar relative gains for the respective surface tilt
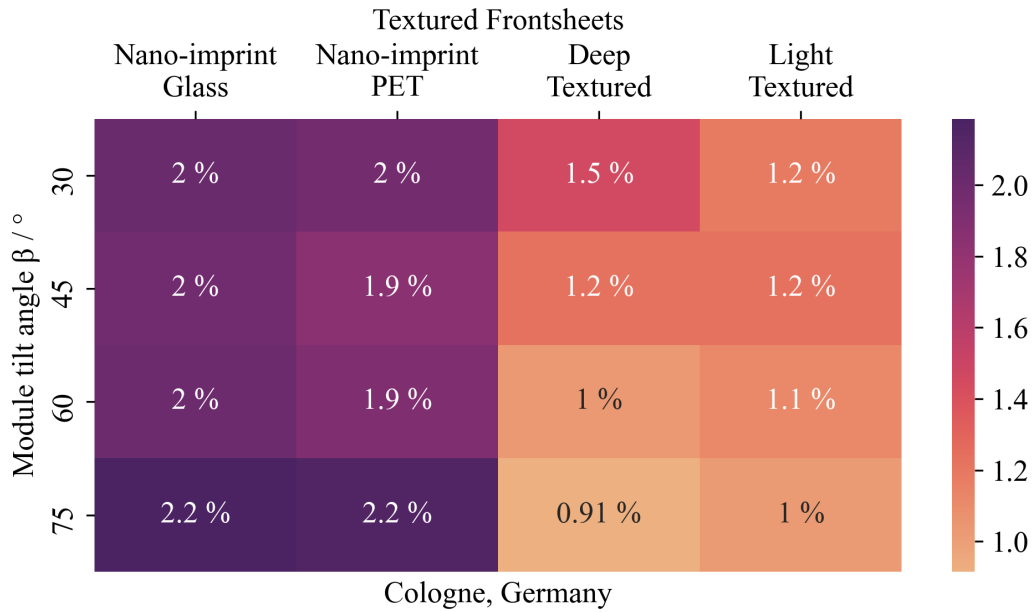
Fig. 4.5 Relative increase of annual angular-dependent optical performance of an east-facing module surface in Cologne, Germany (50.9° N, 7.0° E).

angles. The highest gain can be observed for 75° with 2.2%$_{rel}$. In comparison, the rolled textured glasses show the highest values for a tilt angle of 30°. While the deep-textured glass shows a relative gain of 1.5%$_{rel}$, the light-textured glass shows only 1.2%$_{rel}$ for this tilt angle, respectively. In contrast, for 70° tilt angle the deep-textured glass shows the lowest values for Cologne, Germany with 0.9%$_{rel}$. Fig. 4.6 shows the relative increase of optical performance for Risø, Denmark. The values range between 0.9%$_{rel}$ and 1.9%$_{rel}$ for the deep-textured and nano-imprinted textured glass, respectively. Similarly to the Cologne results, the nano-imprinted samples consistently show increasing but lower values with increasing tilt angle. In contrast to the results in Cologne, the light-textured glass shows higher values than the deep-textured glass. The highest values for the rolled glasses range from 1.1%$_{rel}$ to 1.2%$_{rel}$ for the deep- and light-textured, respectively.

The relative increase of angular-dependent optical performance shows consistent values for the nano-imprinted textured samples. However, the values are decreased for Risø. This can be explained by the lower sun elevation angle in eastern orientation. Thus, the AOI distributions are in a lower range compared to Cologne. The nano-imprinted textures show the largest increase of angular-dependent optical performance for all tilt angles and locations. This can be attributed to the improved angular behavior, especially at high AOI. Moreover, the highest values are observed for a tilt angle of 70°, which can be explained by the low sun elevation angle in eastern orientation and thus a high share of low AOI. In contrast, the rolled textured glasses show lower a increase and the highest values for tilt angle of 30°. The deep-textured glass shows only slight improvements in comparison to the light-textured at a tilt angle of 30°. For higher tilt angles, the increase is even slightly larger for
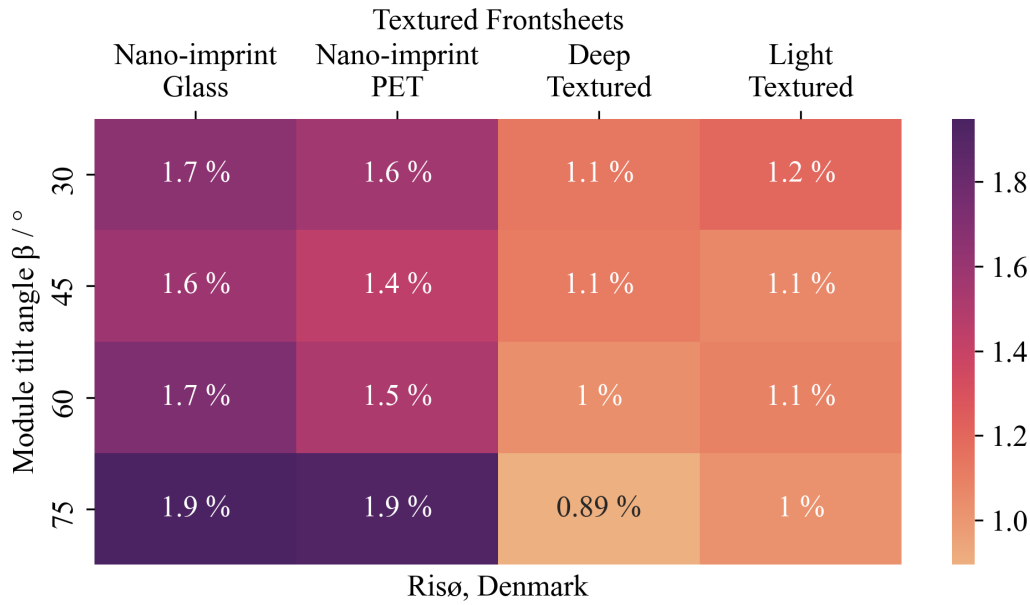
Fig. 4.6 Relative increase of annual angular-dependent optical performance of an east-facing module surface in Risø, Denmark (55.7° N, 12.1° E).

light-textured glass. However, the absolute transmittance of the different substrates and textures must be considered to evaluate the exact overall performance of the nano-imprinted front covers. These textures show a $4\%_{\mathrm{rel}}$ increase in optical performance for normal incident light, as described in [51]. Overall, these properties in addition with the results of this work indicate that the nano-imprinted textures are promising for application in BIPVT modules.

In summary, the results indicate strong evidence that nano-imprinted textures have an impact on the reduction of angular-dependent optical losses on the front covers of PV modules and solar thermal collectors. Finally, these textured front covers can be used in building-integrated solar applications such as BIPVT modules with suboptimal orientation in order to improve energy yields and reduce the LCOE. However, the results are limited in terms of the optical AOI losses. Optical properties such as transmittance, reflectance and absorption are not considered, and therefore a more detailed study is recommended.

4.2 Thermal optimization by variation of mass flow rate and air leakage

The thermal performance of air-based BIPVT systems is largely dependent of heat transfer on the mass flow rates, air leakage and design of the air duct. Therefore, studies on air duct design optimizations and harmonized evaluation approaches have been carried out in [53–56, 137]. Studies about these optimizations in terms of air-based BIPVT systems are sparse in the literature. The optimizations are focused on different air duct depths [36, 15], multiple inlets [48, 29] and micro-channels [138].

Especially for building-integrated systems, air leakage is even more difficult to control compared to PVT air collectors mounted in an open rack. The construction design of BIPVT systems is more complex and must be aligned with building code requirements. In addition, multi-functionality such as aesthetics, ease of installation and maintenance, and thermal insulation for the building must be considered. The objective of this study is to determine the optimal mass flow rate and analyze the influence of air leakage on the performance of the system.

The thermal performance of solar thermal air heating systems increases with mass flow rate. However, the mechanical energy required to drive the fan has to be considered in the energy balance. The authors in [56] calculate the effective efficiency, or thermo hydraulic efficiency, also known as efficient boundary mass flow (EGM) in [53–55], to determine the optimal design of fin absorber solar air collectors. The thermo hydraulic efficiency is used in this work to determine the optimal mass flow rate for the given geometrical design of the BIPVT module using a numerical approach. Therefore, the electrical energy power of the fan P_{fan} can calculated according to (3.9) with $\eta_{fan} = 0.18$ from [106]. Subsequently, the effective thermal efficiency η_{eff} can be determined according to [56] as

$$\eta_{eff} = \frac{\dot{q}_{th,eff}}{G} \tag{4.2}$$

with

$$\dot{q}_{th,eff} = \frac{\dot{m} \cdot c_p \cdot (T_o - T_i) - P_{fan}}{A}. \tag{4.3}$$

Steady-state climate reference conditions are defined by the ISO9806 standard in [94] and used for the determination of the optimal mass flow rate. The conditions are classified from class A (very sunny) to class C (temperate). Class A reference conditions are defined as a minimum of $1000 \, \text{W} \cdot \text{h}^{-2}$ irradiance on the collector plane G_i and 20°C ambient temperature T_a. These conditions are used for the simulations in order to identify the optimal mass flow rate of the BIPVT system. Furthermore, different geometrical air leakage sizes are studied. The leakage in the air duct are on every BIPVT module transition is on the rear and front sides, as shown in Fig. 3.4.

The simulation is done using the BIPVT model described in Section 3.3. The efficiencies are calculated in $12.5 \, \text{kg} \cdot \text{h}^{-1}$ step sizes for two different collector designs. The first design is an airtight collector with an air leakage mass flow rate set to zero. The second design has a 1 mm leakage on the front and rear sides of the glass-glass module in the BIPVT module, as shown in Fig. 3.4. The corresponding air leakage mass flow rates are derived by CFD simulations as input parameters. These leakage rates are linearly interpolated in a range of 0-300 $\text{kg} \cdot \text{h}^{-1}$.

The thermal efficiencies are determined for a BIPVT system operated in hybrid MPP mode. Accordingly, electrical efficiency is considered in the energy balance. Therefore, the electrical efficiency is provided as an input parameter to the thermal model. The thermal efficiency in this study is calculated for a PV system at STC and under real module operating temperatures.

4.2.1 Effective efficiencies at standard test conditions

Fig. 4.7 shows the simulated thermal and effective efficiency of 12 active rear ventilated BIPVT modules connected in series as a function of mass flow rate. The results are calculated using (4.2) and Class A reference conditions according to [94]. The wind speed is not defined in the standard and is therefore set to a constant value of $1\,\mathrm{m\cdot s^{-1}}$ for all operation points. In particular, the wind speed has a large impact on the thermal efficiency of unglazed air heating systems and therefore cannot be neglected. While the solid lines indicate the thermal efficiency, the dotted lines indicate the effective
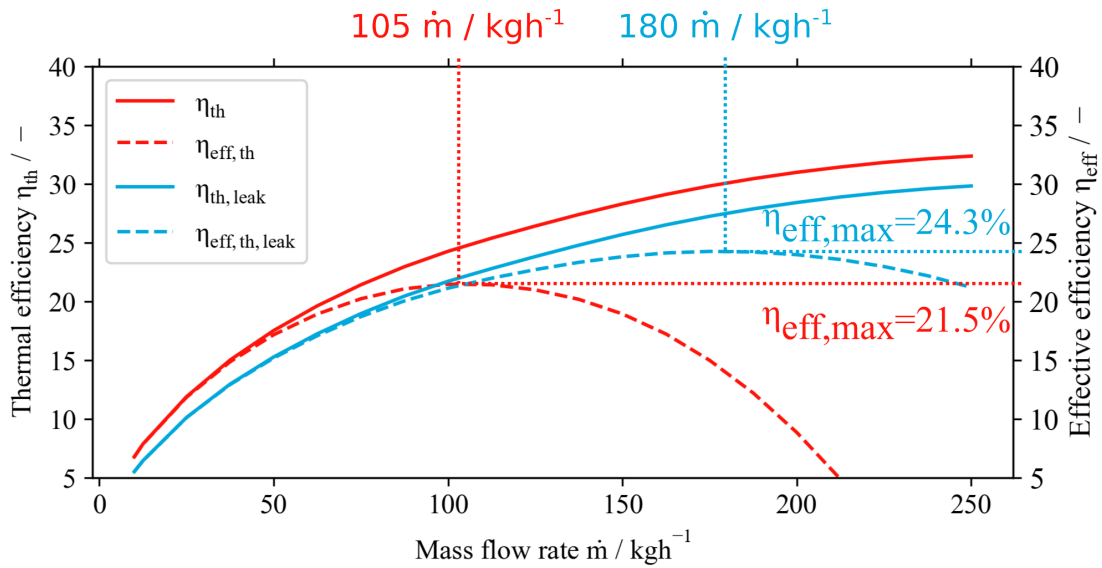
Fig. 4.7 Effective efficiency of the BIPVT system as a function of mass flow rate. The system consists of 12 BIPVT modules connected in series.

efficiency. The values for effective and thermal efficiency initially increase consistently for both air duct designs, whereas the airtight design has higher absolute values. However, the slope of the curve decreases with increasing mass flow rates. The values show that the effective efficiency of the airtight design drops earlier and more sharply due to the increased fan power. In contrast, the curve of the design with air leakage shows a flatter slope.

The dotted lines show the maximum effective efficiency at specific mass flow rates for both designs. The airtight design reaches its maximum at $105\,\mathrm{kg\cdot h^{-1}}$ with $21.5\%_{\mathrm{abs}}$. In comparison, the design with air leakage shows a maximum effective efficiency of $24.3\%_{\mathrm{abs}}$ at $180\,\mathrm{kg\cdot h^{-1}}$. The results show a relative increase of the maximum effective efficiency of $13\%_{\mathrm{rel}}$ for design with air leakage.

The results show that the airtight BIPVT module design has increased maximum thermal performance in comparison to the air leakage design. However, the effective efficiency of the BIPVT module with air leakage is higher when taking into account the thermo-hydraulic performance. The thermo hydraulic performance considers the fan power required to operate the rear ventilation system at the corresponding mass flow. The increased pressure difference between the inlet and outlet explains the

decreased values for the airtight design of the system. This increased pressure difference increases the mechanical fan power, according to (3.8). These results indicate that leakage in the air duct can optimize the effective thermal efficiency and, therefore, the overall performance of the system. Nevertheless, the results are limited to the assumptions of the model. The simulation has been done for 12 BIPVT modules connected in series, including the ridge construction. The air leakage in the ridge construction is not considered in this study, and therefore the effective efficiency can be even increased for the experimental system studied in this thesis.

Chapter 5

Assessment of measured and simulated BIPVT system performance

5.1 Experimental assessment of an optimized BIPVT system

To analyze the performance of the optimized BIPVT system and validate the developed simulation model, field measurements are conducted on an experimental setup at THK in Cologne, Germany. Fig. 5.1 shows an overview with the BIPVT test system a), reference PV system b), dual-axis sun tracker c), and all-in-one weather station d). The objective of this experimental analysis is to compare
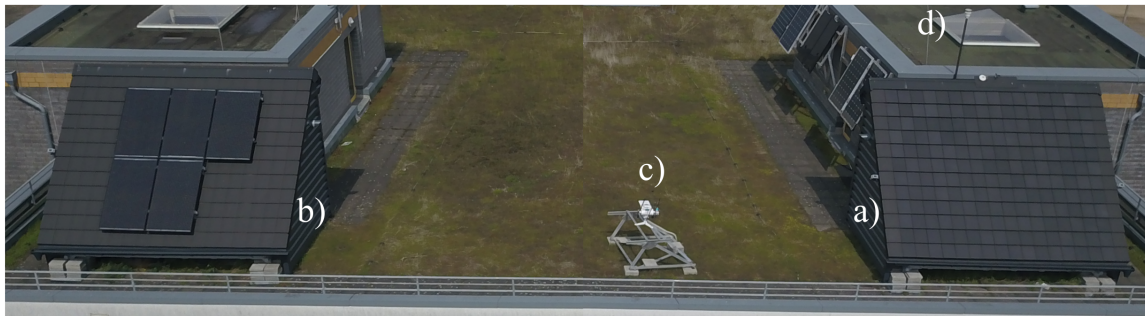
Fig. 5.1 Overview of the experimental field setup: Test roof with BIPVT system a) and reference roof with a conventional PV system mounted on an open-rack b).

the performance of the optimized BIPVT system with a conventional PV roof system (reference) mounted on an open rack. The roof structures (Fig. A.8) correspond to a conventional insulated 45° tilted timber-frame construction and have an identical orientation at 170° azimuth (0°=North). Thus, it is assumed that the environmental conditions of both systems are approximately the same and the weather station in Fig. 5.1 d) can be used to monitor the conditions of both systems. However, the shading from surrounding objects and the inclination of the module surface due to the construction designs are different. The construction design of the BIPVT module includes an overlap of each

module, which results in a 40° tilted plane due to a compensation angle. In contrast, the surface tilt of the PV modules on the mounting system on the reference roof is parallel to its roof inclination. In order to compare the electrical output of both systems, the measurement data must be normalized by means of the PR. An overview of the experimental setup is shown in Table 5.1 and is described in detail in the following Section 5.1.1.

Table 5.1 Experimental BIPVT and reference PV system.

Parameter	Location and orientation	
Location	Cologne, Germany	
Latitude	50°56'02,6"N	
Longitude	6°59'25,1"E	
Altitude	60 m	
Surface azimuth	170°	
System	**Electrical**	**Thermal**
BIPVT	2x96x14.4 Wp, Total 2.8 kWp Custom PV module Surface tilt: 40°	ASHP coupled with rear-ventilation air heating system, A_g=15.6 m²
Reference PV	5x310 Wp, Total 1.6 kWp SOLARWATT, Vision 60M style Surface tilt: 45°	ASHP operated with ambient air

The installation and configuration of the monitoring system are done in accordance with the monitoring standards for PV modules in [139] and outdoor testing standards for solar thermal collectors in [94]. These standards define the types, required accuracy and arrangement of the measurement devices as well as data filtering, recording & sampling procedures. System operation parameters and weather data are measured on site, the datasets are recorded in 20-second intervals and stored in a database. These data are used for experimental analysis of the optimized BIPVT system and additionally for validation of the simulation model in Section 3.3.4.

5.1.1   Experimental setup

The BIPVT module design under study is described in Section 1.2. The front of the glass-glass module is covered with a light-textured solar glass. The measured and simulated relative transmittance of this glass cover is shown in Fig. 3.8. The air duct of the rear-ventilation system has an effective length L of 0.34 m due to the overlap of each module. The air duct has dimensions with a height and width of 0.02 m × 0.24 m and thus a cross-sectional area of 0.0048 m². The cross-section of the air duct is shown in Fig. 3.6. Fig. 5.2 shows the optimized BIPVT test system with 192 modules. The system is operated in hybrid MPP mode during all test series unless otherwise specified. The PV modules
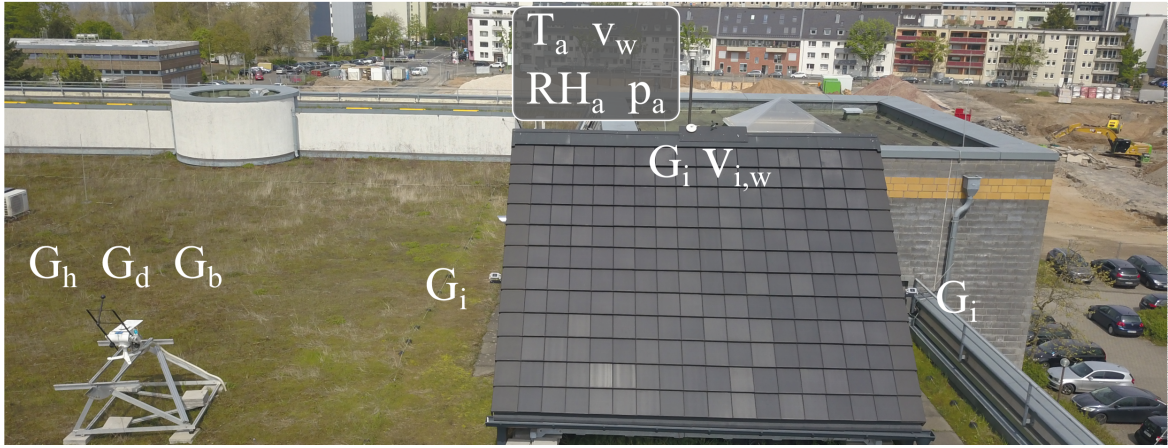
Fig. 5.2 Experimental setup with 192 BIPVT modules (2x1.4 kWp, 15.6 m² active rear-ventilated aperture area).

are connected in two parallel strings (2x1.4 kWp) with a total surface area of 19.2 m². Each string is connected to an adequately sized PV inverter. In comparison, the PV reference system consists of one PV string with five modules (1.6 kWp) connected to an inverter. Both systems are connected in parallel to the grid with an identical inverter.

The solar air heating system is configured with 16 tilted parallel air ducts with each 12 modules connected in series as shown in Fig. A.1. The total length L of a parallel air duct system with 12 modules is 4.37 m. The outlets of the air ducts are connected to a volume in the ridge of the roof as shown in Fig. 5.3. A pipe is installed in the ridge and has linearly increasing inlet sizes from the center to the outside of the roof to provide uniform mass flow distribution. A total of 12 parallel air ducts are connected to the pipe in the ridge of the roof for active rear ventilation (Columns C-N, see Fig. A.1). Depending on the test series performed, this pipe is either connected to an ASHP or to the ambient air by an outlet pipe. However, two parallel air ducts on each side of the test roof are not connected to this pipe and hence these modules are only passively rear-ventilated (Columns A-B & O-P, see Fig. A.1). These passively rear ventilated modules are used for a comparison of module and air fluid temperatures with the actively rear-ventilated modules. Finally, the temperatures can be monitored and analyzed simultaneously under the same ambient conditions using this experimental setup.

The air duct system connected to the outlet of the BIPVT system is shown schematically in Fig. 5.4. The air flow distribution can be controlled by the ventilation flaps and the volume flow is generated by a variable-speed axial tube fan. These control devices are used to perform different test series (active and passive rear ventilation of the BIPVT). If both ventilation flaps (1 & 2) are open, air can flow into the environment. In order to avoid uncertainties caused by the exhaust air during operation, the height and position of the outlet ensure that preheated air cannot re-enter the system inlets. If only ventilation flap 2 is opened, the heat pump is fed by preheated ambient air from the BIPVT rear ventilation system. By using this air, the COP of the ASHP is expected to be improved compared to operation with ambient air. These systems are also known as SAHP in [140, 141]. An additional tube
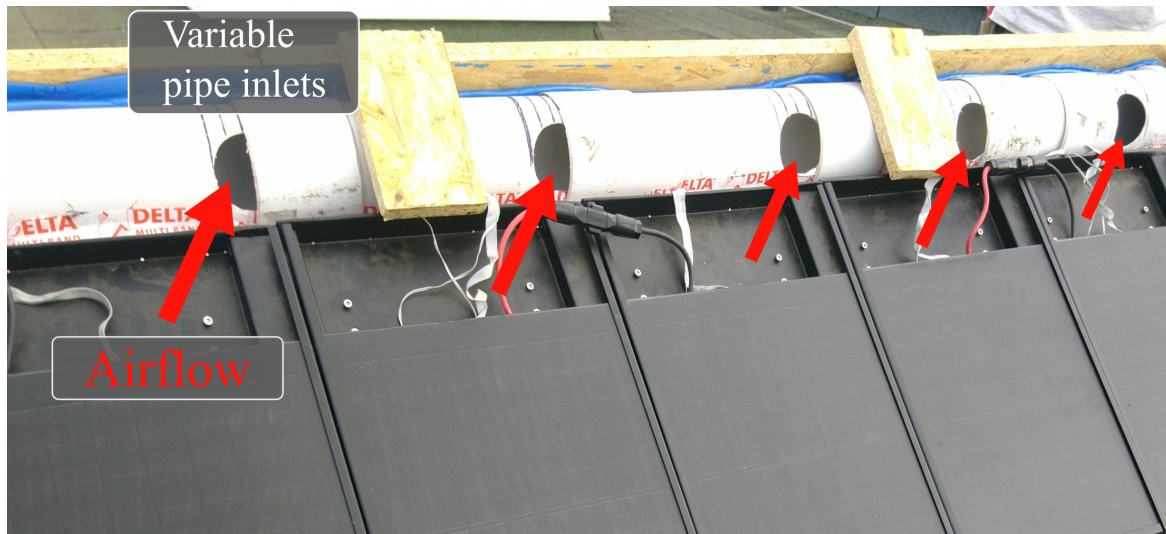
Fig. 5.3 Rear ventilation outlets of the BIPVT system and pipe inlets of the heat recovery system with variable inlet sizes at the ridge of the test roof.
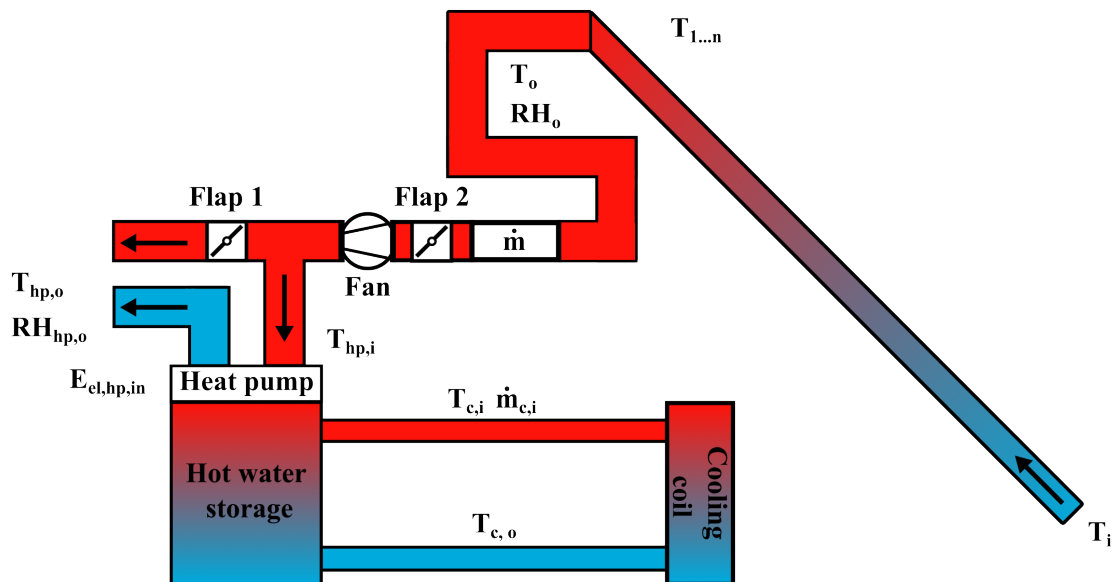
Fig. 5.4 Schematic representation of the BIPVT test system. The rear-ventilation outlet is connected to an air-source heat pump as well as to the ambient air by an air duct system. The temperature of the water in the storage tank is reduced for test purposes using a cooling coil and the ambient air.

fan is installed in the air duct system between the rear ventilation of the BIPVT system and the inlet of the heat pump to support its ventilation system. Moreover, tests without the heat pump are performed by using the tube fan. In order to compare the performance of the SAHP with a conventional system, an identical ASHP is installed on the reference roof and operated with ambient air. If only ventilation flap 1 is opened, the ASHP on the test roof is operated with ambient air. This operation mode is initially used to compare both heat pump systems in order to demonstrate identical operation behavior.

5.1.1.1 Data acquisition and control system

The data acquisition and control system used in the field setup consists of two identical embedded industrial controllers (cRIO-9056, National Instruments) with a Field Programmable Gate Array (FPGA) module and reconfigurable input and outputs in the test and reference roofs. The data
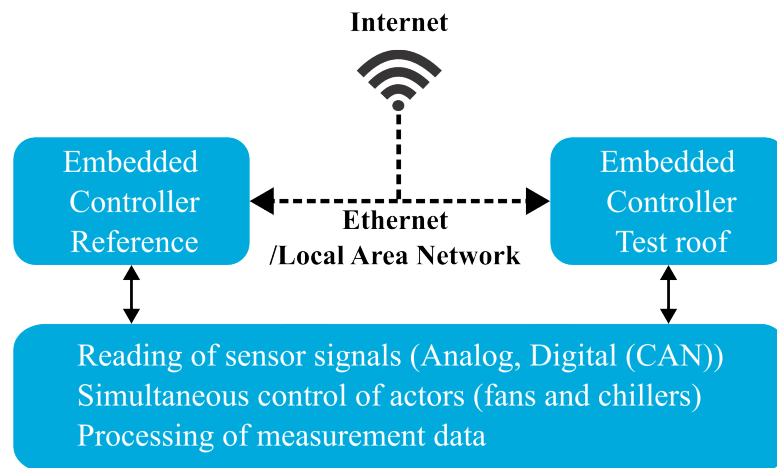
Fig. 5.5 Schematic overview of the data acquisition and control system used for the experimental test series.

acquisition and control software was developed in LabVIEW in [142]. A schematic representation of the system is shown in Fig. 5.5. The real-time controllers acquire, process and record the analog and digital measurement signals of the installed sensors. The temperature, voltage and current sensors integrated in the BIPVT modules have a digital communication interface based on a Control Area Network (CAN) field bus implementation. This implementation was developed in [143, 144]. The FPGA module is used to control simultaneously the fans and cooling coil during the experiments. The used system is specified for operation in a temperature range between -20°C and 55°C and is therefore well suited for use in a long-term field measurement setup at the test site. In addition, the controllers on both roofs are connected to the Internet by a Local Area Network (LAN) to remotely control the experimental test series and merge the recorded data into one data set.

5.1.1.2   Measurement setup

The weather data is measured on the experimental field test site and includes a detailed irradiance data set. The ambient wind speed v_w, wind direction, relative humidity RH_a, temperature T_a, pressure p_a and precipitation quantities are measured with an all-in-one weather station (Clima Sensor US NHTFB, Thies Clima) at a height of 1 m above the test roof. In addition, the in-plane wind speed parallel to the aperture surface is measured by a three-cup anemometer as an input parameter for the convective heat losses model in (2.8) and (2.9). The solar irradiance data for the field test is measured i) on a dual-axis sun tracker with a class A pyranometer (CMP11, Kipp+Zonen) and a pyrheliometer (MS-57, EKO Instruments), ii) on the test roof with a class A pyranometer (CMP11, Kipp+Zonen) and two c-Si reference cells (Si-mV-85-Pt100-4L, Si-V-10TC-13, Mencke & Tegtmeyer) and iii) on the reference roof with a c-Si reference cell (Si-V-10TC-13, Mencke & Tegtmeyer). The different devices are installed for the different test series. While the c-Si reference cells are used for PV performance analysis and electrical model validation, the pyranometers are used to analyze the thermal performance and validate the thermal model. The irradiance measurement devices are calibrated before starting the test series. While the pyranometer and pyrheliometer are calibrated according to the ISO 9847 [145] standard, the c-Si reference cell devices are calibrated according to the standard IEC60904-1 [146]. Temperature and relative humidity are monitored in different parts of the BIPVT system. While the temperature measurements are based on customized thermistors (NTC) and standardized RTD, the relative humidity sensors are based on electronic devices with analog output signal interfaces. The module temperature T_m as well as the temperature measurements of the air T_{air} in the rear ventilation are conducted with a total of 232 NTC devices. Two different NTC temperature sensor arrangements are mounted on the back side of the glass packages. These sensors are mounted either with silicone (left: air) or are embedded in thermally conductive paste (right: module) as shown in Fig. 5.6. More sensor positions are in selected positions of the BIPVT system, as shown in Fig. A.6 (Appendix A). The temperature distribution of the BIPVT system can be analyzed with spatial resolution due to the
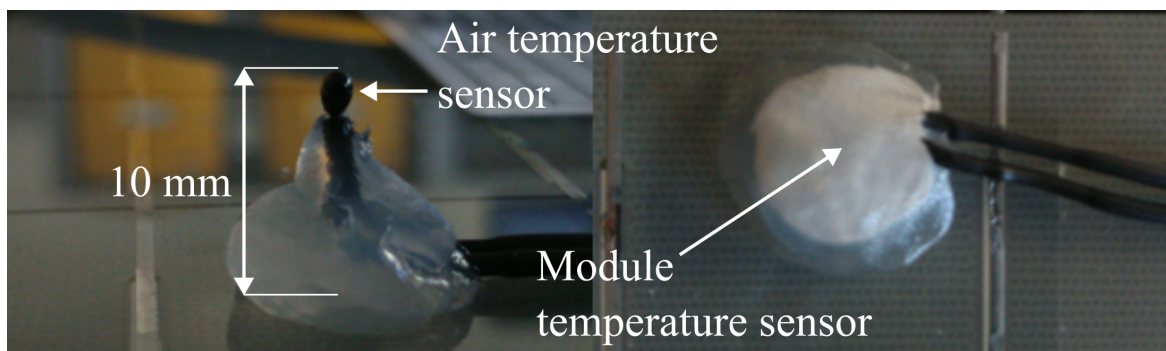
Fig. 5.6 Fluid (left) and module (right) temperature measurement sensors mounted on the rear-side of the glass-glass module of the BIPVT modules.

monitoring at the module level. This enormous number of sensors is integrated using a CAN field bus system and processed with the embedded industrial controller. In addition, two temperature sensors

are mounted in the same configuration on the backside of the reference PV modules on the bottom left and top right. In contrast, the RTDs are used for measurements such as the outlet air temperature of the BIPVT system, the in- and outlet air temperatures of the ASHP as well as the water flow & return of the cooling coil.

The RH is measured in the rear ventilation air duct of 8 modules in the center of the system, as shown in Fig. A.3 (Appendix A).

The outlet air flow rate of the BIPVT system is measured by an orifice plate sensor on the suction side of the fan. The minimum distances of 0.5 m to the fan and to pipe bends are taken into account in accordance with the manufacturers specifications. These distances ensure an approximately laminar air flow and thus accurate measurements of the flow velocity. The mass flow is calculated by the diameter of the pipe and the volumetric mass density of air according to (2.15). The density of air is calculated from measurement data of absolute pressure, RH and temperature in the air duct system.

5.1.1.3   Uncertainty of the measurement devices

The uncertainties of the measurement devices are listed in Table 5.2. The irradiance and volume flow rate devices are initially calibrated by the manufacturer according to international standards. However, the volume flow rate sensor shows a large uncertainty budget with $\pm 7.5\%$ of the measurement value at part load operation. The full load during calibration of the sensor is reported in the calibration certificate as $\dot{V} = 719.73 \ \mathrm{m^3 \cdot h^{-1}}$ and is about twice the volume flow in the air duct system during the test series. The maximum volume flow rate of the ASHP is rated with $\dot{V} = 400 \ \mathrm{m^3 \cdot h^{-1}}$. Accordingly, the measurement uncertainty of the volume flow rate must be considered with $\pm 7.5\%$. The measurement uncertainty of the setup is in accordance with the IEC 61724 [139] standard.

Table 5.2 Measurement uncertainties of used devices in the field setup.

Measurement device	Measurement value (m.v.)	Measurement uncertainty
Pyranometer (CMP11)	G_i, G_d	$\pm 1.6\%$ (calibr.)
Pyrheliometer (MS-57)	G_b	$\pm 0.63\%$ (calibr.)
Reference cell (Si-mV-85-Pt100-4L)	G_i	$\pm 1.58\%$ (calibr.)
Thermistor (NTC)	T_m, T_f	$\pm 0.3°C$ ($-10 \leq$ m.v. $\leq 50°C$)
		$\pm 0.5°C$ (m.v. $\geq 75°C$)
RTD (PT100)	T_o, T_i	$\pm 0.15°C$
Relative Humidity (HM1500LF)	RH	$\pm 2\%$ @ 55% RH
Orifice plate sensor (EZ55 C160F)	$\dot{V}$	$\pm 3\%$ Fullload (calibr.)
		$\pm 7.5\%$ Partload (calibr.)
All-in-one weather station	T_a, v_w,	$\pm 0.5°C$, $0.3 \text{ m} \cdot \text{s}^{-1}$
(US NHTFB)	p_a, RH_a	± 0.25 hPa, $\pm 3\%$
Anemometer (4.3519.00.x00)	$v_{i,w}$	$\pm 3\%$

5.1.2 Experimental test series

In order to analyze the performance of the optimized BIPVT system, various test series are conducted on the test and reference roofs. The recorded data is used to calculate the i) PR for the experimental and reference system, ii) yield increase due to active rear-ventilation, iii) maximum thermal performance of the BIPVT system, vi) increase of the COP of the ASHP in the test roof compared to the reference roof and v) determination of the maximum operation and stagnation temperature. The following list provides an overview of the experimental test series performed, the operation of the rear ventilation system and the objectives of the study:

- Test series #1: Performance Ratio - Analysis of the PR for 14 months without considering the particular experimental series and mode of operation of the rear-ventilation system. Comparison of the electrical performance of the BIPVT system with the reference PV system mounted on an open-rack.

- Test series #2: Yield increase by active rear-ventilation - Analysis of the electrical performance of the BIPVT system at high ambient temperatures and solar irradiance in summer months with and without active rear-ventilation

- Test series #3: Thermal performance - Operation of the rear ventilation system under full operation (V=350 $\text{m}^3 \cdot \text{h}^{-1}$) using a bypass (heat pump switched off, ventilation flap 1 & 2 open, Fig. 5.4). Outdoor testing of the maximum thermal performance according to ISO 9806 (Thermal solar collectors - Test method)

- Test series #4: Increase of the COP - Calculation of the increase in COP of the ASHP connected to the rear-ventilation of the BIPVT system (ventilation flap 1 closed, ventilation flap 2 open, Fig. 5.4).

The detailed methodical procedure and measurement concepts for the individual test series are described in the following subsections.

5.1.2.1 Test series #1: Performance ratio

Test series #1 is based on the calculation of the PR and temperature-corrected PR_{STC} for the BIPVT and reference system over a time period of 10 months in the thesis of Von Holst (2023) [147]. In [147] the data pre-processing, PR calculation and reporting are done in accordance with the IEC 61724-1 standard. In this work, the time period is extended to one year and two months, from March 2022 until April 2023. The performance of a PV system under real operating conditions is affected by electrical-, temperature- and optical losses. The PR considers these effects in terms of rated power at STC (25°C, 1000 $W \cdot m^{-2}$, AM1.5g). In the IEC standard [139], the PR is defined as the quotient of the final measured AC yield Y_f of the system and its AC reference yield Y_r at STC:

$$PR = \frac{Y_f}{Y_r} = \frac{\sum_k P_{el,k} \cdot t_k}{\sum_k \frac{P_0 \cdot G_{i,k} \cdot t_k}{G_{i,STC}}} \tag{5.1}$$

The AC power output $P_{el,k}$ used for the calculation is provided by the inverter manufacturer in 15-minute average values and therefore defines the time interval t. The solar irradiance data $G_{i,k}$ used for PR calculation are each measured by identical c-Si irradiance sensors in the POA of the respective PV system. Furthermore, P_0 represents the rated power output of the PV system at STC and $G_{i,stc}$ the corresponding solar irradiance. However, the performance of PV modules is strongly dependent on the operating temperature and therefore the impact on the PR is non-negligible. Consequently, the climatic conditions of the location of the PV system influences the PR [148]. In order to analyze the system performance without temperature influence, the PR_{STC} is introduced in [139]. The PR_{STC} is calculated by means of a temperature correction factor $c_{k,25°C}$ and is used to normalize the performance of the system under investigation to STC. This factor is based on the PV module temperature coefficient γ and is calculated according to:

$$c_{k,25°C} = 1 + \gamma \cdot (T_{m,k} - 25°C) \tag{5.2}$$

The PR_{STC} is determined with $c_{k,25°C}$ by:

$$PR_{STC} = \frac{Y_f}{Y_{r,25°C}} = \frac{\sum_k P_{el,k} \cdot t_k}{\sum_k \frac{c_{k,25°C} \cdot P_0 \cdot G_{i,k} \cdot t_k}{G_{i,STC}}} \tag{5.3}$$

5.1.2.2 Test series #2: Yield increase by active rear-ventilation

The second test series is done in the summer season and based on the operation of the system without a tube fan and ASHP in the test roof. The PR and the T_m are compared with times active and passive rear ventilation to the reference system. In addition, a total of four BIPVT vertical module air ducts, two on the left and two on the right edge side of the test roof, are not connected to the air duct system in the ridge. This allows a simultaneous comparison of the T_m of active and passive rear ventilation operations. However, the edges of the test roof are more exposed to the wind and therefore the T_m of the modules with passive rear ventilation is more affected by the wind compared to the modules in the center of the roof.

5.1.2.3 Test series #3: Thermal performance

A schematic representation of the air duct system configuration for test series #3 is shown in Fig. 5.4. The third test series is used to determine the maximum thermal performance of the BIPVT system as a solar thermal collector. The test conditions correspond to steady-state operating conditions according to ISO 9806:2017 [94]. Therefore, the measurements are only valid for days with approximately steady-state conditions within the range defined in the standard. Measurement data of air outlet temperature, ambient temperature, mass flow, wind speed and solar irradiance on the test roof are recorded to calculate the thermal efficiency and monitor the test conditions. The thermal efficiency is calculated by (2.18) for the active rear ventilated gross area A_g of the system with 144 BIPVT modules and the ridge construction ($A_g = 15.6m^2$). The gross area includes the aluminum frame of the module as well as the aluminum ridge construction of the test roof (Columns C-N, see Fig. A.1). This test is typically done within the harmonized Solar Keymark Network certification for different mass flow rates, the rated mass flow rate $\dot{m}$ specified by the manufacturer and $\frac{\dot{m}}{2}$. The procedure is typically done indoors under controlled environmental conditions and at collector level. According to the standard, several solar air collectors can be connected in series for the performance tests. It is also important to emphasize that testing of hybrid systems is not included.

5.1.2.4 Test series #4: Increase of the coefficient of performance

Test series #4 is based on the comparison of an ASHP coupled to a BIPVT system with a conventional system fed by ambient air. A schematic representation of the air duct system configuration for test series #4 is shown in Fig. 5.4. These systems are also known as SAHP systems. The SAHP is supplied by the preheated air of the solar air collector system and thus the COP can be increased. Previous comprehensive reviews on SAHP systems for heating purposes in [140, 141] revealed that studies about experimental studies of ASHP coupled to solar air heaters are sparse in the literature. In this work, an experimental study of these systems incorporating BIPVT modules is presented. The experimental test series is performed with a variable-speed type ASHP (aroSTOR VWL B 200/5, Vaillant) for domestic hot water (DHW) generation in the spring, fall and winter seasons during the

daytime. The test procedure is based on driving the amount of heat of the 200-liter hot water tank from a variable lower mean temperature reservoir to a defined temperature reservoir of 60°C. The output and input of the storage tank are connected by a pipe and a pump with an ambient air-based cooling coil to lower the water temperature. Different starting times of the day are defined when the heat pump starts operation. The operation stops when the threshold of 60°C is reached. The water temperature in the storage tank at the beginning and end of operation is used to calculate the heat energy $Q_{th,e}$ provided by the ASHP. The heat energy in the hot reservoir is calculated as

$$Q_{th,e} = m \cdot c_p \cdot (T_e - T_s),$$ (5.4)

where m is the mass of the water, c_p is the specific heat capacity, T_e is the temperature at the end and T_s is the temperature at the start of the test. The corresponding temperatures, the electrical energy consumption $E_{i,el}$ of the ASHP in both systems and the variable-speed fan are measured and recorded to determine the corresponding COP. The COP is defined as

$$COP_i = \frac{Q_{i,th,e}}{E_{i,el}}.$$ (5.5)

The relative increase of the SAHP in the COP compared to the reference system is expressed as

$$\Delta COP = \frac{COP_{SAHP}}{COP_{ref}} - 1.$$ (5.6)

Finally, the relative increase in the COP ΔCOP is calculated from the measurement data and correlated with environmental conditions.

5.1.2.5 Test series #5: Determination of the maximum operation and stagnation temperature

The maximum module and air outlet temperatures are relevant indicators for the durability and usability of BIPVT systems. On the one hand, module temperatures > 70° can cause deterioration, and overheating protection is therefore a relevant BIPVT research topic, as described in [11]. On the other hand, a high air outlet temperature is important for thermal usability. The measurement data of 34 module (Fig.A.1) and 62 air outlet (Fig.A.2) temperature sensors are analyzed over the period of one year. The module temperature data is filtered for maximum values from April to September. In contrast, the fluid module data is filtered for maximum values over a one-year period. The values are evaluated both as individual values and as averaged values of all sensors of the same type.

5.1.3 Results and discussion

5.1.3.1 Test series #1: Performance ratio

The results of the measured data (Table B.2) of the experimental comparison of the electrical performance from test series #1 are shown in Fig. 5.7. The average PR shows values of $86\%_{PR}$ and $88\%_{PR}$
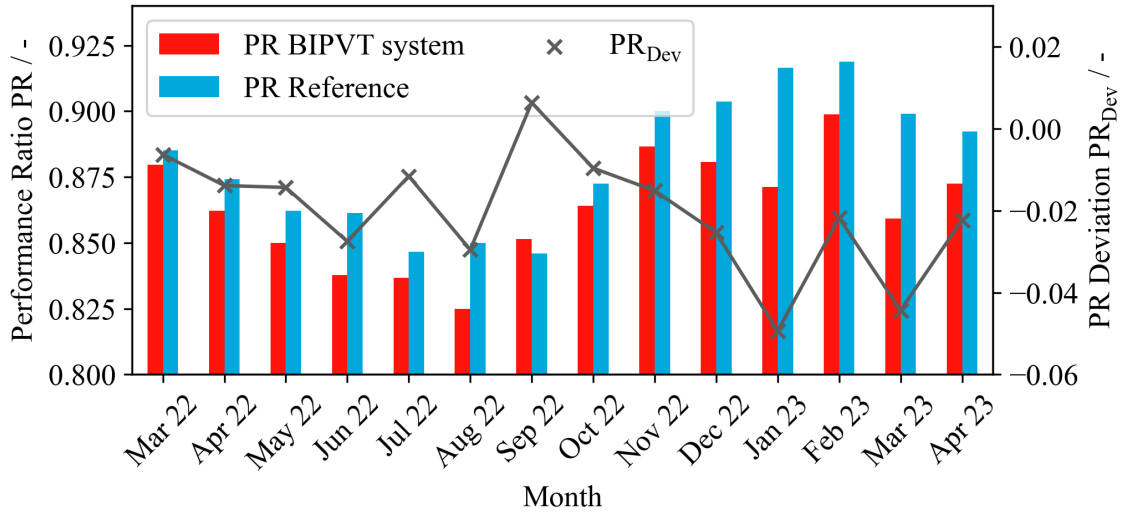
Fig. 5.7 Comparison of the measured Performance Ratio (PR) of the test roof with BIPVT modules and the reference system over 14 months. The energy consumption of the additional fan is not considered in the energy balance.

for the BIPVT system and the reference PV system, respectively, for a measurement period of 14 months. While the values are lower in summer, they are higher in winter, which is typical for northern temperate climate conditions. Recently published studies on the performance of BIPV systems under real operating conditions in [149, 150] showed an annual average PR between $74\%_{PR}$ and $78\%_{PR}$. Accordingly, the BIPVT system under investigation can increase the relative electrical performance by up to $16\%_{rel}$. However, the results are limited to varying operating conditions of the rear ventilation system due to the test series performed. The PR must be analyzed within specific time periods with constant and realistic operating conditions of the rear ventilation system to justify the significance of the results. Nevertheless, the PR comparison shows an improvement of the optimized BIPVT system compared to the state-of-the-art.

Fig. 5.8 shows the PR_{STC} of the BIPVT and reference PV system for the same data set. Although the PR_{STC} values vary significantly for four months, the mean value for both systems is $88\%_{PR}$. The average results of PR_{STC} indicate that the remaining losses, such as cable, inverter and mismatch losses, of both systems are in a similar range, although the monthly values vary. Therefore, the PR can be used to evaluate the performance of the improved BIPVT system in comparison to the standard PV system.
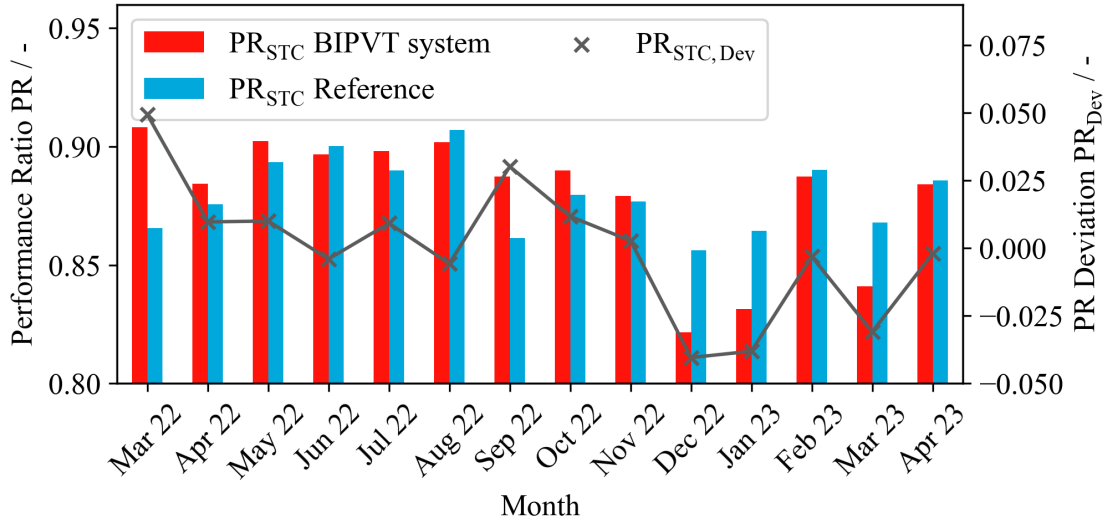
Fig. 5.8 Comparison of the measured temperature-corrected Performance Ratio (PR_{STC}) of a BIPVT test system and reference system over 14 months. The energy consumption of the additional fan is not considered in the energy balance.

5.1.3.2 Test series #2: Yield increase by active cooling

Evaluation of the data on the yield increase due to active cooling of the BIPVT module from test series #2 is done for various days in the summer of 2022. Only data from the period after optimization of the air duct system in the ridge is evaluated. All measured data for the calculation of the PR are filtered according to the solar irradiance on the respective inclined plane ($G_i > 50$ W$\cdot$m^{-2}). The evaluation of the PR from the cooled BIPVT module results in an average absolute difference of $2\%_{PR}$ over a period of 16 days. The average ambient temperature during this period is 25°C. For comparison, the average absolute difference in PR of the BIPVT module with passive cooling is also $2\%_{abs}$ for a period of 13 days at an average ambient temperature of 24°C.

From the results of the analysis, it can be concluded that no significant increase in yield can be expected from active rear ventilation of the BIPVT modules. This statement can be confirmed by analyzing the module temperature data of the passive rear ventilated modules (Columns A-B & O-P, see Fig. A.1) in comparison to the active rear ventilated modules (Columns C-N, see Fig. A.1). It can be observed that the average T_m of the actively or passively cooled BIPVT module in two analyzed periods in June (18 days) and August (6 days) is between 41°C and 53°C, respectively. This applies for all values $G_i > 200$ W$\cdot$m^{-2}. When considering the same periods for irradiation values $G_i > 800$ W$\cdot$m^{-2}, similar temperature differences result, but with a higher absolute T_m between 52°C and 62°C, respectively. The averaged temperature differences of the actively or passively rear ventilated BIPVT system are partly within the accuracy range of the temperature sensors used for the evaluation (Table 5.2). Therefore, the T_m is almost identical for both rear ventilation operation modes, taking the

measurement uncertainties into account. This analysis confirms the results presented previously for evaluating the PR in terms of yield enhancement due to active rear ventilation. According to these observations, no additional module temperature reduction and thus electrical yield increase can be expected from active rear ventilation with the considered design of the air duct system. Nevertheless, it should be mentioned that the design of the BIPVT module with integrated rear ventilation air duct already results in passive rear ventilation and thus in a reduction of the T_m. Overall, the comparison with PR evaluations of BIPV systems from the literature shows an improved PR of the BIPVT module. The average module temperature difference between the passively rear ventilated BIPVT system and the reference PV system for the same time periods in June and August ($G_i > 200 \text{ W} \cdot \text{m}^{-2}$) is only 5°C and 7°C, respectively.

5.1.3.3   Test series #3: Thermal performance

Field monitoring data from the BIPVT test system over three days in February is used to calculate the maximum thermal efficiency. This is done according to the steady-state field operating conditions defined in the ISO 9806:2017 [94] standard for solar thermal air collectors. Therefore, a 25-minute interval is filtered at the same time each day with approximately steady-state conditions. Table 5.3 shows the test conditions and corresponding results. The results show a maximum thermal efficiency of 12% for the active rear ventilated gross area A_g of 15.6 m² of the BIPVT system. Fig. 5.9 shows

Table 5.3 Mean values of the measured test conditions and results.

Test details					
Date		2023-02-08; 2023-02-14; 2023-02-15			
Time		12:15:00 - 12:40:00 UTC+1 (30 minutes)			
Type		Hybrid air collector			
Test conditions					
Description	**Symbol**	**Unit**	**Average Values**		
Solar irradiance	G_i	$\text{W} \cdot \text{m}^{-2}$	867.9	878.4	853.8
Ambient temperature	T_a	°C	5.6	10.3	8.1
Wind speed	v_w	$\text{m} \cdot \text{s}^{-1}$	3.3	2.8	2.73
Mass flow rate	$\dot{m}$	$\text{kg} \cdot \text{h}^{-1}$	401.1	458.6	232.04
Outlet temperature	T_o	$\text{W} \cdot \text{m}^{-2}$	18.3	22.5	21.9
Thermal efficiency	η_{th}	–	0.109	0.117	0.069
Electrical efficiency (DC)	η_{el}	–	0.144	0.139	0.139

the measured thermal efficiency of the BIPVT system under steady-state operating conditions in the field. The measurement data has been recorded at 20-second intervals. These measurements are shown for different constant mass flow rates in the rear ventilation system. In addition, the average

values and a regression line of the average values are shown. The average thermal efficiency increases almost proportionally with the mass flow rate. Furthermore, the values show a different spread within the respective measurement periods. The thermal efficiency shows a strong dependency on the mass flow rate. Likewise, the wind speed shows a correlation with the spread of the measurements within a measurement period.
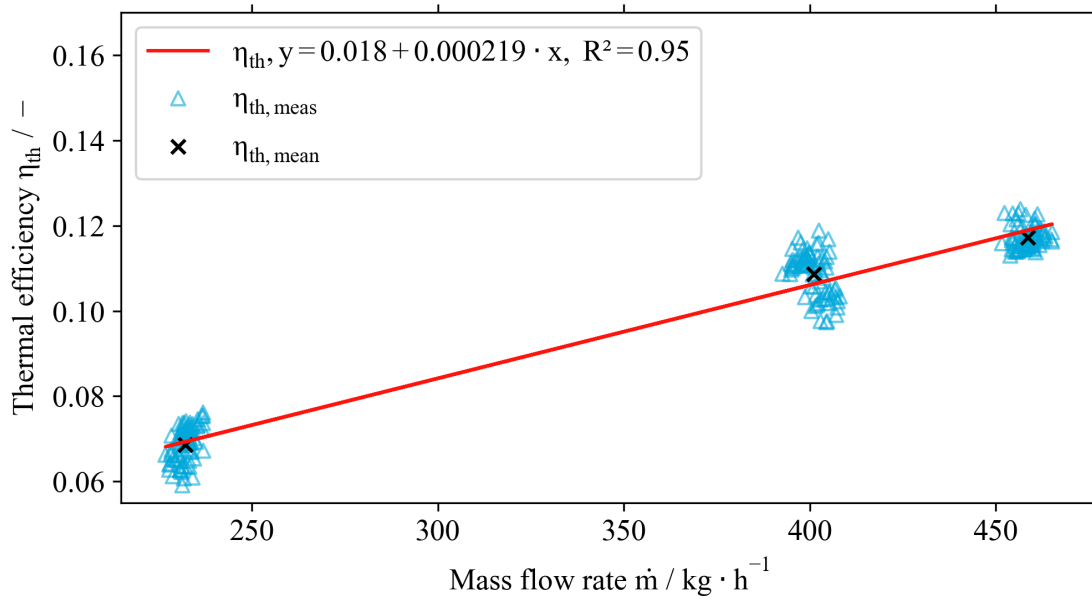
Fig. 5.9 Thermal efficiency of the BIPVT system for three different mass flow rate. The efficiency is measured in an experimental outdoor test facility at the TH Köln.

5.1.3.4   Test series #4: Increase of the coefficient of performance

The relative increase in the coefficient of performance ΔCOP is measured in test series #4 on a daily basis for a steady-state temperature increase of a hot water storage tank (Table B.1). Fig. 5.10 shows the measured monthly average COP of a SAHP and reference system over 10 months. Moreover, the average increase in COP is shown. The evaluation of the test series is done in total for 119 days in the spring, fall and winter seasons since the maximum air flow temperature of the heat pump (45°C) was already reached in May. Accordingly, test days in summer season are not available. While the ventilation system in the test series was operated with a speed-controlled auxiliary fan for 85 days from March 2022 to February 2023, it was correspondingly operated without it for 38 days in March and April 2023. The results show an average ΔCOP of 21%$_{rel}$ for 16 days in the spring and 17%$_{rel}$ for 37 days in the fall season. In December, an average ΔCOP of 8%$_{rel}$ is measured over 10 days. The maximum daily GOP$_g$ values are observed at 40%$_{rel}$ in the spring, 36%$_{rel}$ in the fall, and 37%$_{rel}$ in the winter season, respectively. Overall, the average ΔCOP is observed with 20%$_{rel}$. Annotated in black are the total number of test days in each month. In addition, the test days without operation of the auxiliary fan are annotated in red.
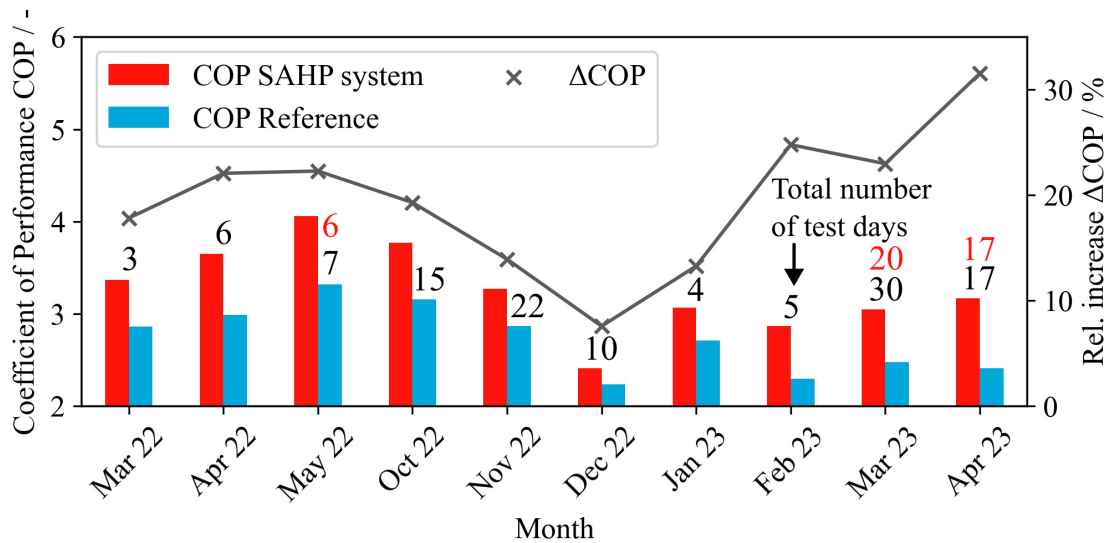
Fig. 5.10 Comparison of the measured coefficient of performance (COP) of a solar assisted heat pump (SAHP) and reference system over 10 months. The energy consumption of the additional fan is considered in the energy balance.

The test series #4 provides an initial energy estimate of the gains by using the preheated exhaust air from the BIPVT modules air duct system in a heat pump. However, the estimated gains are still limited to the operation mode during the tests for a specific environmental condition. The results does not allow final conclusions about the SPF gains of the system. The SPF is the decisive key factor in comparison to the COP to quantify the energetic performance of the SAHP under real operating

conditions. Depending on the heat pump type, the SPF includes the heat consumption for residential space heating and DHW generation. In particular, the weather conditions, the storage tank size and the residential heating demand have a great influence on the SPF. To estimate the SPF, it is determined by simulations with a simplified ASHP modeling approach presented in [151, 152].

5.1.3.5 Test series #5: Determination of the maximum operation and stagnation temperature

The maximum module temperature was observed at 74.2 °C in September. In comparison, the maximum module temperature was 70° between April to August . The maximum air outlet temperatures are observed at 52 °C in summer and 33°C in winter. Also, the temperatures during stagnation of the air in the rear ventilation system are analyzed. It shows a maximum module temperature of 70°C and an air outlet temperature of 67°C for a total of 37 days.

5.2   Numerical assessment of an optimized BIPVT system

A simulation case study is done for the BIPVT system under study, installed on a gable roof. The simulation is performed for two different locations and three different module tilt angles. The system configurations include three tilt angles with a fixed azimuth of 180° (0°=North). The objective is to assess the optimized BIPVT system by means of annual performance simulations. The performance model developed within this thesis is used for the simulation of the annual electrical and thermal yields. The model is described in Section 3.3. The simulation framework includes an optical, electrical and thermo hydraulic model as well as input for TMY weather & load profile data. The PV model is based on a standardized modeling approach according to IEC61853, whereas the thermal model is non-standardized. The thermal model is based on the dynamic simulation of a physical model component network parameterized with CFD simulation data of the BIPVT system under study. Furthermore, a hysteresis control of the rear-ventilation system with a constant mass flow rate is implemented in MATLAB-Simulink. The controller activates the fan when the threshold of $\Delta T > 1°$ is reached. The temperature difference used to control the fan is defined as $\Delta T = T_o - T_a$. In contrast, the fan is deactivated when the temperature difference ΔT equals 0°.

5.2.1   Simulation case

The simulation study is done for a single-family house with three residents in two locations: Cologne, Germany and Risø, Denmark. The simulated systems are 180° south-oriented and tilted at 30°, 45° and 60°, respectively. A total of 192 BIPVT modules are installed on a gable roof, arranged in two strings of 96 tiles each. Accordingly, the simulated systems have a total PV capacity of 2.8 kWp resulting in a PV module area of 19.6 m². The PV systems are connected to two inverters a 1.5 kW rated power input. The active rear ventilation heat recovery system is setup in a 12×12 configuration as described in Section 5.1.1. Therefore, the gross area of the BIPVT system is only 15.6 m², including the area of the ridge construction. Two series of simulations are performed considering two different

mass flow rates. First, the mass flow rate in each rear ventilation air duct is setup with $11 \, \text{kg} \cdot \text{h}^{-1}$, as this is the flow rate validated by the experimental setup in Section 5.1.1. It is important to emphasize that the airflow distribution in the collecting pipe on the ridge is neglected. Accordingly, a uniform flow distribution is assumed in this case study. Air leakage mass flow from the ambient air into the ridge construction is assumed to be a function of the total mass flow.

The study includes an approximation of the gains from the utilization of the increased air temperature by an ASHP system connected to the BIPVT system outlet. Simplified heat pump models based on performance and temperature measurements of manufacturers are presented in [151, 152]. The quadratic regression line presented in [151] is used for the modeling of the ASHP. Accordingly, the COP in this study is approximated by

$$COP_{ASHP} = 6.81 - 0.121 \cdot \Delta T + 0.000630 \cdot \Delta T^2 \; for \; 15 {\leq} \Delta T {\leq} 60°C, \tag{5.7}$$

where ΔT is the temperature difference between sink and source temperature. The sink temperature is used as a constant value and depends on the heating application. For DHW applications, a temperature of 50-60°C is recommended for comfort and hygiene reasons [153]. The source temperature is the inlet temperature of the heat pump, which can be the temperature of the ambient air or preheated air from the rear ventilation of a BIPVT system. In order to analyze the gains from the heat utilization, an ASHP connected to the BIPVT system under study and a conventional ASHP are compared. The simulated air outlet temperature of the time-series based BIPVT model and the ambient temperature of the TMY data sets are used for this comparison. The heat pump is considered as on/off modulation device. Furthermore, it is used for DHW generation and therefore rated with an electrical power input of 0.7 kW.

The SPF indicates the annual performance of a heat pump considering the provided thermal energy $E_{th,hp}$ and the respective electrical energy demand $E_{el,dem}$. Accordingly, the SPF is calculated as

$$SPF = \frac{\int E_{th,hp} \, dt}{\int E_{el,dem} \, dt} \tag{5.8}$$

and the relative increase ΔSPF as

$$\Delta SPF = \frac{SPF_{BIPVT}}{SPF_{ref}} - 1, \tag{5.9}$$

where SPF_{BIPVT} is the SPF of the BIPVT system and SPF_{ref} is the SPF of the reference system connected to the ambient air. In this thesis, the SPF is calculated according to three different methods. The SPF_{load} is calculated using a demand-controlled operation strategy, based on the DHW load profile. In contrast, the SPF_{mean} is the annual mean value of the COP and the SPF_{max} is the maximum value that can be achieved by using only operating points with increased air outlet temperature. Nevertheless, to ensure adequate operation of the heat pump, a thermal storage must be used in the heating system.

Hourly-resolved load profiles are used as input in the developed simulation framework to determine system performance indicators such as electrical solar coverage rate and self-consumption rate, as well as the SPF of the heat pump. According to [154], the electrical solar coverage rate is calculated by

$$a_{cov} = \frac{E_{PV,cov}}{E_{el,cons}},$$ (5.10)

where $E_{PV,cov}$ is the demand covered by the PV system and $E_{el,cons}$ is the total electrical energy consumption. The self-consumption rate is the ratio of solar-covered electrical energy consumption $E_{PV,cov}$ and the total energy generated by the PV system $E_{PV,total}$. Accordingly, the self-consumption rate is calculated by

$$a_{self} = \frac{E_{PV,cov}}{E_{PV,total}}.$$ (5.11)

According to [155], the electrical energy consumption of an average German household in 2021 was $2828\,\mathrm{kWh \cdot a^{-1}}$. The measurement data of the electrical load profiles for households are presented in [156]. In this thesis, load profile 6 with an electrical energy consumption excluding the heat pump and fan operation of the BIPVT system of $2938\,\mathrm{kWh \cdot a^{-1}}$ is used for the simulation study. The electri-
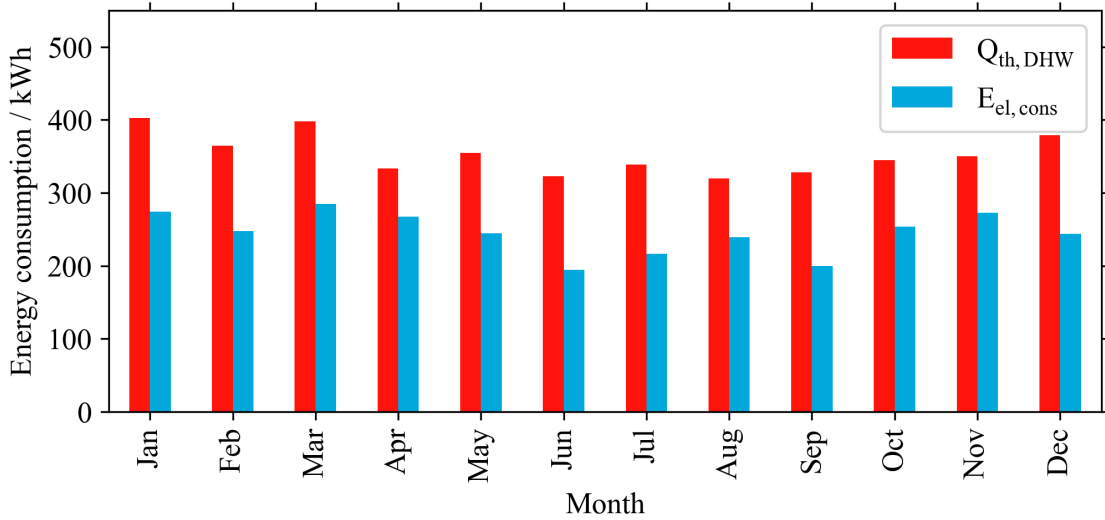
Fig. 5.11 Monthly distribution of energy consumption for domestic hot water (DHW) supply and electricity of an average single-family house in Cologne, Germany.

cal energy consumption of the heat pump and fan operation for the BIPVT system varies with changing operating conditions. Therefore, it is calculated for each individual simulation case. Then the overall electric consumption is combined in order to calculate the system performance indicators. The DHW load profile for a single-family house is generated using the DHWcalc tool presented in [157]. The

mean daily draw-off volume for three residents is considered to be 200 liters per day at a temperature difference of 50°C. The total heat demand for DHW supply in an average single-family house is thus $4238\,\mathrm{kWh\cdot a^{-1}}$. Fig. 5.11 shows the monthly distribution of the load profiles for a single-family house.

5.2.2   Locations and weather data

The weather data for this study are provided by the Photovoltaic Geographical Information System (PVGIS) of the European Commission [107]. The procedure to generate TMY files is described in the ISO15927-4 [158] standard and in [159]. The solar radiation data of the PVGIS-SARAH-2 database is used. This database is based on images of the EUMETSAT Climate Monitoring Satellite Application Facility (CM SAF) as described in [160]. The datasets are provided with hourly time resolution for given geographical locations in order to perform solar energy yield simulations. In these data sets, average ambient temperature, relative humidity, wind speed and detailed solar radiation are included. The radiation data set contains direct beam, diffuse and global horizontal irradiance.

Fig. 5.12 shows the monthly irradiated specific solar energy and averaged wind speed in Cologne, Germany. The irradiated specific solar energy is shown for the plane-of-array for a tilt angle of 30°
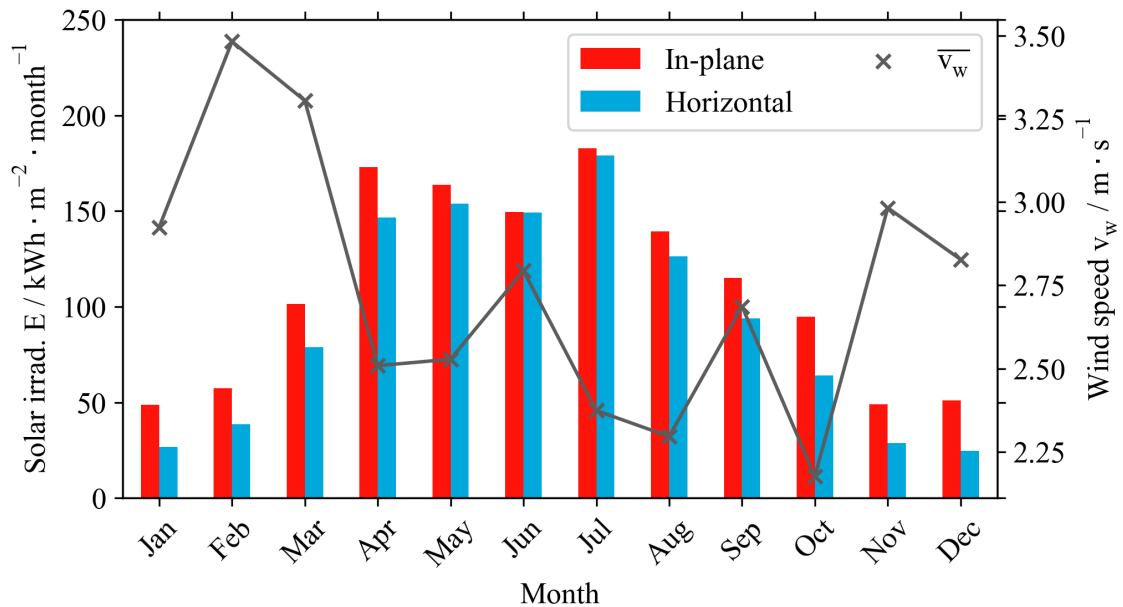
Fig. 5.12 Monthly irradiated solar energy and averaged wind speed in Cologne, Germany.

and on the horizontal surface. While in the winter, autumn and spring seasons the difference in amounts is large, the difference in the summer season is small. The average wind speed is between 2.8 and 3.4 m·s^{-1} in winter. In contrast, the wind speed is around 2.2 and 2.6 m·s^{-1} in the spring, summer and autumn seasons. Fig. 5.13 shows the TMY weather data used for the simulation study

for Risø, Denmark. The weather data sets are summarized in Table 5.4. The ambient temperature
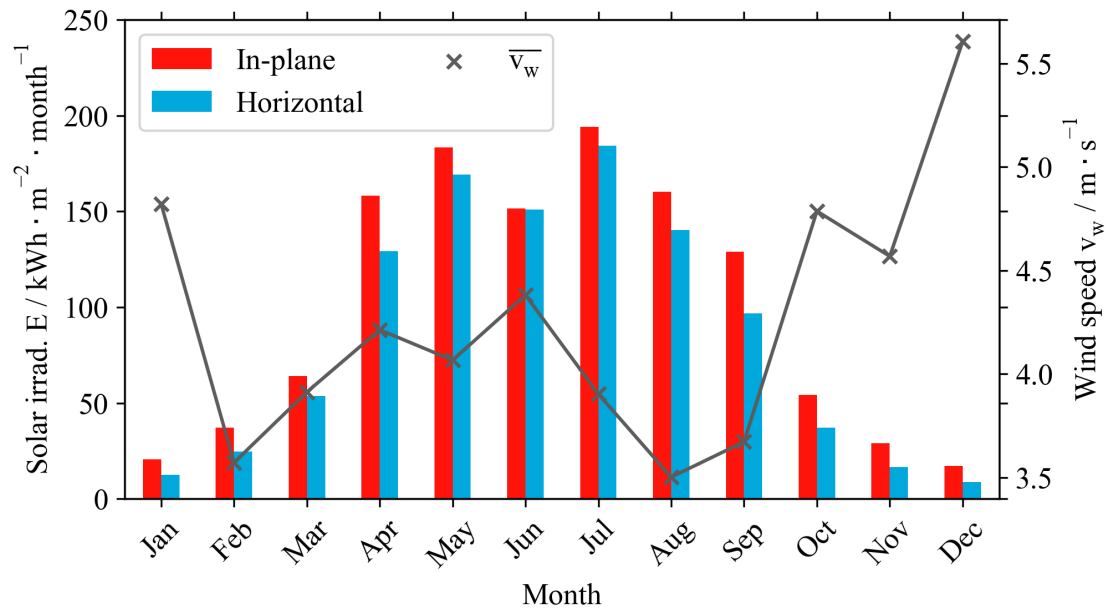
Fig. 5.13 Monthly irradiated solar energy and averaged wind speed in Risø, Denmark.

and wind speed are averaged. In contrast, solar irradiation is shown as total irradiated energy. The in-plane irradiation is shown for a tilt angle of 30°, simulated with the modeling approach described in Section 3.3.1.

Table 5.4 Typical meteorological year data used for the simulation study.

Typical meteorological year data				
Database	PVGIS-SARAH-2 [160]			
Resolution	Hourly			
Time period	2005-2020			
Parameter	**Symbol**	**Unit**	**Cologne** 50.9°N, 7.0°E	**Risø** 55.7°N, 12.1°E
Climate classification [161]			Cfb	Cfb
Global horizontal irradiation	E_h	$kWh \cdot m^{-2} \cdot a^{-1}$	1111	1025
In-plane irradiation	E_{in}	$kWh \cdot m^{-2} \cdot a^{-1}$		
180°South, β=30°			1326	1199
180°South, β=45°			1336	1200
180°South, β=60°			1278	1141
Ambient temperature	$\overline{T_a}$	°C	10.5	8.9
Wind speed	$\overline{v_w}$	$m \cdot s^{-1}$	2.7	4.3

5.2.3 Results and discussion

The results of the simulation case study are first presented for a constant mass flow rate of $\dot{m} = 11\,kg \cdot h^{-1}$ in each rear ventilation system. Subsequently, the results are presented using the optimal mass flow rate of $\dot{m} = 180\,kg \cdot h^{-1}$ as determined in Section 4.2 for the BIPVT module design under study. The fan for the operation of the rear ventilation system is hysteresis controlled based on the air outlet temperature of the BIPVT system and ambient temperature. Fig. 5.14 shows the specific electrical and thermal energy yields for Cologne, Germany, with a system surface tilt angle of 30°. The energy yields are calculated by (2.17) and the corresponding equation for electrical energy yield. The electrical energy required to operate the fan of the rear ventilation system is excluded and amounts to 141 kWh. The annual specific AC electrical energy yield is $165\,kWh \cdot m^{-2}$. In comparison, the annual specific thermal energy yield is $151\,kWh \cdot m^{-2}$. This results in an annual specific overall energy yield of the system of $302\,kWh \cdot m^{-2}$, including the energy demand of the fan. Fig. 5.15 shows the monthly average electrical and thermal energy efficiencies in Cologne. The efficiencies are calculated by (2.18) and the corresponding equation for electrical efficiency. The annual average electrical and thermal efficiency are $13\%_{abs}$ and $11\%_{abs}$, respectively. These values are obtained by neglecting the energy that has to be used for the fan. Taking this energy consumption into account, the annual average overall efficiency is $22\%_{abs}$.

Fig. 5.16 shows the simulation results with a system surface tilt angle of 30° for the site in Risø, Denmark. The annual specific electrical energy yield amounts to $151\,kWh \cdot m^{-2}$. In contrast, the annual
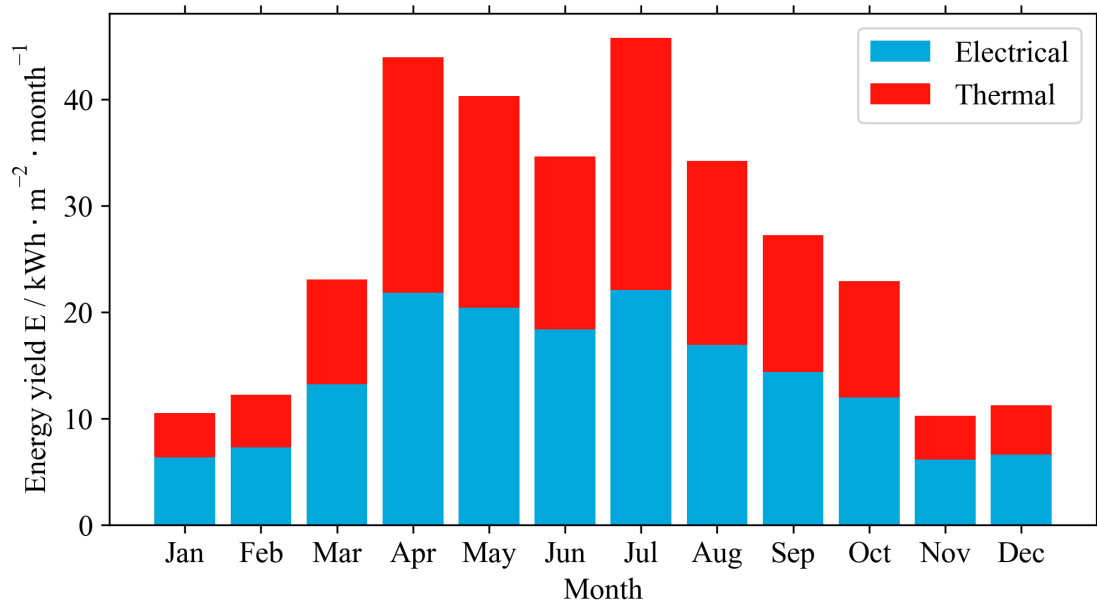
Fig. 5.14 Monthly electrical and thermal energy yield of an air-based BIPVT system with 30° module tilt angle in Cologne, Germany.
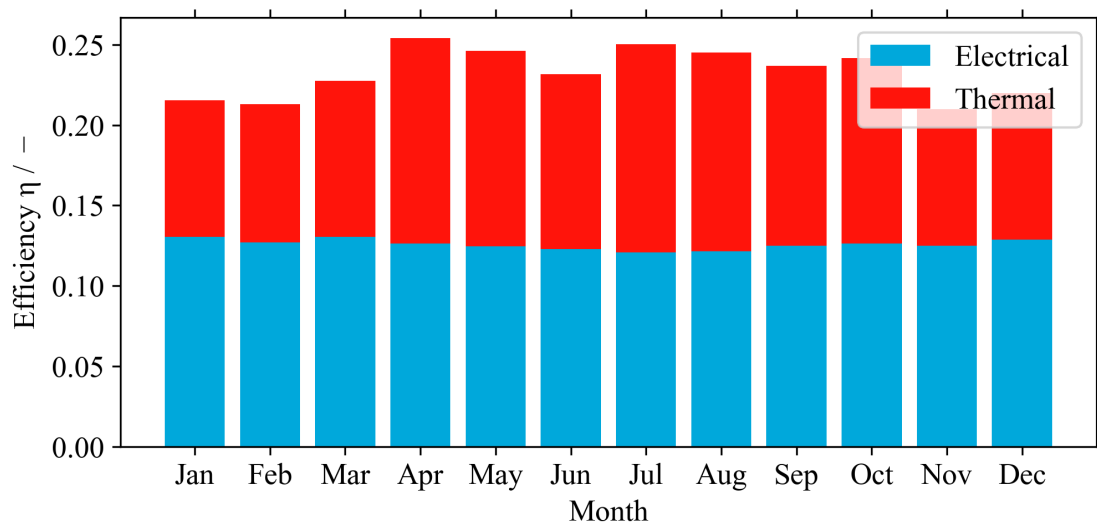
Fig. 5.15 Monthly electrical and thermal efficiency of an air-based BIPVT system with 30° module tilt angle in Cologne, Germany.
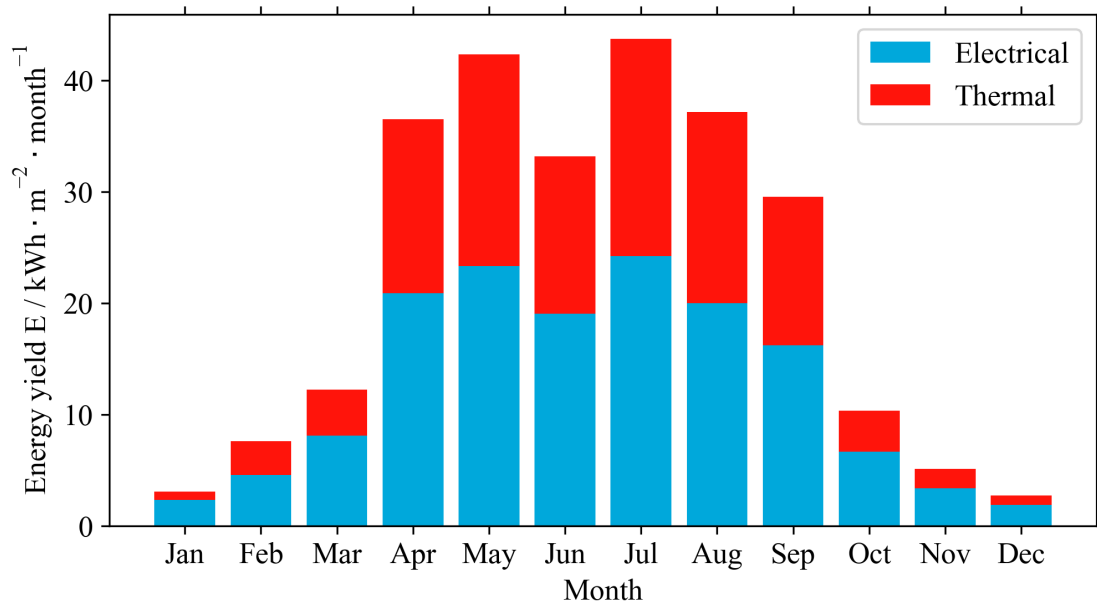
Fig. 5.16 Monthly electrical and thermal energy yield of an air-based BIPVT system with 30° module tilt angle in Risø, Denmark.

thermal energy yield is $113 \, \mathrm{kWh \cdot m^{-2}}$. The annual energy consumption of the fan to operate the rear ventilation system is not included and amounts to 123 kWh. Therefore, the overall system energy yield, including the energy demand of the fan, results in $251 \, \mathrm{kWh \cdot m^{-2}}$. The electrical efficiencies
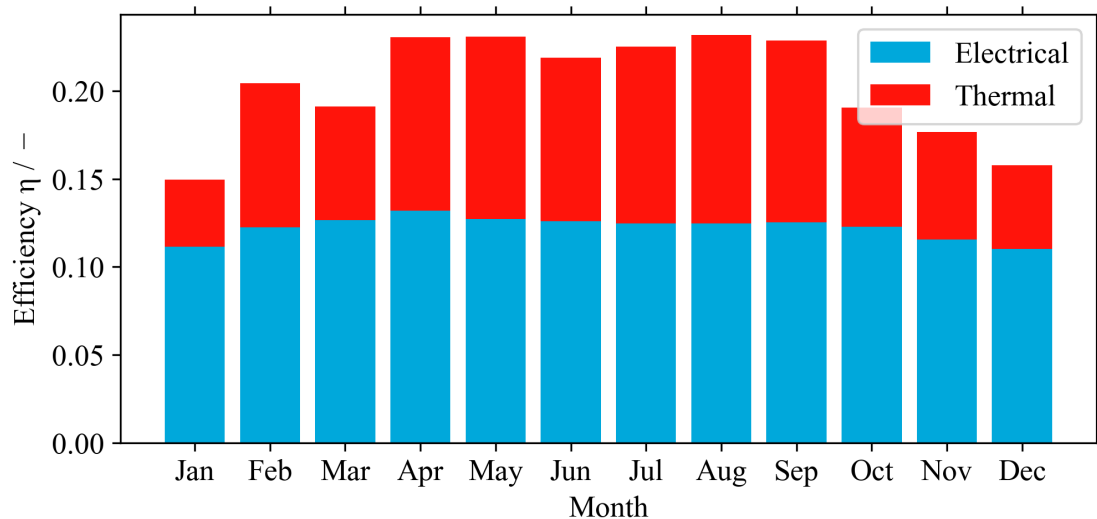
Fig. 5.17 Monthly electrical and thermal efficiency of an air-based BIPVT system with 30° module tilt angle in Risø, Denmark.

of both locations are in a similar range. The values are slightly higher in the winter months, which can be attributed to the lower ambient temperatures. However, the thermal efficiencies in Cologne vary only in a range between $8.5\%_{abs}$ in winter and $13\%_{abs}$ in summer months. In comparison, the efficiencies in Risøvary between $4\%_{abs}$ and $10.7\%_{abs}$. The higher deviation can be explained by the increased wind speed in the winter months compared to the summer months.

Table 5.5 shows the summarized results of the simulation study. The results show similar electrical performance for both locations with $12.5\%_{abs}$. The solar coverage and self-consumption rate are calculated by (5.10) and (5.11), respectively. The coverage rate has slightly decreased for the systems located in Risø. The average thermal performance of these systems shows a lower efficiency by $30\%_{rel}$ in comparison to the systems in Cologne. It is assumed that the lower efficiency is attributed to the increased wind speed at the site. Likewise, a lower overall performance by $17\%_{rel}$ in average is observed for the systems in Risø. Compared to the values in the literature [11, 14], which range between $14\%_{abs}$ and $60\%_{abs}$, the thermal efficiency can be considered low. However, a comparison is very limited because the thermal efficiency is strongly influenced by the wind speed, module design and mass flow rate in the rear ventilation system. Moreover, the results stated in the literature are presented for different experiment and simulation conditions. The annual average solar coverage rate is observed at 0.26 and 0.23 in Cologne and Risø, respectively. In contrast, the average self-consumption rate shows 0.46 for both locations. Whereas the monthly average solar coverage rate in Cologne has its maximum in August at 0.43, its minimum is 0.17 in January. In comparison, the self-consumption rate shows a maximum value of 0.82 in November, and the minimum value is observed in April with 0.6 (Fig. C.1). These system performance indicators for air-based BIPVT systems are lacking in the literature. Annual average solar coverage and self-consumption rates are stated in [162], with 0.27 and 0.68 for a water-based BIPVT system, respectively. Accordingly, the values observed in this thesis are slightly lower, which can be attributed to the more efficient water-based thermal system in the work of [162]. It is important to highlight that these results were achieved without battery storage. It can be concluded that the observed values in the simulation case study are consistent with values presented in the literature and observed in the experimental test series.

Table 5.5 Final results of the simulation study with $\dot{m} = 396 \, \text{kg} \cdot \text{h}^{-1}$.

Parameter	Symbol	Unit	Cologne 50.9°N, 7.0°E			Risø 55.7°N, 12.1°E		
System surface tilt	β	°	30	45	60	30	45	60
Electrical system								
Energy	E_{el}	$\text{kWh} \cdot \text{m}^{-2} \cdot \text{a}^{-1}$	165	167	160	151	151	143
Efficiency	η_{el}	$\%_{abs}$	12.6	12.7	12.6	12.2	12.4	12.5
Solar coverage rate	a_{cov}	-	0.26	0.26	0.24	0.23	0.23	0.22
Self-consumption rate	a_{self}	-	0.46	0.45	0.45	0.46	0.45	0.45
Thermal system								
Energy (Collected air)	Q_{th}	$\text{kWh} \cdot \text{m}^{-2} \cdot \text{a}^{-1}$	151	153	145	113	114	107
Efficiency	η_{th}	$\%_{abs}$	10.7	11.0	11.0	8.1	8.5	8.6
BIPVT system								
Fan	E_{fan}	$\text{kWh} \cdot \text{a}^{-1}$	141	138	132	123	120	114
Energy	E	$\text{kWh} \cdot \text{m}^{-2} \cdot \text{a}^{-1}$	302	313	298	257	259	244
Efficiency	η	$\%_{abs}$	22.2	23.2	23.2	19.8	20.4	20.5
SAHP system								
Rel. increase SPF_{load}	ΔSPF	$\%_{rel}$	5.2	5.3	5.1	4.0	4.0	3.7
Rel. increase SPF_{mean}	ΔSPF	$\%_{rel}$	6.9	7.0	6.5	5.2	5.2	4.9
Rel. increase SPF_{max}	ΔSPF	$\%_{rel}$	20.1	20.7	20.3	16.8	17.2	16.9

Chapter 6

Conclusion and outlook

The conclusions of this thesis are first separated by each research topic with the respective objectives and then summarized in a general conclusion and outlook.

6.1 Conclusion on the modeling and analysis of BIPVT modules

A BIPVT simulation framework based on measured and simulated modeling parameters has been developed. The experimental approach is based on small-scale optical measurements in the laboratory. In contrast, the numerical approach includes electrical, optical and thermal simulations. The findings related to the first research question, how the improved BIPVT module can be modeled, are summarized in the following:

First of all, an automated rotational sample stage for angular-dependent optical characterization has been developed for experimental measurements. The sample stage shows an angular adjustment accuracy $\leq 1°$ and thus allows very precise angular-dependent measurements according to the standard IEC61853-2. Therefore, the experimental approach is suitable to derive optical design parameters for the simulation models. The numerical approach to derive modeling parameters includes steady-state CFD simulations. These simulations are done to determine parameters such as the respective convective heat transfer coefficients to the fluid, air leakage mass flow rates, and pressure drop for the development of a thermo hydraulic model. Finally, a time-series simulation framework based on these design parameters is developed to analyze and assess the electrical and thermal performance under real operating conditions of the improved BIPVT system.

The consistency of the thermal parameters is justified by a comparison of the simulation results between the CFD and the thermo hyraulic model for the air temperature in the rear ventilation system. Four models to determine the convective heat transfer coefficient are set up. The lowest RMSE of 0.22°C is observed for a model using the fluid temperature as a function of the mass-weighted average in the total air duct volume and the module surface temperature as a function of the area-weighted average on the bottom of the glass package.

The simulation framework is validated by field measurements over 59 days in an experimental field

test. The model shows good agreement with the measurement data. The DC electrical energy yield shows a relative ΔMBE of -0.8%, whereas the thermal energy of the collected air shows a ΔMBE of 0.8%. In conclusion, the applied experimental and numerical modeling approach is suitable for the analysis of outdoor performance and the optimization potential of a custom BIPVT module design. These findings contribute to a more precise planning of system concepts, such as effective heat utilization, and to the estimation of optimization potentials. However, several simplifications and assumptions have been made, so verification for various module and system designs remains. These simplifications include air leakage caused by the connection to the ridge structure, which is difficult to quantify. The ridge construction is simplified with a constant factor as a function of the mass flow rate, and therefore the results are limited. Accordingly, it is recommended to consider the ridge construction in more detail.

Future research should expand the simulation framework to include a suitable thermal building model with thermal storage and heating load profiles. These extensions can help calculate usable energy for heating and the economics of such systems. Another point to consider is that the thermal modeling parameters are based on simulations. Experimental measurements of these parameters are therefore recommended to further improve the predictive accuracy of the model.

The second research question in this area was how to accurately simulate the AOI performance of colored modules. Therefore, the short-circuit current of PV single-cell laminates has been simulated with different colored glass covers using experimental ASR and spectral irradiance measurement data. Moreover, field validation is done for 25 days of measurement on a south-oriented rack under a tilted angle of 42° in Risø, Denmark (55.7° N). In addition, simulations were performed with a less elaborate measurement procedure using SR measurements at normal incidence, and broadband IAM was performed to account for AOI reflection losses.

The simulations show good agreement with field measurements. A statistical error analysis reveals a relative ΔRMSE ranges between 1.9% and 2.5% for simulations using ASR and between 1.7% and 3.0% using broadband IAM model approach. The absolute mean differences of the presented ASR modeling approach consistently show lower differences for samples with non-uniform decreasing EQE (blue, blue-green, gold) with increasing AOI. To justify the alternate methodology, the 95% confidence interval of the mean absolute differences is evaluated. It shows that the lower differences of the ASR model approach for the colored samples are statistically significant. In contrast, the broadband IAM approach shows significantly lower mean absolute differences for samples with neutral EQE (grey, control). Nevertheless, the absolute error differences are very small, and comparability is limited due to the larger dependency of the broadband IAM modeling approach on the IAM model applied. Finally, it can be concluded that simulations using ASR measurement data have the most value in colored BIPV applications. Nonetheless, both presented model approaches show improved prediction accuracy compared to simulation studies on the outdoor performance of BIPV modules found in the literature. However, it is important to emphasize that the findings of this thesis are limited to colored glasses with a thin-film multi-layer interference coating on the inner surface and a structured outer surface.

The application of spectral measurement data provides accuracy suitable for energy yield estimates of BIPV applications. In particular, the ASR model approach helps to predict accurate energy yields of colored BIPV systems for a wide range of operating conditions. This contributes to better planning of investments in BIPV installations with custom design options.

In subsequent research, the simulations should be done for various locations with different prevailing solar spectra distributions to compare the findings presented here. Beyond an angular resolved modeling approach can also be applied to the diffuse irradiance component to improve simulation accuracy.

6.2   Conclusion on the optimization of BIPVT modules

The optical and thermal optimization potential of BIPVT module performance has been quantified to answer the following research question:

How do the optimizations impact the module performance?

The impact of different nano-imprinted textured front covers on the annual angular-dependent optical losses was investigated. Therefore, the effective irradiance has been simulated for different locations and module tilt angles. In order to determine the relative annual increase in effective irradiance, each textured sample is compared with an identical non-textured sample. The relative transmittance of PV single-cell test samples has been measured using a rotational sample stage and a sun simulator to derive modeling parameters. The study includes two different rolled-texture glasses available on the market to compare the results. In order to identify the exact input parameters for the annual simulation, a suitable model for the relative transmittance must be qualified by a comparison. However, a poor agreement was observed, and therefore the relative transmittance curves are linearly interpolated. The results for the nano-imprinted textures show a relative increase between 2% and 2.2% for Cologne, Germany. In comparison to the rolled textured samples, a relative increase of 2.4% was observed.

It can be concluded that the nano-imprinted textures contribute to a reduction in angle-dependent optical losses, which is particularly relevant for building-integrated systems with suboptimal orientation. However, the results are limited by the angular-dependence of the textures, and therefore a more detailed investigation including optical parameters is recommended. A module design with nano-printed textures has the potential to reduce the LCOE, depending on the additional costs. Future work should focus on the estimation of cost efficiency and long-term outdoor testing.

The optimal operating point for the BIPVT module under investigation was determined by varying the operating mass flow rate and air leakage. Therefore, a wide range of steady-state operation points was simulated using the validated BIPVT model. In order to find an optimal operating point for the particular design, the effective thermal efficiency is calculated. The effective efficiency is taking into account the energy consumption of the fan used to operate the rear ventilation system. The results show maximum effective efficiencies of 21.5% for an airtight system and 24.3% for a system with air

leakage in between the modules. The optimal operating point with an effective thermal efficiency of 24.3% has been observed at a mass flow rate of $180 \, \text{kg} \cdot \text{h}^{-1}$ for a single air duct system consisting of 12 modules connected in series. It can be stated that the efficiency of the investigated BIPVT system can be increased up to 24% at an optimal mass flow rate. In addition, leakages of the air duct lead to a higher effective efficiency and therefore overall energy yield. However, the results are limited to an airtight connection to the manifold pipe in the ridge construction.

6.3 Conclusion on the assessment of BIPVT systems

The third research objective is to assess the electrical and thermal performance of the optimized BIPVT system under real operating conditions. Therefore, the annual energy yields and efficiencies of the improved BIPVT module arranged in a system have been measured and simulated.

A BIPVT system is set up in an experimental large-scale field test in Cologne, Germany. The average PR has been calculated for a total period of 14 months and shows $86\%_{\text{PR}}$ and $88\%_{\text{PR,STC}}$. A comparison with recent studies of roof-integrated BIPV systems reveals a relative increase of up to $16\%_{\text{rel}}$. Therefore, it can be stated that the BIPVT system under study shows a significant increase in electrical energy yield in comparison to non-ventilated BIPV. However, the module temperature analysis and PR calculation regarding the reduction of the PV cell temperature show no significant difference between active and passive rear ventilation. Accordingly, the BIPVT system shows considerable passive rear ventilation functionality. In the literature, 70°C is stated as the critical temperature threshold for the deterioration of PV modules. The maximum module temperature was observed at 74°C. This indicates that the system without active rear ventilation has operating temperatures that are only slightly above this temperature threshold. Therefore, it can be stated that slightly improved thermal management can achieve acceptable overheating protection through passive rear ventilation. Nonetheless, results are limited to different operating conditions during the measurement series. Accordingly, a comparison with a test series under more realistic operating conditions is recommended.

The thermal performance of the collected air is measured under steady-state outdoor conditions according to solar air heater testing standards. The maximum thermal efficiency was observed at 12%, while the rear ventilation system with 12 parallel rear ventilation air ducts was operated at $400 \, \text{kg} \cdot \text{h}^{-1}$. It shows that BIPVT modules have the potential to increase the overall efficiency of residential solar systems. However, the results are limited to the outdoor conditions during the test. In addition, fan power is not included in the maximum thermal efficiency because it is not specified by the standard. Moreover, an ASHP on the test roof has been connected to the air outlet of the BIPVT system. For comparison, a reference ASHP is connected to ambient air. The relative increase in the COP between these heat pumps was calculated for 119 days over 10 months of measurement data. An average relative increase of $20\%_{\text{rel}}$ in COP was observed. In conclusion, a significant gain can be expected when the preheated air of a BIPVT system is used as an inlet for an ASHP. However, the results are limited to a test roof without a realistic heat demand profile. It is important to consider a thermal storage system for load shifting to take advantage of these gains.

A case study with the developed simulation framework has been performed to assess the annual performance of the improved BIPVT modules. The study includes annual simulations in hourly resolution at two different locations and in three different orientations. TMY data and electrical energy load profiles, as well as DHW generation load profiles for a single-family house, were used as input for the time-series simulation. Maximum electrical, thermal and overall efficiencies of 12.7%, 11%, 23.2% have been observed, respectively. The performance indicators, solar coverage and self-consumption rate, were found to average 0.26 and 0.46, respectively, without battery storage. The SPF has been simulated and shows a relative increase of 7%. A maximum relative increase of 20.7% was found for heat pump operation with increased air outlet temperature. In summary, the values of the simulation and experiment are consistent. However, the results are limited by several assumptions in the simulation models. Since the performance of the system is strongly influenced by climatic conditions, it is recommended to simulate different climate zones.

6.4 General conclusions and outlook

An improved BIPVT module design has been studied using an experimental and numerical approach. It can be stated that the presented and validated simulation framework optimizes the planning and quantification of optical and thermal optimizations. Likewise, a significant contribution towards the state of the art in the simulation under real operating conditions of modules with high-transmissive colored glasses has been presented. These findings significantly contribute to quantifying performance optimization potential and the implementation of improved system designs. Likewise, a contribution is made to the performance prediction accuracy of customized modules with a colored appearance. Future work should integrate thermal building load profiles into the simulation framework and extend the BIPVT system model to include space heating and storage applications. The performance of the BIPVT module has been improved by optical and thermal optimizations. While the optical optimization potential is comparatively low and limited to angular-dependent enhancements, the thermal potential, in contrast, is large. However, the quantified potential is far from its maximum. Therefore, future work should include thermal optimizations with a focus on an improved system design considering mass flow rate, air leakage and heat utilization concepts to maximize performance. The key findings of the performance assessment can be summarized as follows: The electrical performance of the BIPVT module is above average, while the observed thermal performance is comparatively low. Nonetheless, the overall performance is improved compared to a BIPV system due to heat utilization. The results indicate that heat utilization by an ASHP can save a considerable amount of energy for residential space heating and DHW generation. In order to utilize the energy savings due to the improved SPF, an adequately sized thermal storage system for load shifting is recommended. However, the PR is influenced by the climate, and therefore these findings are limited to systems located in temperate climates. Nonetheless, the determined performance indicators of the ASHP system in the field test are very limited due to operation without realistic load profiles.

This thesis contributes to pave the way for the BIPVT technology to become a standard building component. Nonetheless, subsequent research has identified a need for improvement in order to introduce this technology into the market. Future work should consider expanding the simulation framework by building simulations to improve prediction capabilities. In addition, variations of the module design should be integrated into the simulation framework to compare their performances. A number of research questions were only briefly touched upon, and these should be further investigated in future studies. In particular, how the heat in the building can be effectively used with a heat pump or other systems.

Appendix A

Experimental measurement setup
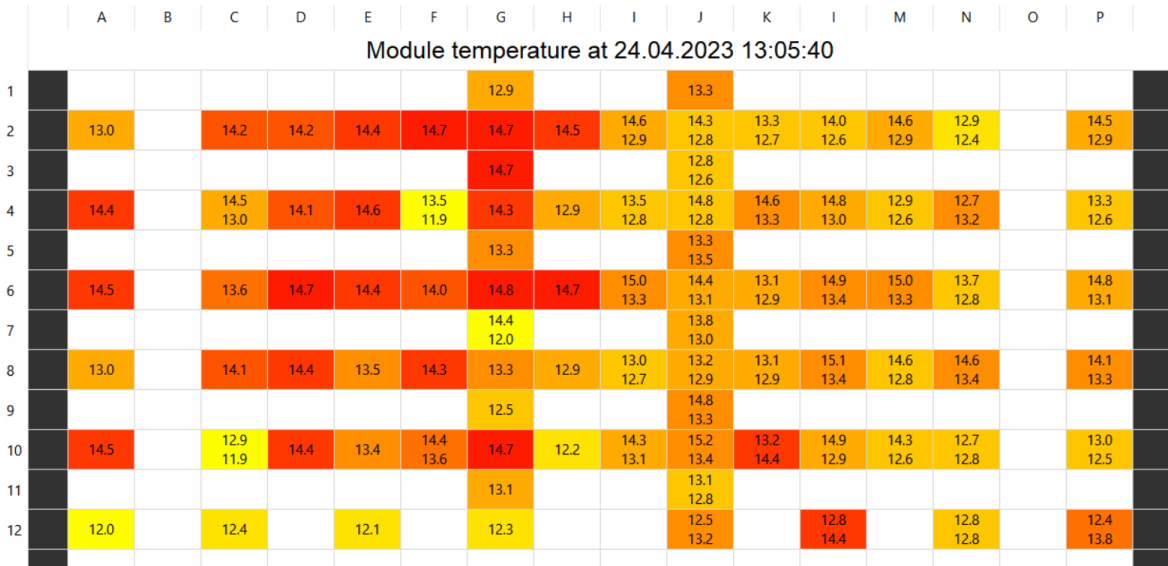
Fig. A.1 Overview of module temperature measurement sensors mounted on the backside of the building-integrated PVT modules in the test facility.
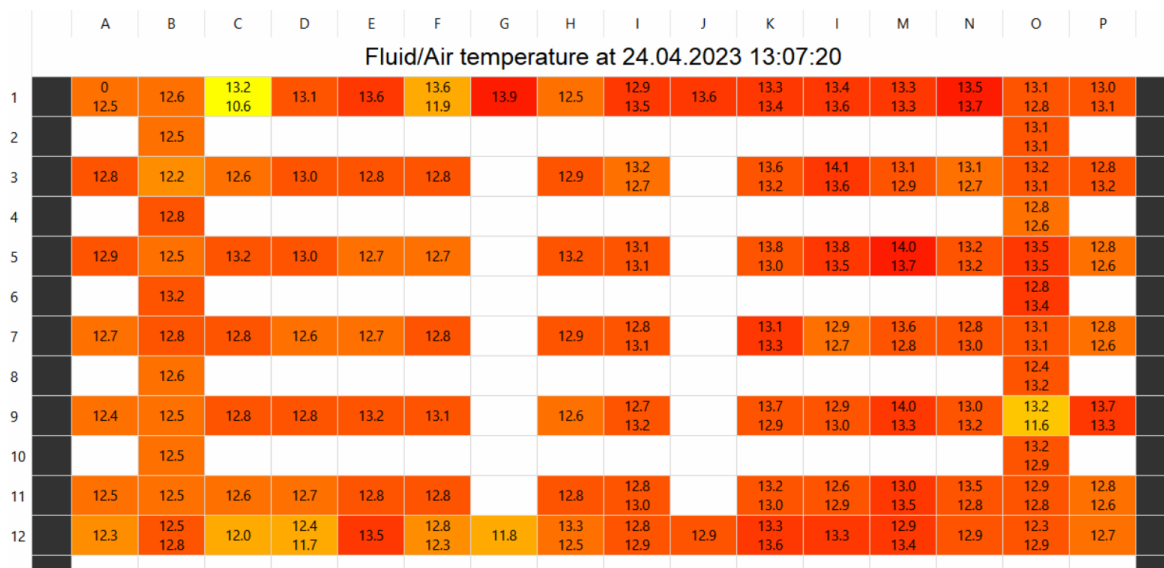
Fig. A.2 Overview of air outlet temperature measurement sensors mounted on the backside of the building-integrated PVT modules in the test facility.
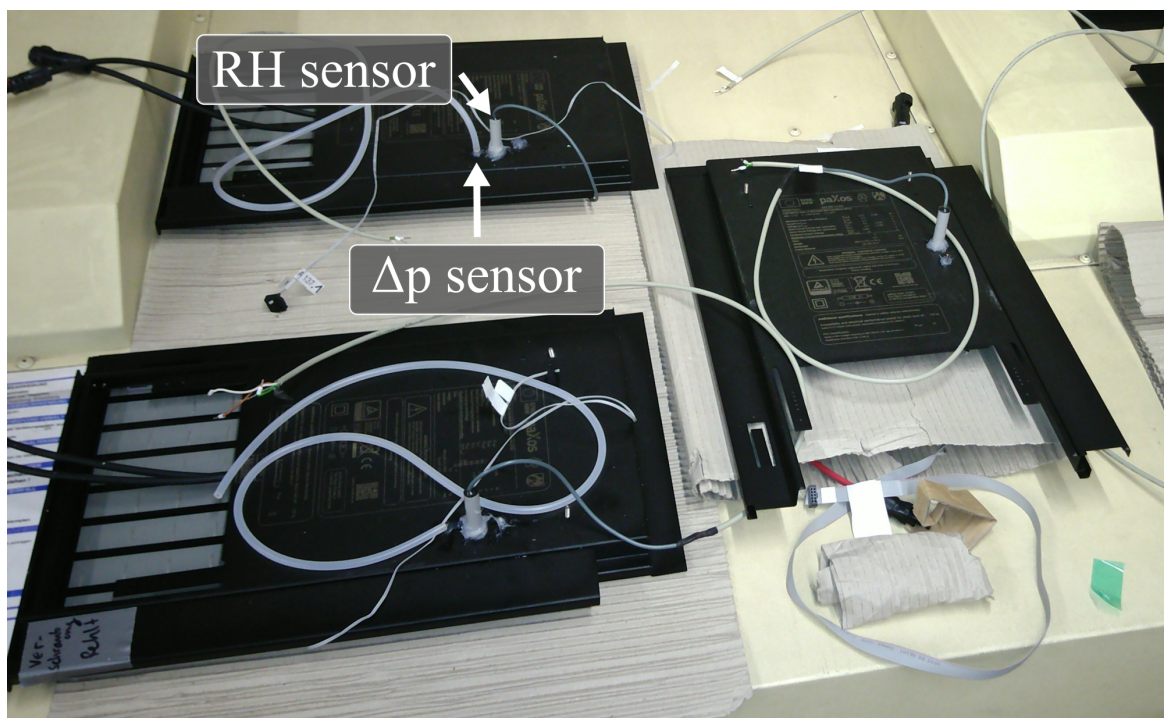
Fig. A.3 Relative humidity (RH) and pressure difference (Δp) sensor mountings on the backside of the aluminum frame of eight building-integrated PVT modules.
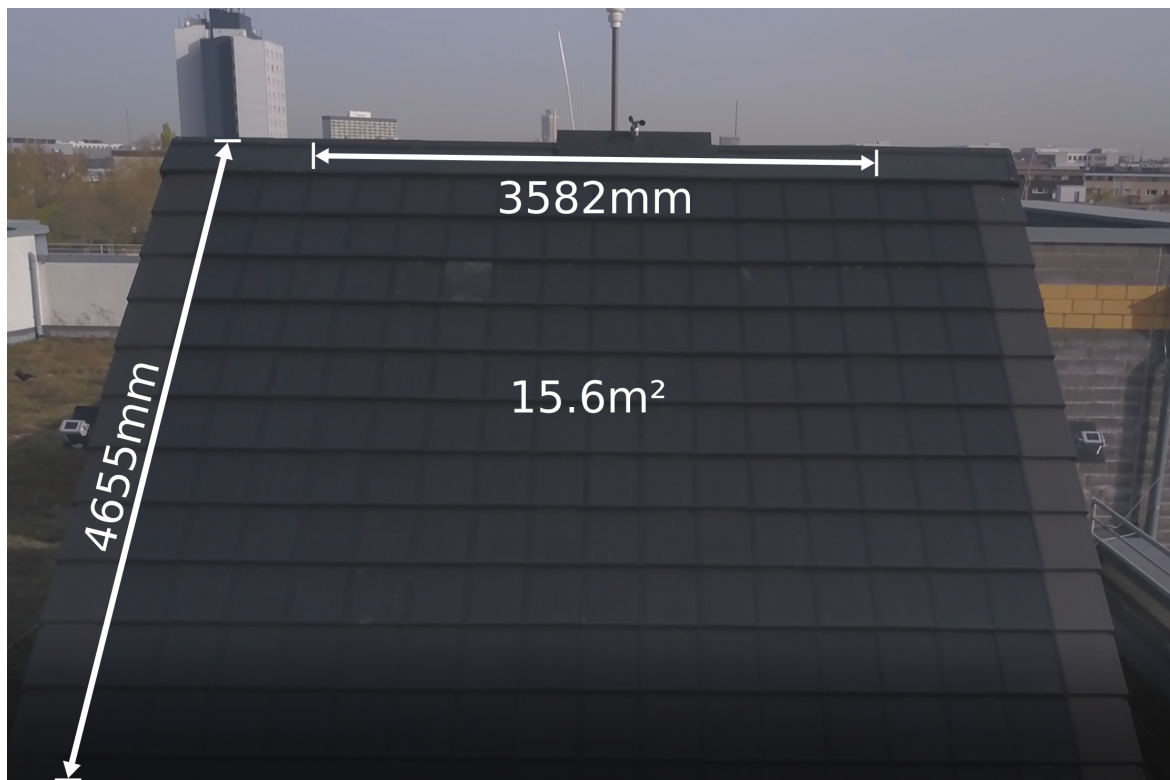
Fig. A.4 Front view and dimensions of the considered gross area of the experimental building-integrated PVT system.
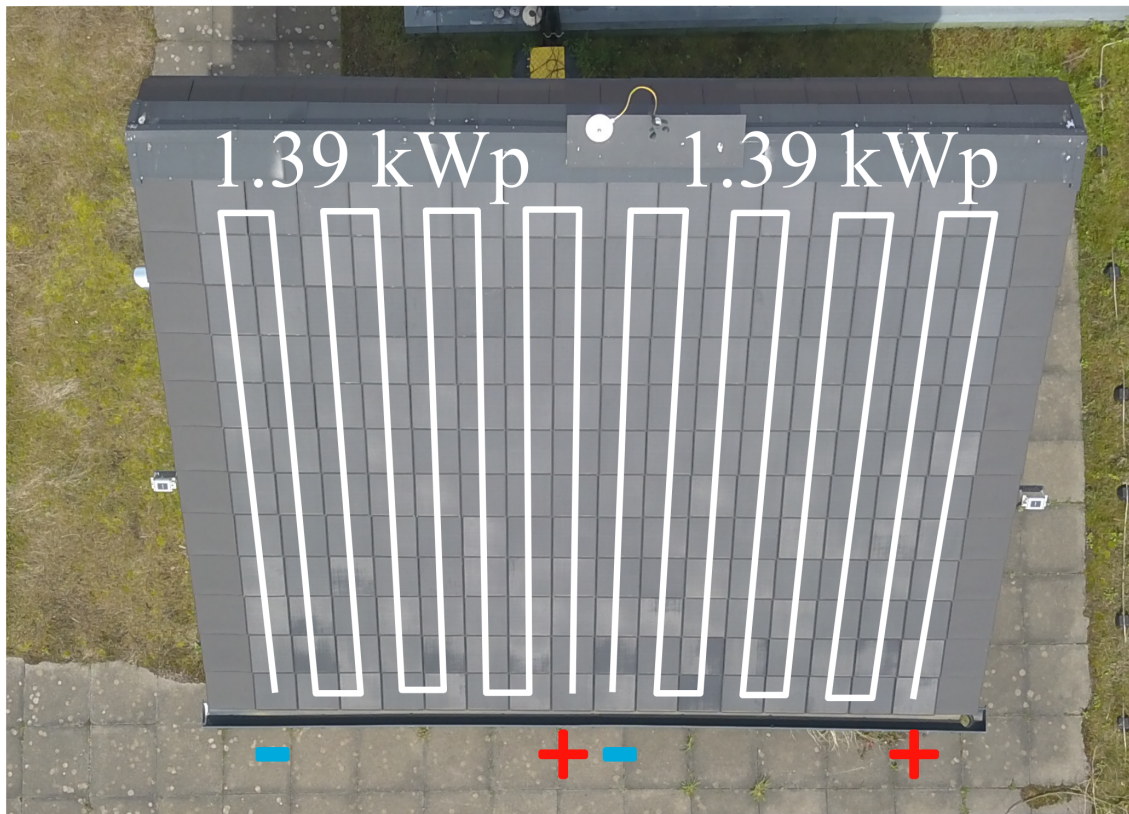
Fig. A.5 Schematic diagram of the electrical string connections of the building-integrated PVT test system. Each string is connected to a separate inverter installed in the attic.
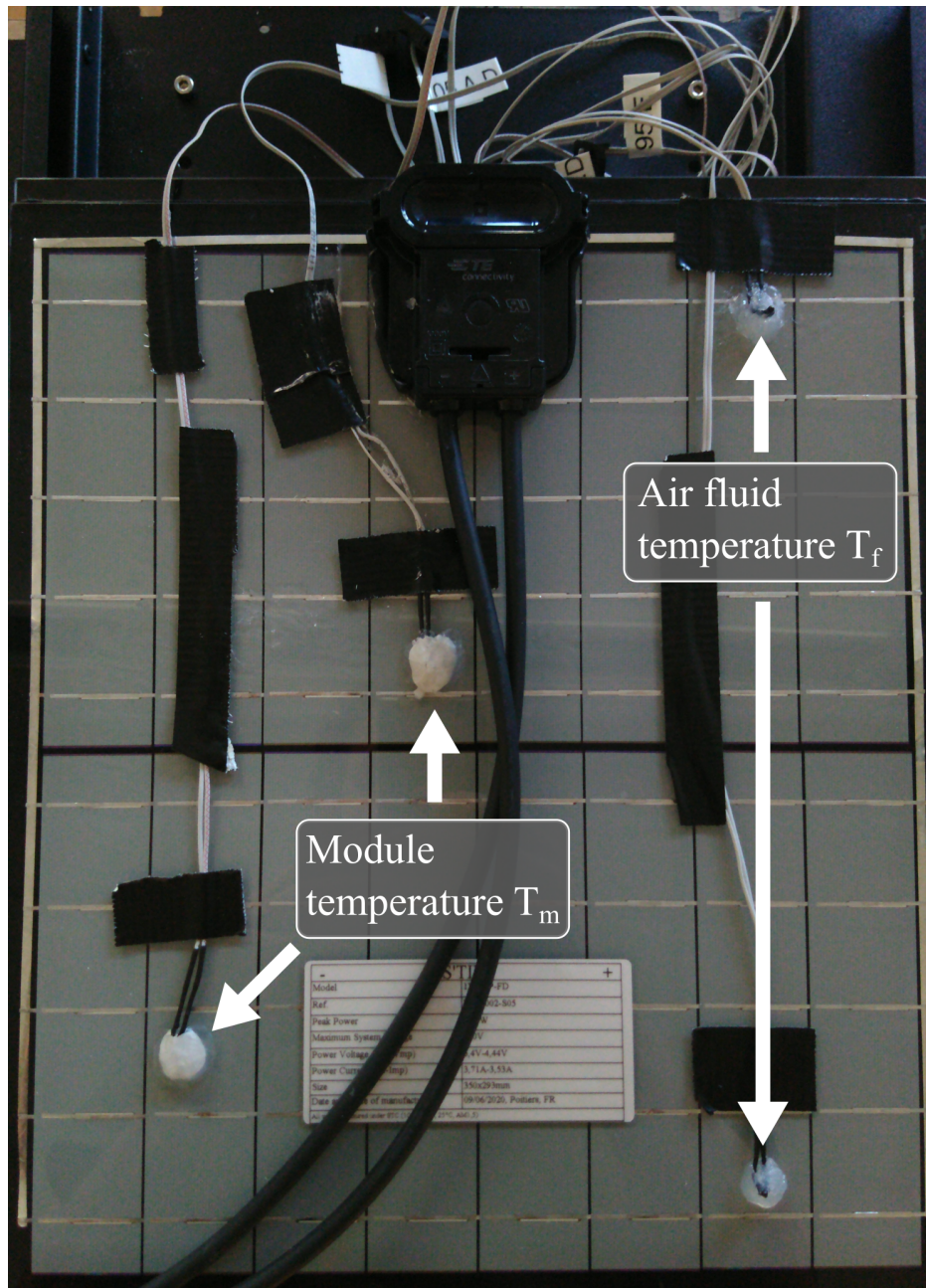
Fig. A.6 Module and air temperature measurement sensors on the backside of the glass-glass module of the BIPVT module.
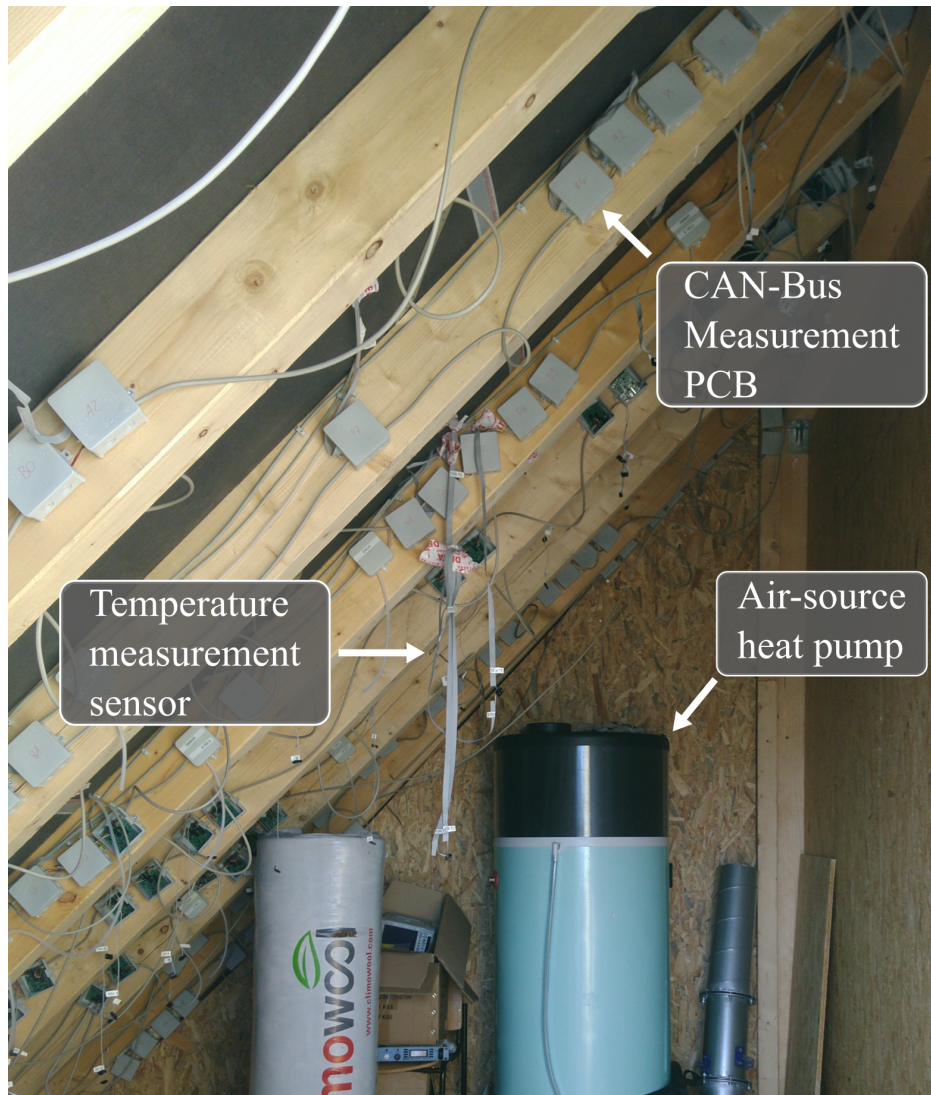
Fig. A.7 Air-source heat pump and CAN field bus installation for module and fluid temperature measurement sensors in the roof construction.
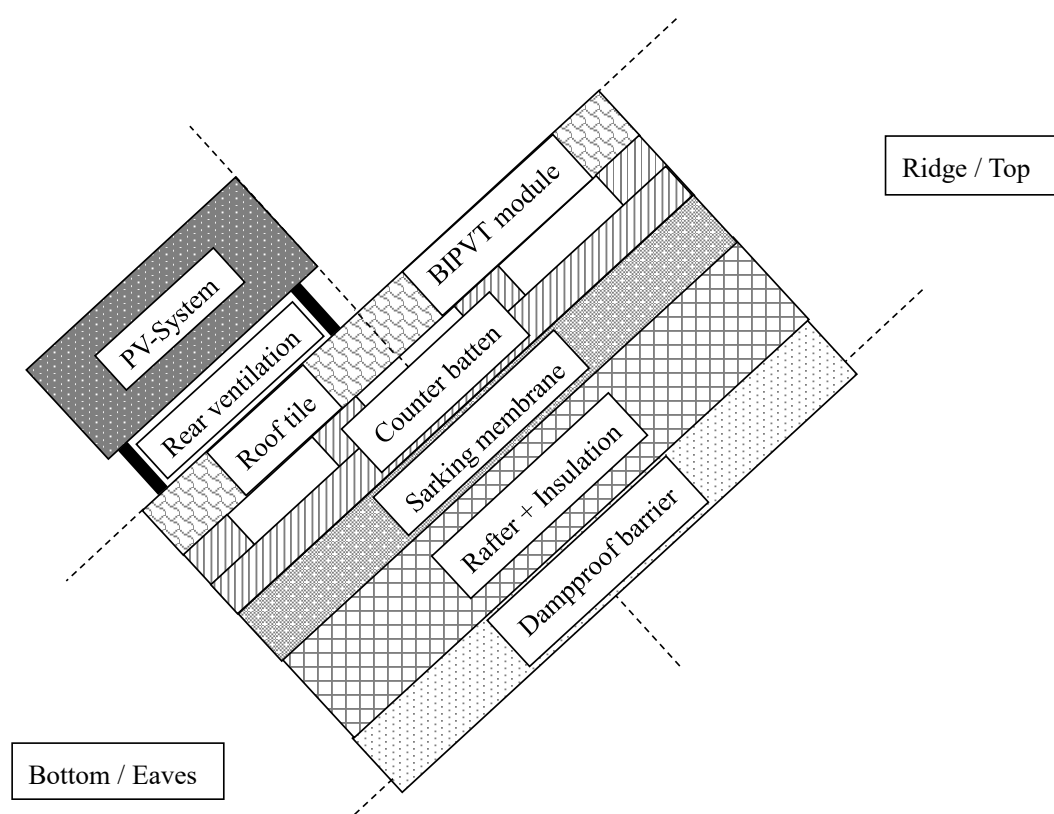
Fig. A.8 Schematic representation of the roof constructions of the test and reference system. Adapted from [163]

Fig. A.9 Interior of the test roof structure with air-source heat pump and data acquisition system.

Fig. A.10 Interior of the reference roof structure with air-source heat pump.

Appendix B

Experimental measurement data

Table B.1 Measured coefficient of performance values of an air-source heat pump connected to an experimental BIPVT system (SAHP) and ambient air (Reference).

Month/Year	COP (SAHP)	COP (Reference)	ΔCOP	Days
Mar/22	3.37	2.86	17.83	3
Apr/22	3.65	2.99	22.07	6
May/22	4.06	3.32	22.29	7
Oct/22	3.77	3.16	19.30	15
Nov/22	3.27	2.87	13.93	22
Dec/22	2.41	2.24	07.59	10
Jan/23	3.07	2.71	13.28	4
Feb/23	2.87	2.3	24.78	5
Mar/23	3.05	2.48	22.98	30
Apr/23	3.17	2.41	31.54	17
	Mean	**Mean**	**Mean**	**Sum**
	3.269	2.734	19.56	119

Table B.2 Measured performance ratio (PR) values of an experimental BIPVT system and standard PV system (Reference) over 14 months.

Month /Year	PR BIPVT	PR Reference	Dev. %	PR_{STC} BIPVT	PR_{STC} Reference	Dev. %
Mrz/22	0.87958	0.88516	-0.63	0.90829	0.86559	4.93
Apr/22	0.86213	0.87425	-1.39	0.88427	0.87578	0.97
Mai/22	0.84989	0.86225	-1.43	0.90231	0.89337	0.02
Jun/22	0.83772	0.86141	-2.74	0.89667	0.90029	0.40
Jul/22	0.83674	0.84653	-1.16	0.89809	0.88991	0.92
Aug/22	0.82487	0.84998	-2.95	0.90188	0.90709	-0.57
Sep/22	0.85147	0.84608	0.64	0.88736	0.86140	3.01
Okt/22	0.86417	0.87255	-0.96	0.88996	0.87965	1.17
Nov/22	0.88653	0.90015	-1.51	0.87922	0.87684	0.27
Dez/22	0.88066	0.90357	-2.54	0.82170	0.85630	-4.04
Jan/23	0.87122	0.91648	-4.94	0.83144	0.86433	-3.81
Feb/23	0.89881	0.91883	-2.18	0.88732	0.89009	-0.31
Mrz/23	0.85916	0.89901	-4.43	0.84110	0.86795	-3.09
Apr/23	0.87247	0.89233	-2.23	0.88408	0.88584	-0.20
Mean	0.86253	0.88061	-2.03	0.87955	0.87960	-0.01

Appendix C

Simulation case study data
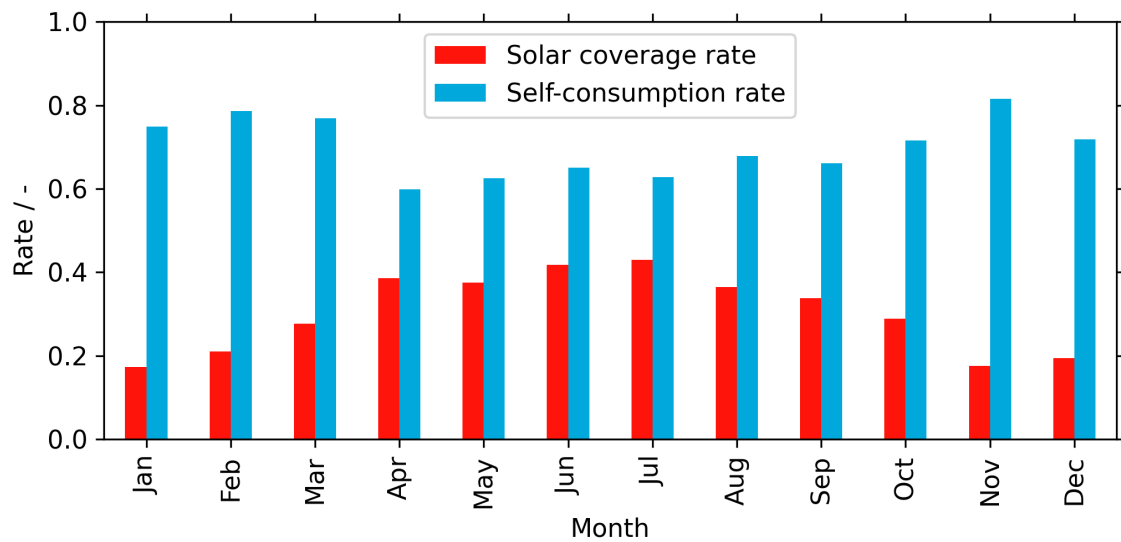
Fig. C.1 Monthly averaged solar coverage and self-consumption rate for the simulation case of Cologne with 30° module tilt angle.

References

[1] IPCC, "AR5 Climate Change 2013: The physical science basis," 1.Intergovernmental Panel on Climate Change (IPCC), Tech. Rep., 2013.

[2] UNFCCC, "Adoption of the paris agreement. proposal by the president," 2.United Nations Framework Convention on Climate Change (UNFCCC), Tech. Rep., 2015.

[3] F. Hülsmeier, A. Heller, S. Huth, S. Knechtges, and J. Reise, "Solar Shell - Die parametrisch optimierte Fassade als Energiequelle," Hochschule für Technik, Wirtschaft und Kultur Leipzig, Abschlussbericht, 2017.

[4] N. Sánchez-Pantoja, R. Vidal, and M. C. Pastor, "Aesthetic perception of photovoltaic integration within new proposals for ecological architecture," *Sustainable Cities and Society*, vol. 39, pp. 203–214, may 2018.

[5] J.-B. Eggers, M. Behnisch, J. Eisenlohr, H. Poglitsch, W.-F. Phung, M. Münzinger, C. Ferrara, and T. E. Kuhn, "PV-Ausbauerfordernisse versus Gebäudepotenzial: Ergebnis einer gebäudescharfen Analyse für ganz Deutschland," in *35. PV-Symposium, Online*, 2020.

[6] S. Chander, A. Purohit, A. Sharma, S. Nehra, and M. Dhaka, "Impact of temperature on performance of series and parallel connected mono-crystalline silicon solar cells," *Energy Reports*, vol. 1, pp. 175–180, nov 2015.

[7] H. Zondag, D. de Vries, W. van Helden, R. van Zolingen, and A. van Steenhoven, "The thermal and electrical yield of a PV-thermal collector," *Solar Energy*, vol. 72, no. 2, pp. 113–128, feb 2002.

[8] H. Wirth, K.-A. Weiß, and C. Wiesmeier, *Photovoltaic Modules, p. 105.* Walter de Gruyter GmbH, 2016.

[9] P. Charalambous, G. Maidment, S. Kalogirou, and K. Yiakoumetti, "Photovoltaic thermal (PV/T) collectors: A review," *Applied Thermal Engineering*, vol. 27, no. 2-3, pp. 275–286, feb 2007.

[10] L. Clasing, C. Dick, U. Blieske, J. Münzberg, P. Hakenberg, S. Leyer, and J.-R. Hadji-Minaglou, "Analysis of a novel improved BIPV/T roof tile design," in *Proc. 15th Conference on sustainable development of energy, water and environment systems (SDEWES)*, Online, 2020.

[11] T. Yang and A. K. Athienitis, "A review of research and developments of building-integrated photovoltaic/thermal (BIPV/T) systems," *Renewable and Sustainable Energy Reviews*, vol. 66, pp. 886–912, dec 2016.

[12] C. Kaysers, "Comparison of the optical efficiency with different types of cell coverage for a solar roof tile via ray tracing," Bachelor's thesis, Cologne University of Applied Sciences, 2020.

[13] S. Krauter, R. G. Araújo, S. Schroer, R. Hanitsch, M. J. Salhi, C. Triebel, and R. Lemoine, "Combined photovoltaic and solar thermal systems for facade integration and building insulation," *Solar Energy*, vol. 67, no. 4-6, pp. 239–248, 1999.

[14] M. Debbarma, K. Sudhakar, and P. Baredar, "Comparison of BIPV and BIPVT: A review," *Resource-Efficient Technologies*, vol. 3, no. 3, pp. 263–271, sep 2017.

[15] J. Wajs, A. Golabek, R. Bochniak, and D. Mikielewicz, "Air-cooled photovoltaic roof tile as an example of the BIPVT system – an experimental study on the energy and exergy performance," *Energy*, vol. 197, p. 117255, apr 2020.

[16] J. Duffie, *Solar engineering of thermal processes.*   Hoboken: Wiley, 2013.

[17] H. ZONDAG, "Flat-plate PV-thermal collectors and systems: A review," *Renewable and Sustainable Energy Reviews*, vol. 12, no. 4, pp. 891–959, may 2008.

[18] G. Quesada, D. Rousse, Y. Dutil, M. Badache, and S. Hallé, "A comprehensive review of solar facades. opaque solar facades," *Renewable and Sustainable Energy Reviews*, vol. 16, no. 5, p. 2820–2832, jun 2012.

[19] H. M. Maghrabie, K. Elsaid, E. T. Sayed, M. A. Abdelkareem, T. Wilberforce, and A. Olabi, "Building-integrated photovoltaic/thermal (BIPVT) systems: Applications and challenges," *Sustainable Energy Technologies and Assessments*, vol. 45, p. 101151, jun 2021.

[20] S. Moosberger-Kropf, "PV/T-Schiefer: Optimierung der Hinterlüftung und der Abwärmenutzung gebäudeintegrierter Photovoltaik," Ph.D. dissertation, ETH Zürich, 2006.

[21] J. A. Candanedo and A. K. Athienitis, "Simulation of the performance of a BIPV/T system coupled to a heat pump in a residential heating application," in *Proc. 9th International IEA Heat Pump Conference*, May 2008.

[22] Y. Chen, K. Galal, and A. K. Athienitis, "Modeling, design and thermal performance of a BIPV/T system thermally coupled with a ventilated concrete slab in a low energy solar house: Part 2, ventilated concrete slab," *Solar Energy*, vol. 84, no. 11, p. 1908–1919, nov 2010.

[23] Y. Chen, A. Athienitis, and K. Galal, "Modeling, design and thermal performance of a BIPV/T system thermally coupled with a ventilated concrete slab in a low energy solar house: Part 1, BIPV/T system and house energy concept," *Solar Energy*, vol. 84, no. 11, pp. 1892–1907, nov 2010.

[24] B. Agrawal and G. Tiwari, "Optimizing the energy and exergy of building integrated photovoltaic thermal (BIPVT) systems under cold climatic conditions," *Applied Energy*, vol. 87, no. 2, pp. 417–426, feb 2010.

[25] S. Pantic, L. Candanedo, and A. Athienitis, "Modeling of energy performance of a house with three configurations of building-integrated photovoltaic/thermal systems," *Energy and Buildings*, vol. 42, no. 10, pp. 1779–1789, oct 2010.

[26] L. M. Candanedo, A. Athienitis, and K.-W. Park, "Convective heat transfer coefficients in a building-integrated photovoltaic/thermal system," *Journal of Solar Energy Engineering*, vol. 133, no. 2, mar 2011.

[27] K. Sinapis, M. Van Den Donker, G. Litjens, P. Michiels, E. Philipse, A. Van Hese, and W. Folkerts, "The glass-glass aesthetic energy roof: Thermal behavior for various ventilation levels," in *Proc. 28th European Photovoltaic Solar Energy Conference and Exhibition*, 2013, pp. 4351–4356.

[28] V. Delisle and M. Kummert, "A novel approach to compare building-integrated photo-voltaics/thermal air collectors to side-by-side PV modules and solar thermal collectors," *Solar Energy*, vol. 100, pp. 50–65, feb 2014.

[29] E. Rounis, E. Bigaila, P. Luk, A. Athienitis, and T. Stathopoulos, "Multiple-inlet BIPV/T modeling: Wind effects and fan induced suction," *Energy Procedia*, vol. 78, pp. 1950–1955, nov 2015.

[30] E. Vuong, R. S. Kamel, and A. S. Fung, "Modelling and simulation of BIPV/T in EnergyPlus and TRNSYS," *Energy Procedia*, vol. 78, pp. 1883–1888, nov 2015.

[31] T. Yang and A. K. Athienitis, "Experimental investigation of a two-inlet air-based building integrated photovoltaic/thermal (BIPV/T) system," *Applied Energy*, vol. 159, pp. 70–79, dec 2015.

[32] C. Brosig, L. Clasing, U. Blieske, and E. Waffenschmidt, "Modeling a novel building-integrated PVT-air-collector system coupled to a heat pump using open source libraries," in *Proc. 16th Conference on Sustainable Development of Energy, Water and Environment Systems (SDEWES)*, Dubrovnik, Croatia, 2021.

[33] M. I. Sohel, Z. Ma, P. Cooper, J. Adams, and R. Scott, "A dynamic model for air-based photovoltaic thermal systems working under real operating conditions," *Applied Energy*, vol. 132, pp. 216–225, nov 2014.

[34] V. Delisle, J.-T. Kim, J. Kim, A. Gagne, and J. Ayoub, "Performance assessment of a new air-based building-integrated photovoltaic thermal solar collector," in *Proc. 33rd European Photovoltaic Solar Energy Conference and Exhibition*, Amsterdam, Netherlands, 2017, pp. 2590–2595.

[35] C. De Keizer, R. Valckenborg, R. Borro, M. Laureijssen, and W. Folkerts, "Using the hot air under a building integrated PV roof in combination with a ventilation heat pump to realise energy efficient dwellings," in *Proc. 35th European Photovoltaic Solar Energy Conference and Exhibition*, Brussels, Belgium, 2018, pp. 1818–1820.

[36] J. Wajs, A. Golabek, and R. Bochniak, "Photovoltaic roof tiles: The influence of heat recovery on overall performance," *Energies*, vol. 12, no. 21, p. 4097, oct 2019.

[37] K. Bot, L. Aelenei, M. da Glória Gomes, and C. S. Silva, "Performance assessment of a building integrated photovoltaic thermal system in mediterranean climate—a numerical simulation approach," *Energies*, vol. 13, no. 11, p. 2887, jun 2020.

[38] A. Fudholi, M. Zohri, I. Taslim, M. A. Indrianti, and I. N. Manyoe, "Theoretical approach model of building integrated photovoltaic thermal air collector," *International Journal of Power Electronics and Drive Systems (IJPEDS)*, vol. 11, no. 2, p. 1002, jun 2020.

[39] K. Meisenzahl, N. Schneble, M. Volk, U. Blieske, L. Clasing, J. Müller-Ost, J. Münzberg, and P. Hakenberg, "Measuring the incidence angle modifier of optically uncoupled glass for PV application," in *Proc. 36th European Photovoltaic Solar Energy Conference and Exhibition*, Marseille, France, 2019.

[40] L. Clasing, J. Münzberg, P. Hakenberg, and U. Blieske, "Neuartiger Entwurf einer Solardachp-fanne zur Lösung anwendungsspezifischer-Probleme," in *Proc. 37. PV-Symposium*, 2022.

[41] M. Meir, "Technology position paper: State-of-the-art and SWOT analysis of building in-tegrated solar envelope systems," *International Energy Agency, Solar heating and cooling programme, Task 56*, nov 2019.

[42] International Energy Agency, "Coloured BIPV: Market, research and development," International Energy Agency, Tech. Rep. IEA-PVPST15-07:2019, 2019.

[43] S. Boppana, K. Passow, J. Sorensen, B. H. King, and C. Robinson, "Impact of uncertainty in IAM measurement on energy predictions," in *Proc. 7th World Conference on Photovoltaic Energy Conversion, WCPEC2018 - A Joint Conference of 45th IEEE PVSC, 28th PVSEC and 34thEU PVSEC*, 2018, p. 2276–2281.

[44] D. J. Wright, "Closed-form, analytic solution for diffuse irradiance on a tilted, photovoltaic collector," *IEEE Journal of Photovoltaics*, vol. 9, no. 2, pp. 391–396, mar 2019.

[45] B. Bläsi, T. Kroyer, O. Höhn, C. Ferrara, and T. E. Kuhn, "Coloured module glass for BIPV inspired by morpho butterfly," in *Proc. 33rd European PV Solar Energy Conference and Exhibition*, Amsterdam, The Netherlands, 2017.

[46] C. Kutter, B. Bläsi, H. Wilson, T. Kroyer, M. Mittag, O. Höhn, and M. Heinrich, "Decorated building-integrated photovoltaic modules: Power loss, color appearance and cost analysis," in *Proc. 35th European Photovoltaic Solar Energy Conference and Exhibition*, Brussels, Belgium, 2018, pp. 1488–1492.

[47] B. Blasi, T. Kroyer, T. Kuhn, and O. Hohn, "The MorphoColor concept for colored photovoltaic modules," *IEEE Journal of Photovoltaics*, vol. 11, no. 5, pp. 1305–1311, sep 2021.

[48] T. Yang and A. K. Athienitis, "Performance evaluation of air-based building integrated photovoltaic/thermal (BIPV/T) system with multiple inlets in a cold climate," *Procedia Engineering*, vol. 121, pp. 2060–2067, 2015.

[49] G. Hailu, T. Yang, A. K. Athienitis, and A. S. Fung, "Computational fluid dynamics (CFD) analysis of building integrated photovoltaic thermal (BIPV/T) systems," in *in Proc. 8th International Conference on Energy Sustainability collocated with the 12th International Conference on Fuel Cell Science, Engineering and Technology*. American Society of Mechanical Engineers, 2014, pp. 139–150.

[50] D. Roeleveld, G. Hailu, A. Fung, D. Naylor, T. Yang, and A. Athienitis, "Validation of computational fluid dynamics (CFD) model of a building integrated photovoltaic/thermal (BIPV/T) system," *Energy Procedia*, vol. 78, pp. 1901–1906, nov 2015.

[51] L. W. Veldhuizen, A. J. Carr, J. Loeffler, M. Dielen, and R. A. J. M. van Erven, "Light management coatings for solar modules by large-area nanoimprinting," in *Proc. 36th European Photovoltaic Solar Energy Conference and Exhibition*, 2019.

[52] L. Clasing, D. Werner-Meier, L. W. Veldhuizen, and U. Blieske, "Experimental assessment of nanoimprinted textured frontsheets for PV modules," in *Proc. 8th World Conference on Photovoltaic Energy Conversion*, Milan, Italy, 2022.

[53] C. Welz, P. D. Lauro, C. Thoma, J. Richter, M. Hermann, G. Stryi-H, and C. Maurer, "Physikalische Modellierung und Simulation sowie detaillierte Vermessung von Luftkollektoren," in *Proc. 22. OTTI-Symposium Thermische Solarenergie*. Unpublished, 2012.

[54] C. Welz, M. Knecht, C. Maurer, P. D. Lauro, G. Stryi-Hipp, and M. Hermann, "Thermohydraulische Simulation von Luftkollektoren und Luftkollektorsystemen: Systembezogene Bewertung von Luftkollektoren," in *Proc. 23. OTTI-Symposium Thermische Solarenergie*, 2013.

[55] K. S. Kramer, C. Thoma, S. Mehnert, and S. Fahr, "Testing solar air-heating collectors," *Energy Procedia*, vol. 48, pp. 137–144, 2014.

[56] S. Rai, P. Chand, and S. Sharma, "Evaluation of thermo hydraulic effect on offset finned absorber solar air heater," *Renewable Energy*, vol. 125, pp. 39–54, sep 2018.

[57] IEC61853-2, "Photovoltaic (PV) module performance testing and energy rating - part 2: spectral responsivity, incidence angle and module operating temperature measurements," International Electrical Commission, 2016.

[58] N. Reiners, U. Blieske, P. Hakenberg, and J. Münzberg, "Transmissivity and aesthetics of optically uncoupled glasses for the application in a PVT roof tile," in *Proc. 35th European Photovoltaic Solar Energy Conference and Exhibition*, Brussels, Belgium, 2018, pp. 1845–1847.

[59] A. Souka and H. Safwat, "Determination of the optimum orientations for the double-exposure, flat-plate collector and its reflectors," *Solar Energy*, vol. 10, no. 4, pp. 170–174, oct 1966.

[60] S. A. Mumma, J. I. Yellott, and B. Wood, "Application of ashrae standard 93-77 to the thermal performance testing of air solar collectors," *ASHRAE J.; (United States)*, vol. 84:2, 1 1978. [Online]. Available: https://www.osti.gov/biblio/6149565

[61] D. L. King, J. A. Kratochvil, and W. E. Boyson, "Measuring solar spectral and angle-of-incidence effects on photovoltaic modules and solar irradiance sensors," in *Proc. 26th IEEE Photovoltaic Specialists Conference*, a. W. E. B. David L. King, Jay A. Kratochvil, Ed.   Sandia National Laboratories, 1997.

[62] J. K. D.L. King, W.E. Boyson, "Photovoltaic array performance model," Sandia National Laboratories, techreport, 2004.

[63] B. H. King, C. W. Hansen, D. Riley, C. D. Robinson, and L. Pratt, "Procedure to determine coefficients for the sandia array performance model (SAPM)," National Renewable Energy Laboratory, Tech. Rep., jun 2016.

[64] N. Martín and J. Ruiz, "Calculation of the PV modules angular losses under feld conditions by means of an analytical model," *Solar Energy Materials & Solar Cells*, vol. 70, pp. 25–38, 2001.

[65] N. Martín and J. M. Ruiz, "A new model for PV modules angular losses under field conditions," *International Journal of Solar Energy*, vol. 22, no. 1, pp. 19–31, 2002.

[66] N. Martín and J. M. Ruiz, "Annual angular reflection losses in PV modules," *Progress in Photovoltaics: Research and Applications*, vol. 13, no. 1, pp. 75–84, nov 2004.

[67] B. Marion, "Numerical method for angle-of-incidence correction factors for diffuse radiation incident photovoltaic modules," *Solar Energy*, vol. 147, pp. 344–348, may 2017.

[68] H. Helmers and K. Kramer, "Multi-linear performance model for hybrid (c)PVT solar collectors," *Solar Energy*, vol. 92, pp. 313–322, jun 2013.

[69] W. H. McAdams, *Heat Transmission*.   Kogakusha: McGraw-Hill New York-London, dec 1954, vol. 120.

[70] M. Lämmle, T. Kroyer, S. Fortuin, M. Wiese, and M. Hermann, "Development and modelling of highly-efficient PVT collectors with low-emissivity coatings," *Solar Energy*, vol. 130, pp. 161–173, jun 2016.

[71] W. C. Swinbank, "Long-wave radiation from clear skies," *Quarterly Journal of the Royal Meteorological Society*, vol. 89, no. 381, pp. 339–348, jul 1963.

[72] P. von Böckh and T. Wetzel, *Wärmeübertragung*. Springer Berlin Heidelberg, 2014.

[73] IEC61853-1, "Photovoltaic (PV) module performance testing and energy rating - part 1: Irradiance and temperature performance measurements and power rating," International Electrical Commission, 2011.

[74] S. R. Wenham, M. A. Green, and M. E. Watt, *Applied Photovoltaics*. Centre for Photovoltaic Devices and Systems, 2021.

[75] W. D. Soto, S. Klein, and W. Beckman, "Improvement and validation of a model for photovoltaic array performance," *Solar Energy*, vol. 80, no. 1, pp. 78–88, jan 2006.

[76] M. K. Fuentes, "A simplifed thermal model for flat-plate photovoltaic arrays," Sandia National Laboratories, Albuquerque NM, Tech. Rep., 1987.

[77] D. Faiman, "Assessing the outdoor operating temperature of photovoltaic modules," *Progress in Photovoltaics: Research and Applications*, vol. 16, no. 4, pp. 307–315, jun 2008.

[78] A. Dobos, "PVWatts version 5 manual," Tech. Rep., sep 2014.

[79] IEC60904-8, "Photovoltaic devices - part 8: Measurement of spectral responsivity of a photovoltaic (PV) device," International Electrical Commission, International Electrotechnical Commission, 2014.

[80] *FiMo SR-EQE 100 Spectral Response Scanner User Manual V 1.6*, Aescusoft Automation, 2009.

[81] N. Reiners, "Angle and spectral dependence of the internal and the external quantum efficiency of solar modules," Ph.D. dissertation, Technische Hochschule Köln, 2018.

[82] U. Blieske and G. Stollwerck, *Glass and Other Encapsulation Material in Advances in Photovoltaics: Part 2, pp. 201 ff.* ACADEMIC PR INC, 2013.

[83] F. Pedrotti, L. Pedrotti, W. Bausch, and H. Schmitt, *Optik für Ingenieure: Grundlagen (German Edition), pp. 47.* Springer, 2005.

[84] Schröder and Treiber, *Technical Optics, p. 30*, ser. 10. Issue. Wuerzburg: Vogel, 2007.

[85] N. Jolissaint, R. Hanbali, J.-C. Hadorn, and A. Schüler, "Colored solar façades for buildings," *Energy Procedia*, vol. 122, pp. 175–180, sep 2017.

[86] S. Albrecht, "Conceptual design of the mechanical construction of a measuring stage for automated angle-dependent measurements," Bachelor's thesis, University of Applied Sciences Cologne, 2021.

[87] E. A. Alva Coletti, "Development of a software for the automatization of incidence angle modifier measurements of solar modules," Bachelor's thesis, University of Applied Sciences Cologne, 2020.

[88] N. Riedel, A. Santamaria Lancia, M. Amdemeskel, S. Thorsteinsson, P. Poulsen, F. Plag, I. Kröger, L. Slooff, M. Jansen, A. Carr, P. Manshanden, M. Bliss, T. Betts, I. Petrina Jauregui, M. Ezquer Mayo, J. Balenzategui, R. Roldán, U. Kräling, G. Baarah, B. Iandolo, R. Davidsen, A. Thorseth, C. Dam-Hansen, and G. Dos Reis Benatto, "Interlaboratory comparison of methodologies for measuring the angle of incidence dependence of solar cells," in *Proc. 35th European Photovoltaic Solar Energy Conference and Exhibition*, Brussels, Belgium, 2018, pp. 1034–1039.

[89] N. Riedel-Lyngskær, A. A. S. Lancia, F. Plag, I. Kröger, M. R. Vogt, C. Schinke, R. S. Davidsen, M. Amdemeskel, M. J. Jansen, P. Manshanden, L. H. Slooff, A. J. Carr, M. Bliss, T. Betts, M. E. Mayo, I. P. Jauregui, J. L. Balenzategui, R. Roldan, G. Bellenda, M. Caccivio, U. Kräling, F. Neuberger, D. Zirzow, J. Crimmins, C. Robinson, B. King, W. Teasdale, C. Kedir, J. Watts, R. Desharnais, P. B. Poulsen, M. L. Jakobsen, and G. A. R. Benatto, "Interlaboratory comparison of angular-dependent photovoltaic device measurements: Results and impact on energy rating," *Progress in Photovoltaics: Research and Applications*, dec 2020.

[90] M. Schweiger and W. Herrmann, "Solar simulator measurement procedures for determination of the angular characteristic of PV modules," in *Proc. 29th European Photovoltaic Solar Energy Conference and Exhibition*, Amsterdam, Netherlands, 2014.

[91] F. Plag, I. Kröger, T. Fey, F. Witt, and S. Winter, "Angular-dependent spectral responsivity-traceable measurements on optical losses in PV devices," *Progress in Photovoltaics: Research and Applications*, vol. 26, no. 8, pp. 565–578, nov 2017.

[92] N. Reiners, U. Blieske, and S. Siebentritt, "Investigation on the angle and spectral dependence of the internal and the external quantum efficiency of crystalline silicon solar cells and modules," *IEEE Journal of Photovoltaics*, vol. 8, no. 6, pp. 1738–1747, nov 2018.

[93] L. Clasing, P. Yam, C. Ziller, and U. Blieske, "Dynamic simulation model of an air-based BIPVT roof tile system," in *Proc. 8th World Conference on Photovoltaic Energy Conversion*, Milan, Italy, 2022, pp. 662–665.

[94] ISO9806-2017, "Solar energy – solar thermal collectors – test methods," International Organization for Standardization, International Organization for Standardization, 2017.

[95] P. Loutzenhiser, H. Manz, C. Felsmann, P. Strachan, T. Frank, and G. Maxwell, "Empirical validation of models to compute solar irradiance on inclined surfaces for building energy simulation," *Solar Energy*, vol. 81, no. 2, pp. 254–267, feb 2007.

[96] T. Klucher, "Evaluation of models to predict insolation on tilted surfaces," *Solar Energy*, vol. 23, no. 2, pp. 111–114, 1979.

[97] Perez, "Modeling daylight availability and irradiance components from direct and global irradiance," *Solar Energy*, vol. 44, no. 5, pp. 271–289, 1990.

[98] J. E. Hay, "Calculating solar radiation for inclined surfaces: Practical approaches," *Renewable Energy*, vol. 3, no. 4-5, pp. 373–380, jun 1993.

[99] M. Hofmann and G. Seckmeyer, "A new model for estimating the diffuse fraction of solar irradiance for photovoltaic system simulations," *Energies*, vol. 10, no. 2, p. 248, feb 2017.

[100] M. Lave, W. Hayes, A. Pohl, and C. W. Hansen, "Evaluation of global horizontal irradiance to plane-of-array irradiance models at locations across the united states," *IEEE Journal of Photovoltaics*, vol. 5, no. 2, pp. 597–606, mar 2015.

[101] M. Bartkowski, H. Saleemi, L. Clasing, C. Brosig, E. Waffenschmidt, and U. Blieske, "Development and validation of a model for performance simulation of an air-based BIPVT roof tile system using open-source libraries," in *Proc. 8th World Conference on Photovoltaic Energy Conversion*, Milan, Italy, 2022, pp. 716–723.

[102] A. P. Dobos, "An improved coefficient calculator for the california energy commission 6 parameter photovoltaic module model," *Journal of Solar Energy Engineering*, vol. 134, no. 2, mar 2012.

[103] F. M. White and S. Klein, *Fluid mechanics*, 7th ed.   McGraw-Hill, New York, 2011.

[104] Y. A. Cengel and S. Klein, *Heat and mass transfer : a practical approach*, 3rd ed.   McGraw-Hill, Singapore, 2007.

[105] E. Mayer, A. Zegowitz, and M. Kersken, "Messung des konvektiven Wärmeübergangs - Entwicklung eines neuen Sensors und bauphysikalische Anwendungen," *Bauphysik*, vol. 40, no. 5, pp. 336–343, oct 2018.

[106] A. Cortés and R. Piacentini, "Improvement of the efficiency of a bare solar collector by means of turbulence promoters," *Applied Energy*, vol. 36, no. 4, pp. 253–261, jan 1990.

[107] PVGIS. (2022) Photovoltaic geographical information system. Online: https://joint-research-centre.ec.europa.eu/pvgis-online-tool. Joint Research Centre European Commission. Accessed: June 14, 2022.

[108] L. Clasing, N. Riedel-Lyngskær, N. Reiners, and U. Blieske, "Simulation of colored BIPV modules using angular-dependent spectral responsivity," *IEEE Journal of Photovoltaics*, vol. 13, no. 4, pp. 1–9, jul 2023.

[109] M. C. M. Probst and C. Roecker, "Criteria and policies to master the visual impact of solar systems in urban environments: The LESO-QSV method," *Solar Energy*, vol. 184, pp. 672–687, may 2019.

[110] H. Kaan and T. Reijenga, "Photovoltaics in an architectural context," *Progress in Photovoltaics: Research and Applications*, vol. 12, no. 6, pp. 395–408, sep 2004.

[111] E. Saretta, P. Bonomo, and F. Frontini, "BIPV meets customizable glass: A dialogue between energy efficiency and aesthetics," in *Proc. 35th European Photovoltaic Solar Energy Conference and Exhibition*, Brussels, Belgium, 2018, pp. 1472–1477.

[112] M. Mittag, M. Ebert, H. Wilson, and T. Fellmeth, "Mosaic module concept for cost-efficient and aesthetic BIPV modules," in *35th European Photovoltaic Solar Energy Conference and Exhibition*, 2018, pp. 1458–1462.

[113] M. Lee and A. Panchula, "Spectral correction for photovoltaic module performance based on air mass and precipitable water," in *Proc. IEEE 43rd Photovoltaic Specialists Conference (PVSC)*, Portland, OR, USA, Jun. 2016.

[114] W. Herrmann, A. Steland, and W. Herff, "Sampling procedures for the validation of PV module output power specification," in *Proc. 24th European Photovoltaic Solar Energy Conference*, Germany, 2009, pp. 3540–3547.

[115] B. C. Duck and C. J. Fell, "Improving the spectral correction function," in *Proc. IEEE 43rd Photovoltaic Specialists Conference (PVSC)*.   IEEE, Jun. 2016.

[116] F. Plag, I. Kröger, S. Riechelmann, and S. Winter, "Multidimensional model to correct PV device performance measurements taken under diffuse irradiation to reference conditions," *Solar Energy*, vol. 174, pp. 431–444, nov 2018.

[117] M. H. Saw, J. P. Singh, Y. Wang, K. E. Birgersson, and Y. S. Khoo, "Electrical performance study of colored c-si building-integrated PV modules," *IEEE Journal of Photovoltaics*, vol. 10, no. 4, pp. 1027–1034, jul 2020.

[118] M. H. Saw, M. Pravettoni, and E. Birgersson, "STC short-circuit current prediction and I-V simulation of colored BIPV modules with machine learning and one-diode equivalent circuit models," *IEEE Journal of Photovoltaics*, vol. 12, no. 6, pp. 1533–1542, nov 2022.

[119] J. E. Gonçalves, T. van Hooff, and D. Saelens, "Simulating building integrated photovoltaic facades: Comparison to experimental data and evaluation of modelling complexity," *Applied Energy*, vol. 281, p. 116032, jan 2021.

[120] M. K. Sharma and J. Bhattacharya, "Dependence of spectral factor on angle of incidence for monocrystalline silicon based photovoltaic solar panel," *Renewable Energy*, vol. 184, pp. 820–829, jan 2022.

[121] IEC60904-7, "Photovoltaic (PV) devices – part 7: Computation of the spectral mismatch correction for measurements of photovoltaic devices," International Electrical Commission, 2019.

[122] C. Gueymard, "SMARTS, A simple model of the atmospheric radiative transfer of sunshine: Algorithms and performance assessment." 1679 Clearlake Rd., Cocoa: Florida Solar Energy Center, 1995, fL 32922: Professional Paper FSEC-PF-270-95.

[123] J. Gjessing and E. S. Marstein, "An optical model for predicting the quantum efficiency of solar modules," *IEEE Journal of Photovoltaics*, vol. 4, no. 1, pp. 304–310, jan 2014.

[124] R. J. Beal, B. G. Potter, and J. H. Simmons, "Angle of incidence effects on external quantum efficiency in multicrystalline silicon photovoltaics," *IEEE Journal of Photovoltaics*, vol. 4, no. 6, pp. 1459–1464, nov 2014.

[125] I. Geisemeyer, N. Tucher, B. Muller, H. Steinkemper, J. Hohl-Ebinger, M. C. Schubert, and W. Warta, "Angle dependence of solar cells and modules: The role of cell texturization," *IEEE Journal of Photovoltaics*, vol. 7, no. 1, pp. 19–24, jan 2017.

[126] W. Tian, Y. Wang, J. Ren, and L. Zhu, "Effect of urban climate on building integrated photovoltaics performance," *Energy Conversion and Management*, vol. 48, no. 1, pp. 1–8, jan 2007.

[127] M. R. Lewis, E. M. Tonita, C. E. Valdivia, R.-J. K. Obhi, J. Leslie, M. I. Bertoni, and K. Hinzer, "Angular dependence of textured bifacial silicon heterojunction solar cells for high latitudes," in *Proc. IEEE 46th Photovoltaic Specialists Conference (PVSC)*. Chicago, United States: IEEE, Jun. 2019.

[128] S. Pal, A. Reinders, and R. Saive, "Simulation of bifacial and monofacial silicon solar cell short-circuit current density under measured spectro-angular solar irradiance," *IEEE Journal of Photovoltaics*, vol. 10, no. 6, pp. 1803–1815, nov 2020.

[129] L. Clasing, S. Schaaf, U. Blieske, N. Riedel-Lyngskær, A. Santamaria Lancia, and N. Reiners, "Calculation of the short-circuit current of colored BIPV modules under field conditions by application of spectrally and angle resolved measurement data," in *Proc. 38th European Photovoltaic Solar Energy Conference and Exhibition*. WIP, 2021, pp. 803–807.

[130] N. Riedel, A. Thorseth, A. A. S. Lancia, S. Thorsteinsson, P. Poulsen, B. Iandolo, R. S. Davidsen, and G. Benatto, "Direct beam and diffuse spectral irradiance measurements in a nordic country analyzed with the average photon energy parameter," jun 2018.

[131] M. Ernst, H. Holst, M. Winter, and P. P. Altermatt, "SunCalculator: A program to calculate the angular and spectral distribution of direct and diffuse solar radiation," *Solar Energy Materials and Solar Cells*, vol. 157, pp. 913–922, dec 2016.

[132] M. R. J. Stein, C. Hansen, "The variability index: A new and novel metric for quantifying irradiance and PV output variability," 2012.

[133] M. Babin, A. Bertomeu I Baldé, S. Spataru, M. Jakobsen, and S. Thorsteinsson, "Study of optical transmission losses of satinated PV glass," in *Proc. 8th World Conference on Photovoltaic Energy Conversion*, Milan, Italy, 2022, pp. 642–645.

[134] M. Babin, S. Thorsteinsson, A. Santamaria Lancia, P. Poulsen, A. Thorseth, C. Dam-Hansen, and M. Jakobsen, "Dependency of IAM losses in colored BIPV products on the refractive index of colorants," in *Proc. 38th European Photovoltaic Solar Energy Conference and Exhibition*, Online, 2021, pp. 583–588.

[135] A. Shikoh, T. Betts, S. Williams, R. Gottschalg, D. Neumann, and M. Prast, "Representation of optical losses in PV system yield estimates," in *Proc. 27th European Photovoltaic Solar Energy Conference and Exhibition*, N. W. e. a. Shikoh, A. S., Ed.   Centre for Renewable Energy Systems Technology, Loughborough University, Saint-Gobain Sekurit Deutschland GmbH & Co. KG, 2012, pp. 3351–3355.

[136] IEC60904-9, "Classification of solar simulator characteristics," International Electrotechnical Commission, 2018.

[137] A. Hedau and R. Saini, "Thermo-hydraulic performance of double pass solar air heater duct having semi-circular tubes and perforated blocks as artificial roughness," *Renewable Energy*, vol. 205, pp. 543–562, mar 2023.

[138] Y. Assoa and C. Ménézo, "Dynamic study of a new concept of photovoltaic–thermal hybrid collector," *Solar Energy*, vol. 107, pp. 637–652, sep 2014.

[139] IEC61724-1, "Photovoltaic system performance - part 1: Monitoring," International Electrical Commission, International Electrotechnical Commission, 2021.

[140] R. S. Kamel, A. S. Fung, and P. R. Dash, "Solar systems and their integration with heat pumps: A review," *Energy and Buildings*, vol. 87, pp. 395–412, jan 2015.

[141] K. Sezen and A. Gungor, "Comparison of solar assisted heat pump systems for heating residences: A review," *Solar Energy*, vol. 249, pp. 424–445, jan 2023.

[142] F. J. Müller-Flammann, "Development of a LabVIEW program for acquisition of measurement data from a test roof surface with solar roof tiles," Bachelor's thesis, University of Applied Sciences Cologne, 2022.

[143] G. Joentgen, "Automated, can-bus-based long term measuring system with 250 bus participants," Bachelor's thesis, University of Applied Sciences Cologne, 2021.

[144] M. Nießen, P. Deck, G. Jöntgen, L. Clasing, U. Blieske, and C. P. Dick, "Electrical interconnection of a solar roof-tile system: System topology and microconverter," in *Proc. 16th Conference on sustainable development of energy, water and environment systems (SDEWES)*, 2021.

[145] ISO9847:1992, "Solar energy — calibration of field pyranometers by comparison to a reference pyranometer," International Organization for Standardization, 1992.

[146] IEC60904-1:2020, "Photovoltaic devices - part 1: Measurement of photovoltaic current-voltage characteristics," International Electrotechnical Commission, 2020.

[147] C. von Holst, "Energetic evaluation of a novel hybrid solar roof tile based on a comparative ten-month field test," Bachelor's thesis, University of Applied Sciences Cologne, 2023.

[148] N. H. Reich, B. Mueller, A. Armbruster, W. G. J. H. M. van Sark, K. Kiefer, and C. Reise, "Performance ratio revisited: is PR > 90% realistic?" *Progress in Photovoltaics: Research and Applications*, vol. 20, no. 6, pp. 717–726, jan 2012.

[149] N. M. Kumar, M. Samykano, and A. Karthick, "Energy loss analysis of a large scale BIPV system for university buildings in tropical weather conditions: A partial and cumulative performance ratio approach," *Case Studies in Thermal Engineering*, vol. 25, p. 100916, jun 2021.

[150] A. Alazazmeh, A. Ahmed, M. Siddiqui, and M. Asif, "Real-time data-based performance analysis of a large-scale building applied PV system," *Energy Reports*, vol. 8, pp. 15 408– 15 420, nov 2022.

[151] I. Staffell, D. Brett, N. Brandon, and A. Hawkes, "A review of domestic heat pumps," *Energy & Environmental Science*, vol. 5, no. 11, p. 9291, 2012.

[152] O. Ruhnau, L. Hirth, and A. Praktiknjo, "Time series of heat demand and heat pump efficiency for energy system modeling," *Scientific Data*, vol. 6, no. 1, oct 2019.

[153] I. Staffell, P. Baker, J. P. Barton, N. Bergman, R. Blanchard, N. P. Brandon, D. J. L. Brett, A. Hawkes, D. Infield, C. N. Jardine, N. Kelly, M. Leach, M. Matian, A. D. Peacock, S. Sudthar-alingam, and B. Woodman, "UK microgeneration. part II: technology overviews," *Proceedings of the Institution of Civil Engineers - Energy*, vol. 163, no. 4, pp. 143–165, nov 2010.

[154] K. Mertens, *Photovoltaik: Lehrbuch zu Grundlagen, Technologie und Praxis, pp. 201*. Carl Hanser Verlag GmbH & Co. KG, 2022.

[155] BMWK, DestatisFS5R3, and BDEW, "Durchschnittlicher Haushaltsstromver-brauch," Online: https://www.bdew.de/service/daten-und-grafiken/durchschnittlicher-haushaltsstromverbrauch/, 2022, accessed: June 23, 2023.

[156] T. Tjaden, J. Bergner, J. Weniger, and V. Quaschning, "Repräsentative elektrische Last-profile für Wohngebäude in Deutschland auf 1-sekündiger Datenbasis," Online Data: https://solar.htw-berlin.de/elektrische-lastprofile-fuer-wohngebaeude/, accessed: November 14, 2022, Hochschule für Technik und Wirtschaft (HTW) Berlin, License: CC-BY-NC-4.0.

[157] U. Jordan and K. Vajen, "Influence of the DHW-load profile on the fractional energy savings: A case study of a solar combi-system with TRNSYS simulations," in *Proc. EuroSun '00, Copenhagen, Denmark*, 2000.

[158] ISO15927-4, "Hygrothermal performance of buildings — Calculation and presentation of climatic data — part 4: Hourly data for assessing the annual energy use for heating and cooling," International Organization for Standardization, 2005.

[159] T. Huld, E. Paietta, P. Zangheri, and I. P. Pascua, "Assembling typical meteorological year data sets for building energy performance using reanalysis and satellite-based data," *Atmosphere*, vol. 9, no. 2, p. 53, feb 2018.

[160] A. Gracia Amillo, N. Taylor, A. Martinez Fernandez, E. Dunlop, P. Mavrogiorgios, F. Fahl, G. Arcaro, and I. Pinedo, "Adapting PVGIS to trends in climate, technology and user needs," in *Proc. 38th European Photovoltaic Solar Energy Conference and Exhibition*, 2021, pp. 907–911.

[161] H. E. Beck, N. E. Zimmermann, T. R. McVicar, N. Vergopolan, A. Berg, and E. F. Wood, "Present and future Köppen-Geiger climate classification maps at 1-km resolution," *Scientific Data*, vol. 5, no. 1, oct 2018.

[162] A. Gagliano, G. M. Tina, S. Aneli, and D. Chemisana, "Analysis of the performances of a building-integrated PV/thermal system," *Journal of Cleaner Production*, vol. 320, p. 128876, oct 2021.

[163] S. Lentz, "Solardachpfanne.NRW – Vergleichende Betrachtung von Aufdach- und Indachsolar-modulen," Cologne University of Applied Sciences, Tech. Rep., 2022.

Publications

First author:

- L. Clasing, N. Riedel-Lyngskær, N. Reiners, and U. Blieske, **"Simulation of Colored BIPV Modules Using Angular-Dependent Spectral Responsivity,"** IEEE Journal of Photovoltaics, vol. 13, no. 4, July 2023, pp. 632-640, doi: 10.1109/JPHOTOV.2023.3267680.

- L. Clasing, P. H. Yam, C. Ziller, and U. Blieske, **"Dynamic Simulation Model of an Air-Based BIPVT Roof Tile System,"** in Proc. 8th World Conference on Photovoltaic Energy Conversion, Milan, Italy, 2022, pp. 662–665, doi: 10.4229/WCPEC-82022-3BV.3.16.

- L. Clasing, D. Werner-Meier, L. W. Veldhuizen, and U. Blieske, **"Experimental assessment of nanoimprinted textured frontsheets for PV modules,"** in Proc. 8th World Conference on Photovoltaic Energy Conversion (Poster), Milan, Italy, 2022.

- L. Clasing, S. Schaaf, U. Blieske, N. Riedel-Lyngskær, A. A. Santamaria Lancia, and N. Reiners, **"Calculation of the Short-Circuit Current of Colored BIPV Modules under Field Conditions by Application of Spectrally and Angle Resolved Measurement Data,"** in Proc. 38th European Photovoltaic Solar Energy Conference and Exhibition, Online, 2021, pp. 803–807, doi: 10.4229/EUPVSEC20212021-4AV.2.7.

- L. Clasing, J. Münzberg, P. Hakenberg, and U. Blieske, **"Neuartiger Entwurf einer Solardachpfanne zur Lösung anwendungsspezifischer-Probleme,"** in Proc. 37. PV-Symposium, Freiburg, Germany, 2022.

- L. Clasing, C. P. Dick, U. Blieske, J. Münzberg, M. Nennewitz, K. Birkholz, P. Hakenberg, S. Leyer, and J.-R. Hadji-Minaglou **"Analysis of a Novel Improved BIPV/T Roof Tile Design,"** in Proc. 15th Conference on sustainable development of energy, water and environment systems, Online, 2020.

Co-author:

- M. Bartkowski, H. R. Saleemi, L. Clasing, C. Brosig, E. Waffenschmidt, and U. Blieske, **"Development and Validation of a Model for Performance Simulation of an Air-Based BIPVT Roof Tile System Using Open-Source Libraries,"** in Proc. 8th World Conference on Photovoltaic Energy Conversion, Milan, Italy, 2022, pp. 716–723. doi: 10.4229/WCPEC-82022-3BV.3.38.

- C. Brosig, L. Clasing, U. Blieske, and E. Waffenschmidt, **"Modeling a Novel Building-integrated PVT-air-collector System Coupled to a Heat Pump Using Open Source Libraries,"** in Proc. 16th Conference on Sustainable Development of Energy, Water and Environment Systems (SDEWES), Dubrovnik, Croatia, 2021.

- M. Nießen, P. Deck, G. Jöntgen, L. Clasing, U. Blieske, and C. P. Dick, **"Electrical Interconnection of a Solar Roof-Tile System: System Topology and Microconverter,"** in Proc. 16th Conference on sustainable development of energy, water and environment systems (SDEWES), 2021.

- K. Meisenzahl, N. Schneble, M. Volk, U. Blieske, L. Clasing, J. Müller-Ost, J. Münzberg and P. Hakenberg, **"Measuring the Incidence Angle Modifier of Optically Uncoupled Glass for PV Application,"** in Proc. 36th European Photovoltaic Solar Energy Conference and Exhibition, Marseille, France, 2019. doi: 10.4229/EUPVSEC20192019-4AV.2.57.

Danksagung

Hiermit möchte ich mich bei allen Menschen bedanken, die mich während der Anfertigung dieser Arbeit unterstützt und motiviert haben.

Als Erstes möchte ich mich für das entgegengebrachte Vertrauen und die Ermöglichung dieser Arbeit bei Prof. Dr. rer. nat. Ulf Blieske bedanken. Er hat mich an das Thema Solarforschung herangeführt und mir dadurch viele Möglichkeiten eröffnet. Insbesondere konnte er mich mit seiner Expertise und seinem großen Netzwerk bei allen Problemen optimal unterstützen. Ebenfalls möchte ich mich für die optimale Betreuung des interessanten Themas bei Prof. Dr.-Ing. Jean-Régis Hadji-Minaglou bedanken. Außerdem bedanke ich mich bei Prof. Dr. rer. nat. Stephan Leyer und Prof. Dr.-Ing. Inès Chihi für die freundliche Unterstützung und Übernahme des Vorsitzes im Prüfungskomitee.

Ein großes Dankeschön geht an die, zum Teil ehemaligen, wissenschaftlichen Mitarbeiter*innen und Bürokolleg*innen Tobi, Steffi, Rudi, Christian W., Nils, Sascha, Tobias R., Lukas H., Eva und Julia für die gute Arbeitsatmosphäre an der TH Köln. Ich möchte mich auch für die vielen gemeinsamen Stunden in der Kletterhalle und am Fels bedanken, die einen perfekten Ausgleich zur Arbeit im Labor und am Schreibtisch darstellten.

Ich möchte mich auch bei den Kolleg*innen vom CIRE, IBL und der Landmaschinentechnik, insbesondere Christian L., Matthias, Ferdi, Friedrich und Jörg für die große Unterstützung bei der Lösung von mechanischen und konstruktiven Probleme bedanken.

Ich bedanke mich auch für die gute Zusammenarbeit im Forschungsprojekt bei Julian, Christian B., Christian D., Ruth, Eberhardt, Alexej, Martin, Georg, Marius und Peter. In diesem Zusammenhang danke ich auch der Europäischen Kommission und dem Ministerium für Wirtschaft, Industrie, Klimaschutz und Energie des Landes Nordrhein-Westfalen für die finanzielle Unterstützung bei der Realisierung des Forschungsprojekts "Solardachpfanne.NRW" (Fkz.: EFRE-0801561) und dieser Thesis.

Weiterhin möchte ich mich bei meinen Student*innen und HiWis André, Yannik, Esteban, Simon A., Marvin, Kira, Niklas, Christian K., Jakob, Simon S., Felix M.-F., Daniel, Felix G., Pak, Robert, Vaishnavi, Bikram, Marius, Hamza, Shirin, Charlotte und Lukas M. für die anregenden Gespräche und die gute Zusammenarbeit im Labor sowie bei der Anfertigung ihrer Abschluss- und Projektarbeiten bedanken. Es war nicht immer leicht, aber vermutlich habe ich genau so viel dazu gelernt wie die Student*innen selbst.

Ich bedanke mich bei Nicholas für die spannenden und anregenden Diskussionen zum Thema Solarstrahlungsmodellierung und -messung.

Ich bedanke mich bei meinen Freunden die während der Anfertigung eine gute Unterstützung in allen Lebenslagen waren. Ganz besonders danke ich aber meiner Familie, vor allem meinen Eltern Thomas und Christina, die mir das Studium ermöglicht haben. Ich möchte mich auch bei meiner Freundin Sophie bedanken, die mir in der teils entbehrungsreichen Zeit während der Anfertigung dieser Arbeit immer zur Seite gestanden hat. Außerdem bedanke ich mich bei Rita und Heinz für den leckeren Kuchen und viele interessante und aufschlussreiche Gespräche.